Phase separation in thermally-drawn fibers: From porous domains to structured Si-Ge spheres

by

Benjamin Grena

B.S., Physics, Ecole Polytechnique (2011)
S.M., Materials Science, Massachusetts Institute of Technology (2013)

Submitted to the Department of Materials Science and Engineering
in partial fulfillment of the requirements for the degree of

Doctor of Philosophy in Materials Science and Engineering

at the

MASSACHUSETTS INSTITUTE OF TECHNOLOGY

June 2017

Signature redacted

Author .....
Department of Materials Science and Engineering
December 6, 2016

Signature redacted

Certified by... .....
Yoel Fink
Professor of Materials Science and Engineering
Professor of Electrical Engineering and Computer Science
Thesis Supervisor

Signature redacted

Accepted by ....
Donald R. Sadoway
Chairman, Departmental Committee on Graduate Students

Phase separation in thermally-drawn fibers: From porous domains to structured Si-Ge spheres

by

Benjamin Grena

Submitted to the Department of Materials Science and Engineering
on December 6, 2016, in partial fulfillment of the
requirements for the degree of
Doctor of Philosophy in Materials Science and Engineering

Abstract

The preform-to-fiber thermal drawing method is a versatile process that allows the fabrication of polymer or glass-based fibers with complex multimaterial internal structures, which grant them functions ranging from optical transmission to chemical detection. However, while a wide range of materials have been successfully drawn in various phases - such as metals, semiconductors, and ferroelectric polymers - the overall structure of the fiber is typically axially-invariant and the incorporation of heterogeneous materials with isotropic microstructures such as porous domains has remained elusive thus far.

In this thesis we investigate the use of in-fiber phase separation as a means to control the microstructure of different components within thermally-drawn fibers. In particular we propose a novel method based on controlled phase separation of a polymer solution that we use to embed isotropically porous polymeric domains inside multimaterial fibers. We achieve this by thermal-drawing a hollow polymer preform filled with a liquid polymer solution in its core. We later apply this method to the fabrication and characterization of scaffolds for neural regeneration. In addition, we show that the same principle can also be used to draw a functional lithium-ion fiber battery; a fiber device capable of electrochemical energy storage. Finally, we demonstrate how to produce structured Si-Ge spheres encapsulated within a silica cladding by inducing capillary breakup of a continuous Si-Ge core fiber in a strong axial thermal gradient. The thermal gradient causes a "kinetic phase separation" of the alloy, leading to structured Janus particles.

Thesis Supervisor: Yoel Fink
Title: Professor of Materials Science and Engineering
Professor of Electrical Engineering and Computer Science

Acknowledgments

When I was in 11th grade I was denied access to lab classes in physics and chemistry for a semester. I was considered to have no intention whatsoever to learn and every intentions to prevent others from doing so. These accustations were, for the most part, true. Still around that time I found myself in numerous one-on-one conversations with teachers and school officials such as Blandine Kolago, and Mrs. Daillie, who found the patience to repeatedly say they saw a bright future for me, if I could only calm down and focus. I wish to thank them for their perseverance at a time when I deserved it least, and for helping me see further than the tip of my nose.

My scientific training truly began in classes préparatoires at Lycée Saint Louis, and I owe an enormous amount to my physics professors Emmanuelle Archambault and Olivier Joachim. Their lectures and advice still accompany me today, and I would not have made it this far without them.

When I arrived at MIT in 2011 I was a well-rounded student, but had virtually no research experience. I am profoundly indebted to Professor Yoel Fink for opening the doors of his lab to me, and becoming a true mentor. The quality of his scientific insights has never ceased to amaze me, nor has his deep sense of care for others and commitment to helping students grow scientifically and personally. He has been and will remain a great source of inspiration.

I would also like to thank my commitee members. Professor Polina Anikeeva, who reached out to me with exciting new projects and ideas at a time where I was losing momentum. Professor John Joannopoulos for always finding time for me whether it was to discuss project advancements or career paths. Professor Alfredo Alexander-Katz for his enthusiasm and many fun and exciting conversations.

My time at MIT would not have been the same without the amazing team members of the fibers@mit group. I want to thank Dr. Guillaume Lestoquoy who introduced me to the group in the first place, and has continued to be a great friend even after his path led him away from MIT. I thank Dr. Sasha Stolyarov as well, for hours of brainstorming when I began my work in the group, and for being such an example to follow as a scientist. I am also grateful to Dr. Jung Tae Lee who has been my partner on the lithium-ion battery enterprise and whose hard work and ideas have contributed to drive the project out of the doldrums. I am infinitely thankful to Dr. Noémie Chocat, Dr. Chong Hou, Prof. Xiaoting Jia, Prof. Alexander Gumennik, Prof. Lei Wei, Jeff Clayton, Tara Sarathi, Michael Rein, Rodger Yuan, Dr. Etgar Levy, Dr. Tural Khudiyev, and Gabriel Loke. Interacting with them on a daily basis

has been unique chance, and their creativity, enthusiasm and scientific rigour have helped me become a better scientist. Lastly I extend my gratitude to Tina Gilman, for her unmatched kindness, her time, and her help in all matters!

Outside of the group I was extremely fortunate to collaborate with many highly-talented people on various projects. Dr. Ian Matts and Dr. Kang Xu were my anchor-points on experimental and theoretical aspects of the battery project for a long time; I have a learned so much from them. In addition I consider myself extremely lucky to have collaborated with Prof. Ryan Koppes and Seongjun Park on the porous scaffold project; discussing scaffold designs from a biological standpoint and receiving training on neuron culture and immunocytochemistry was among my most exciting learning experiences at MIT. I also thank Andres Canales for fruitful conversations on many technical aspects of fiber drawing.

A lot of my work has led me to use machines and instruments I did not even know existed 5 years ago, and I wish to extend my thanks to all the specialists who trained me. In particular Michael Tarkanian from the DMSE machine shop and Mark Bellanger from the Edgerton machine shop for teaching me the arts and science of plastics and metals machining and prototyping; I have spent countless hours in their premises. Likewise I thank Steven Kooi and William DiNatale of the Institute of Solidiers Nanotechnology for helping me design experimental setups and reinstate abandoned equipments.

I thank as one all my teammates throughout the years of the DMSE soccer team, the SBC team, and more recently the French@MIT team. Despite bruises and probable long-term trauma, I have cherished these moments on the field with the candor of a 7-year-old.

When I left for MIT I was miles away from imagining how crazy and thrilling the next five years would be. I owe that entirely to a handful of people. Hadrien Laubie, MIT companion in labor and trusted "*partenaire de bagarre*"; Pierre Baduel, resourceful inventor of facts and creator of debates; Matthieu Landon and Alice Pabst, living proofs that perpetual fun is not prohibited by the laws of physics. I am so lucky to have lived this adventure with them. A big thank you as well to Julien "*Full Control*" Amouyal - the Brahmin was never the same without him. Thoughts and gratitude to the French gang at large, Loulett and Sarah Reneaume for their genuine coolness, Claire Nicolas for sharings tips and distress over the job market, and all the VIEs who came and went! Thank you also to Alex Toumar, your untimely intrusions in my office were always so refreshing.

I left many pieces of me in France and abroad when I moved here. My buddy Charles Bernard (1P2C 4lyf), The Crew La Tour: Alison, Vince, Marie, Jen, Rémi (PSI STAR!), Joulane, Polo, Christophe, and of course Bobo MdC whom I missed so much he had to come and visit for a year and a half! You are all my beacons of *kiff*.

My family in France has been a boundless source of love and support throughout these 5 years and throughout my life. In particular I thank my parents for always being there for me and never pushing me into a predefined direction. My sister Juliette and my brothers David and Vincent, for being my friends and models. Being away from them (and my growing nieces!) was by far the hardest part of my journey.

Finally to Éléonore: *merci !* Five years ago you came to visit for Thanksgiving. We ate guacamole and fell asleep early. We were children, and we had no idea what tomorrow would be like. Today we still have no clue what lies ahead, but our love gives me strength, and joy, and hope. Let's keep being children together!

List of abbreviations

CB: Carbon black

CNS: Central nervous system

COC: Cyclic olefin copolymer

CPA: Constant phase angle

CPE: Carbon-loaded polyethylene

CV: Cyclic voltammetry

DAPI: 4',6-diamidino-2-phenylindole

DRG: Dorsal root ganglion

EC: Ethylene carbonate

EDS: Energy dispersive spectroscopy

EtOH: Ethanol

FDA: Food and Drug Admininstration

LCO: Lithium cobalt oxide, $LiCoO_2$

LDPE: Low-density polyethylene

LFP: Lithium iron phosphate, $LiFePO_4$

LiTFSI: Bis(trifluoromethane)sulfonimide lithium salt

LTO: Lithium titanate, $Li_4Ti_5O_{12}$

PBS: Phosphate buffer solution

PC: Proylene carbonate

PCL: Poly-ϵ-caprolactone

PEI: Polyetherimide

PNS: Peripheral nervous system

PVdF: Poly(vinylidene fluoride)

PYR13TFSI: N-propyl-N-methylpyrrolidinium bis(trifluoromethanesulfonyl)imide

SEM: Scanning electron microscope

TIPS: Thermally-induced phase separation

Triglycol: Triethylene glycol

Contents

Chapter 1

Introduction

1.1 Multimaterial fibers

1.1.1 Historical perspectives

Recent archeological findings in the north coast of Peru have identified man-made indigo-dyed cotton fabrics on the Preceramic site of Huaca Prieta, dating back to 4,000 BC [Splitstoser et al., 2016]. In 1871, close to 6,000 years later, Jacob W. Davis and Levi Strauss filed a patent for the invention of the blue jeans - a pair of sturdy rivetted pants made from an indigo-dyed cotton fabric with a structure remarkably close to its Huaca Prieta counterpart. The anecdote is symbolic of a more general trend: fibers and fabrics virtually did not evolve on a technological standpoint from their earliest forms of human useage around 30,000 BC [Kvavadze et al., 2009] up to the beginning of the 20th century. The advent of synthetic polymers in the 20th century was the first evolution in the field for millenia. With manufactured fibers such as Nylon, polyester or Spandex, companies like DuPont introduced fabrics with enhanced properties - displaying improved mechanical robustness, elasticity, or higher thermal insulation. Still, these fibers were - and still are today - intrinsically passive and made of single materials, their benefits relying only on the intrinsic properties of the synthetic materials they are made of.

In parallel, the late 20th century saw the emergence and rapid development of an another type of fiber for a completely different set of applications: fiber optics for telecommunications. In 1956, Lawrence Curtiss - then an undergraduate in the University of Michigan - produced the fist core-cladding glass fiber by inserting a high refractive index glass rod in a low-refractive index glass tube, and subsequently heating and pulling on the structure to draw it down into a fiber [Hecht, 2004]. For the first time a structured fiber made of two different materials saw the light of day; and with structure came functionality, as the fiber enabled to guide optical signals with much lower loss than single-material glass fibers. The method he and others around the same time invented [Hecht, 2004], known as the thermal-drawing process, led to the extremely rapid growth of the field of fiber optics. Today, it is estimated that around 180 million kilometers of optical fibers are produced every year to sustain worldwide communications [Ballato and Dragic, 2016].

Over the past 15 years, our group has focused on exploiting the thermal-drawing process to depart from optical transmission capabilities and introduce a new concept: multimaterial fiber devices. By combining a multiplicity of materials in a prescribed architecture into a fiber, we can build fibers that are no longer passive but are able to sense, hear, and communicate [Abouraddy et al., 2007]. The integration of functional fibers into fabrics is a paradigm shift - from the millenial notion of passive fabrics and textiles, to the new conception of complex and highly functional fabric systems.

1.1.2 Thermal-drawing process

The thermal drawing process starts by the fabrication of a multimaterial macroscopic object called a preform, identical in its geometry and composition to the final fiber however much larger in its cross sectional dimensions and shorter in length. A preform is usually comprised of a cladding material and functional materials, in a well-chosen architecture. The cladding material can either be an amorphous thermoplastic or silica glass, depending on the temperature regime sought. Its function is mostly to support the stresses arising in the fiber during the draw process. Examples of thermoplastic materials used as cladding include polycarbonate, polysulfone, polyetherimide,

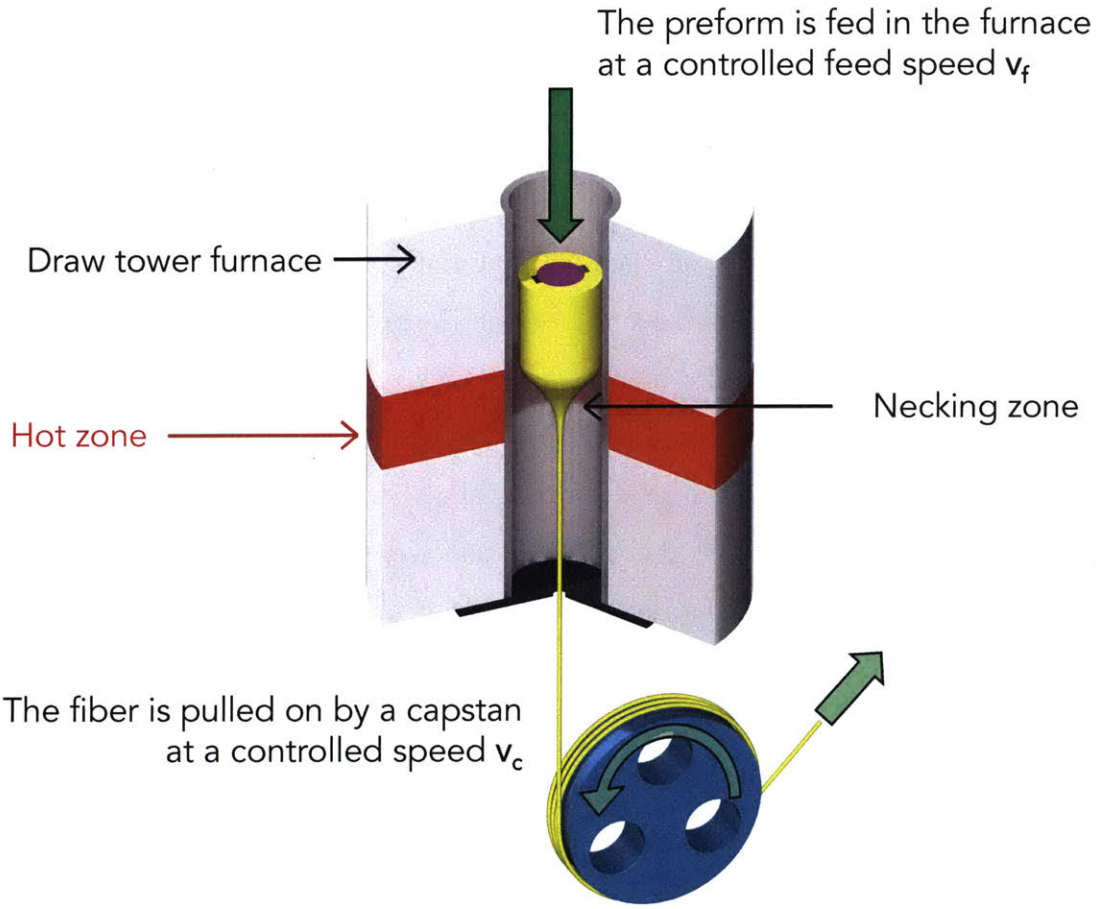

Figure 1-1: Schematic representation of the thermal drawing process. The preform is loaded into the furnace and fed downwards at a controlled feed speed. The cladding is represented in yellow and the "active material" in purple. The preform necks down in the hot zone and extends into a fiber, which is pulled on at a controlled speed. Figure courtesy of G. Lestoquoy.

or poly(methy methacrylate). In polymer preforms, cladding and active materials are assembled by either film-rolling or stacking, followed by a consolidation step to fuse the different materials into one solid part. Because the cladding material constitutes the majority of the preform in weight, it dictates the regime of draw temperatures.

Once assembled and consolidated the preform is taken to a draw tower and preheated in a vertical furnace to an elevated temperature. The furnace temperature is controllable in three points corresponding to the top, bottom and middle zone. The middle zone temperature is usually set to be the hottest, and thus we often refer to the middle zone as the hot zone. During preheating the hot zone temperature is set to around 100 to 120°C above the cladding material's glass transition temperature. The aim of this preheating step is to locally soften the preform in the region of the hot zone to a point where it necks down and starts falling under the effect of gravity. We call this event the "bait-off". Following the bait-off, the bottom part of the preform is cut and thrown away, and the proper drawing of the fiber then starts. The fiber is fed into a capstan which pulls on the fiber at a constant controllable speed v_{capstan}, meanwhile the preform is fed into the furnace at another prescribed feed speed v_{downfeed} (cf. Fig. 1-1). Conservation of volume dictates that the draw-down ratio ν, relating the cross-sectional features dimensions in the preform to dimensions in the fiber, is set by the processing speeds as:

$$\nu = \frac{L_{\text{preform}}}{L_{\text{fiber}}} = \sqrt{\frac{v_{\text{capstan}}}{v_{\text{downfeed}}}}$$

A set of lasers measures the cross-sectional dimensions of the fiber, and a tensiometer measures the tension in the fiber, which is then used to compute the stress in real time. By monitoring the process with a LabView program and properly controlling the different control knobs (mostly capstan speed and furnace temperatures), one can draw a fiber extending hundreds of meters in length. Provided the different materials in the preform are able to codraw at the draw temperature, the fiber conserves the geometry and composition of the preform, but its cross-sectional dimensions are reduced by a factor ν of 10 to as large as 500.

1.1.3 Advantages and constraints

Key advantages

The advantages of the thermal drawing process are numerous: the method enables the incorporation of multiple materials into fibers, and the scalable production of fiber devices with submicron features extending kilometers in length. For example, materials such as chalcogenide glasses [Hart et al., 2002; Sorin et al., 2007], metals [Bayindir et al., 2004], composite polymers [Egusa et al., 2010], piezoelectric polymers [Egusa et al., 2010; Chocat et al., 2012], traditional semiconductors [Ballato et al., 2008; Gumennik et al., 2013], have been successfully drawn in fiber structures. Functional fiber devices made with this diverse set of materials include photonic bandgap transmission fibers [Hart et al., 2002], photodetecting fibers [Sorin et al., 2007], fiber capacitors [Lestoquoy et al., 2013], or even acoustic fiber transducers [Egusa et al., 2010]. Furthermore, once a fiber is drawn, it can be weaved and integrated into large-area multicomponent architectures of various shapes [Abouraddy et al., 2006; Sorin et al., 2009; Chocat et al., 2012]. Thus, the fiber is an elementary building block to large-area conformal and flexible electronic systems.

Main constraints

This method however imposes constraints on the materials that can be used. First of all, it relies on the application of heat at relatively high temperatures - commonly in the 150-300°C temperature range for polymer fibers. This can cause some materials to decompose or degrade, preventing their use. Second, the materials composing a preform should be able to co-flow, in other words they should have similar rheological properties in the regime of draw temperatures (cf. Fig. 1-2 as an illustration). For a controlled draw, the viscosity of the cladding material should be between 10^3 and 10^6 Pa.s - with lower and upper bound corresponding to low and high tension drawing regimes. If a crystalline material is to be introduced in a fiber, it needs to have a melting point below the draw temperature defined by the cladding. This sets constraints on the possible combination of materials.

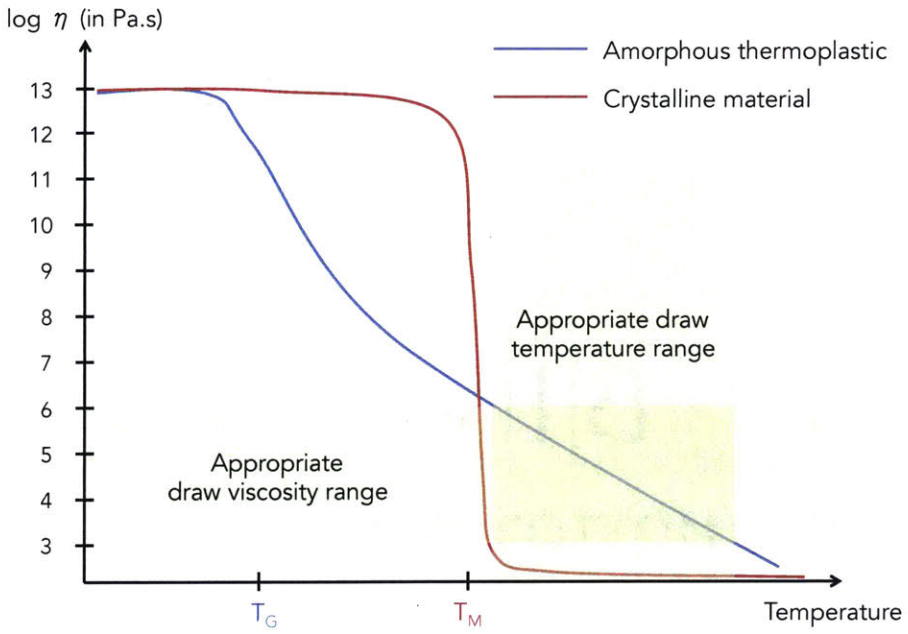

Figure 1-2: Illustration of rheological constraints on materials codrawability.

On top of constraints on materials selection, fiber thermal drawing also suffers from a structural constraint: the method generally only produces axially invariant fibers, with the same structure as the preform. This limit is obviously a direct consequence of the fabrication method itself, relying on extensional flow of all the fiber's components. This flow-induced anisotropy is true for the fiber structure as a whole as well as the microstructure of individual materials. Introducing heterogeneous materials with isotropic microstructures in a preform typically leads to axially-elongated anisotropic microstructures of the materials in the fiber. This in turns may limit the functionality of the fiber devices - precluding for example the incorporation of porous materials with transverse porosity, or structure-wise prohibiting in principle axially-resolved fiber sensors or punctual light emission.

A path beyond constraints

Recent studies stemming from our group and others have shown some paths to go beyond materials selection as well as structural constraints.

On the materials aspect, Orf et al. and Hou et al. have shown that the composition of the final fiber may be different from the initial preform composition. Both authors have shown, in two different materials systems, that the preform drawing process itself can be used to trigger chemical reactions between preform components leading to the synthesis of new compounds during the fabrication process. Orf et al. demonstrated the synthesis of crystalline zinc selenide during the drawing of a polymer fiber around 200°C, occuring from a reaction between selenium-rich glass and zinc-tin metal wires. Zinc selenide having a melting point of 1,525°C, direct incorporation of the material in the preform would not have been possible. Hou et al., on the other hand, observed aluminum-in-silica preforms becoming silicon-in-silica fibers in the drawing process. They attributed the result to the reduction of silica by the aluminum at high temperature, producing pure silicon and aluminum oxide.

Structurally, Kaufman et al. established a method to break the axial invariance of drawn fibers by breaking up axially-continuous components into a series of discrete spherical particles encapsulated within the cladding material. The method revolves around the phenomenon of capillary breakup - the surface tension-driven spontaneous evolution of fluid cylinders into droplets. The actual observation of the phenomenon in fibers was first reported by Shandon D. Hart in his Ph.D. thesis, and was perceived as an issue preventing the production of continuous domains of nanometer-size. Kaufman et al. harnessed the instability to produce spheres of chalcogenide glass embedded within a polymeric cladding.

1.2 Thesis outline

In this thesis, we wish to expand upon the materials and structures that can be incorporated in a drawn fiber by harnessing in-fiber phase separation phenomena. Phase separation is a type of phase transition occurring in systems comprised of multiple substances. Upon the change of some intensive parameter such as temperature or concentration, a multi-component system can undergo a transition from a single-phase homogeneous solution, to a heterogeneous system with multiple coexisting phases.

The same way Orf et al. and Hou et al. use chemical reaction to change the composition of the materials in their fibers, we here aim to use phase separation to produce domains within fibers made of heterogeneous materials with controlled and isotropic microstructures.

In Chapter 2, we present an approach combining the thermal drawing process with the low-temperature phase separation of a polymer solution encapsulated within the preform, generating porous domains in the final fiber. We show that we can use this method to produce multimaterial porous fibers with engineered architectures embedding internal porous domains along with other homogeneous materials, with highly controlled cross-sectional features.

In Chapter 3, we establish the general method presented in the previous chapter as a platform for the production of porous fiber scaffolds for neural regeneration. Nerve guidance scaffolds are synthetic devices used to bridge gaps in peripheral nerves following an injury. Here we design and fabricate a multimaterial porous neural scaffold using in-fiber phase separation, and demonstrate its viability in vitro.

In Chapter 4, we apply the principles of Chapter 2 to the fabrication of a lithium-ion fiber battery. We develop battery components which behave as viscous liquids at high temperature during our drawing process, but phase separate to form solid-like gels in the final fiber. We analyze the electrochemical performance of these components at the preform level and demonstrate cycling behavior in the first Li-ion fiber battery.

In Chapter 5, we study another example of a phase separation phenomenon occuring in microspheres of Si-Ge alloys produced by capillary breakup of a core-cladding fiber. Control of the crystallization kinetics enables to access two different microstructures: the first being an oriented Si-Ge Janus particle and the second a sphere made of dendrites of germanium in silicon.

Chapter 2

Porosity in thermally-drawn fibers

2.1 Motivations and background

Porous polymeric fibers are high aspect ratio filaments displaying a substantial level of internal porosity. Such fibers find applications in gas separation [Kapantaidakis and Koops, 2002; Li et al., 2004; Hosseini et al., 2010], water filtration [Tan et al., 2006; Wang et al., 2008, 2010], hemodialysis [Cross et al., 1971; Yang et al., 2007; Zhang et al., 2014], or tissue engineering [Unger et al., 2005; Mercado-Pagán et al., 2015; Wen and Tresco, 2006]. The fabrication of these fibers generally relies on the extrusion - or spinning - of a polymer solution followed by its phase separation [Strathmann, 2011]. In particular, in the case of thermally-induced phase separation (TIPS), a solution is homogenized at high temperature and cooled or quenched so as to trigger its phase separation into a solvent-rich and polymer-rich phase with subsequent solidification of the polymer-rich phase [Lloyd et al., 1990, 1991]. The solvent can later be removed by rinsing or evaporation to yield the final porous structure. With this process, porous fibers from a variety of polymers have been produced [Kim et al., 1995; Cha and Yang, 2007; Matsuyama et al., 2003; Karkhanechi et al., 2016; Qiu et al., 2009]; however they are generally made from a single material in a cylindrical geometry, and are intrinsically passive. A typical hollow fiber membrane microstructure is presented in Fig. 2-1. The ability to fabricate complex fiber architectures with multiple materials organized around a porous domain would pave the way towards

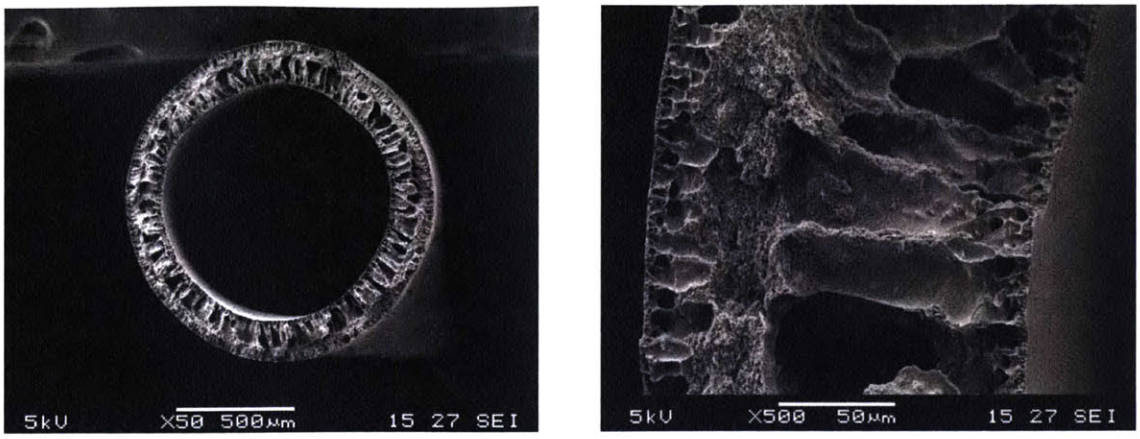

Figure 2-1: From Wang et al. [2009]. Typical cross-sectional microstructure of a PVdF porous fiber membrane.

new types of multifunctional and active porous fiber devices, such as flow-sensing filtration fibers, sweat sensing textiles, or electrically active cell-scaffolds.

On the other hand, the preform-to-fiber thermal drawing method has proven to be a versatile process allowing the fabrication of polymer-based fibers with complex multimaterial internal structures [Hart et al., 2002; Bayindir et al., 2004; Abouraddy et al., 2006; Sorin et al., 2007; Egusa et al., 2010; Chocat et al., 2012; Stolyarov et al., 2012; Gumennik et al., 2012]. As we have seen in Chapter 1, thermally drawn fibers can include a wide range of materials including metals, semiconductors, composites or ferroelectric polymers, granting them capabilities such as light sensing [Bayindir et al., 2004; Sorin et al., 2007], piezoelectric actuation [Egusa et al., 2010; Chocat et al., 2012], chemical detection [Gumennik et al., 2012], or even neural activity stimulation and recording [Lu et al., 2014; Canales et al., 2015]. However, the fabrication of fibers with internal porous domains through this method had remained elusive thus far. The challenge arises from the fabrication method itself, which relies on the flow and elongation of the fiber materials in a low-viscosity state. Direct incorporation of porous materials in the preform is therefore inadequate, as pores tend to elongate and collapse during the drawing process.

In this chapter we present a novel method combining the advantages of thermal drawing with the principle of polymer solution thermally-induced phase separation

to generate porous fibers with complex architectures that could not be achieved otherwise. For this we take advantage of the fact that the thermal drawing method intrinsically takes the preform materials from a high temperature state in the furnace, to a fiber-form low-temperature state upon exiting the furnace. Therefore by filling the preform with a well-chosen polymer solution, we can trigger the latter's phase separation during the draw and produce complex multimaterial fibers with porous domains, out-of-reach to any other porous fiber production techniques.

2.2 In-fiber thermally-induced phase separation of polymer solutions

2.2.1 Methodology

Our general method starts with the fabrication of a macroscopic object called a preform [Tao et al., 2012], which serves as a template for the porous fiber we wish to produce. The preform acts here as a reservoir with a well-defined architecture that we fill with a polymer solution prior to the draw. During the drawing process, we heat the preform in a furnace above the glass transition of the preform material and above the phase separation temperature of the polymer solution, such that the solution remains homogeneous in the furnace. The preform is drawn into a fiber by constant pulling at a controlled speed, and the fiber cools down to room temperature (Fig. 2-2.a). Provided the polymer solution demixes between the drawing temperature and ambient temperature, the solution phase separates in the fiber leading to a porous polymeric core whose pores are filled with a solvent-rich phase (Fig. 2-2.c), much like in a conventional solution extrusion technique. Phase separation in TIPS processing can either occur through liquid-liquid demixing [Lloyd et al., 1991], where the two phases initially formed are liquid and the polymer-rich phase solidifies at a lower temperature, or solid-liquid in which case the polymer crystallizes out of the solvent directly [Lloyd et al., 1990]. In this paper we work with both types of solutions. As an illustration, Fig. 2-2.b shows a typical phase diagram for a liquid-liquid demixing

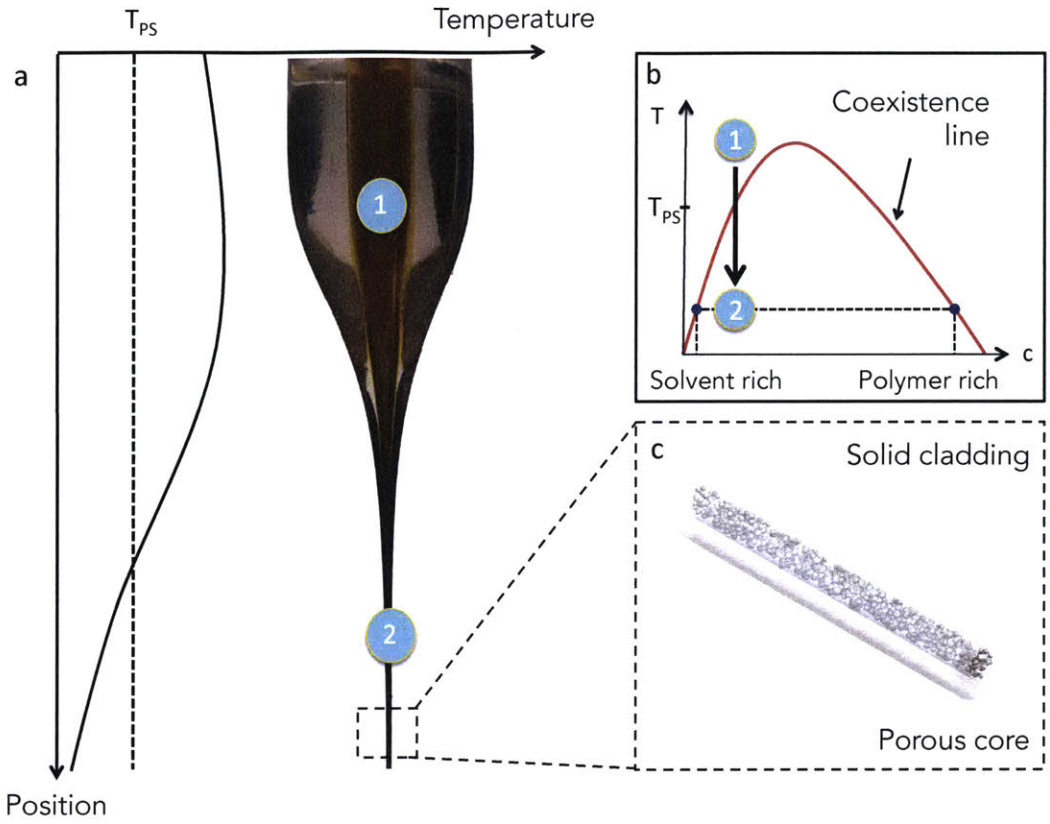

Figure 2-2: Fiber fabrication method and cross-sections. (**a**) General illustration of thermal drawing process, with the associated temperature profile. The dashed line denotes the phase separation temperature for the polymer solution in the core. (**b**) Schematic phase diagram for a generic polymer solution. State 1 is the homogeneous state in the furnace, and state 2 is the phase separated state at room temperature. (**c**) Illustration of a section of drawn fiber with the dense cladding surrounding the porous core

solution [Lloyd et al., 1991; Van de Witte et al., 1996]. After the draw, the dense cladding illustrated in Fig. 2-2.c may be dissolved with an appropriate solvent, and the liquid phase subsequently evaporated resulting in porous fibers.

2.2.2 Materials selection

We demonstrate the process using a cyclic olefin copolymer (COC, TOPAS 8007 from TOPAS Advanced Polymers) preform as a cylindrical reservoir. COC is an amorphous thermoplastic displaying excellent chemical resistance to many polar organic solvents,

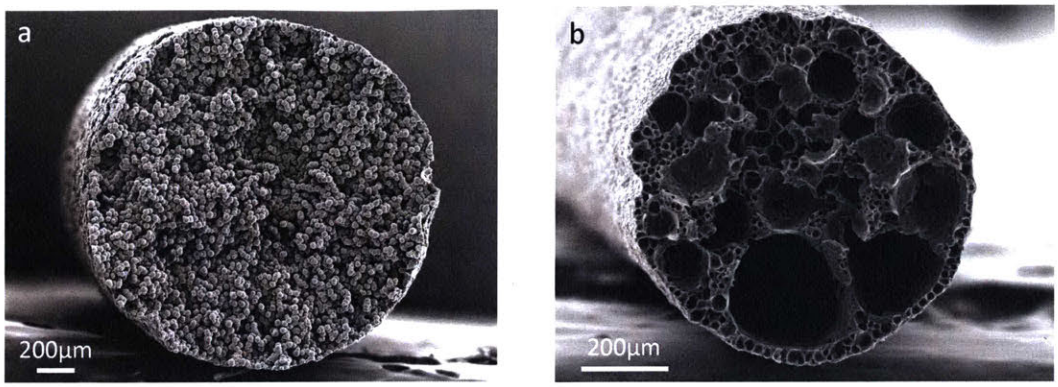

Figure 2-3: Cross-sectional SEM images of porous fibers made of (**a**) PVdF and (**b**) PCL obtained after cladding dissolution.

and can be thermally drawn between 150°C to 300°C. Prior to the draw, we fill the cylindrical hollow reservoir with a 1:4 wt. solution of polyvinylidene fluoride (Kynar 761, Arkema) in propylene carbonate (PC). This solution has a S-L demixing temperature around 35°C [Su et al., 2007], so that it is homogeneous during the draw process but phase separates in the fiber core as it cools down to ambient temperature. By selectively dissolving the COC cladding in toluene, one obtains porous PVdF fibers. The SEM micrograph of the fiber cross-section (Fig. 2-3.a) shows a morphology consisting of interconnected PVdF spherulites separated by voids. Such morphology is common for solid-liquid phase separated PVdF membranes [Lloyd et al., 1990; Van de Witte et al., 1996], and arises from nucleation and growth of highly semicrystalline PVdF spherulites [Su et al., 2007].

We are not limited to PVdF as a porous matrix material. Without changing the cladding material, we can replace the PVdF solution with a solution of poly-ϵ-caprolactone (PCL) in a 1:1 wt. mixture of propylene carbonate and triethylene glycol. The two miscible solvents used act as a latent solvent for the polymer, and a phase separation of the solution also occurs in the fiber as it cools down to room temperature. A SEM micrograph of the porous core is shown in Fig. 2-3.b. It displays a very different morphology than that of the porous PVdF fibers, with a broad distribution of cellular pores separated by polymer walls. This morphology is indicative of a liquid-liquid phase separation occurring through nucleation of a

solvent-rich phase followed by subsequent solidification of the polymer-rich phase [Lloyd et al., 1991; Van de Witte et al., 1996], and has also been reported previously in literature for PCL membranes [Tanaka et al., 2006].

2.3 Advantages of processing method

2.3.1 Geometry and materials architecture

Control over external geometry

The first advantage of this new porous fiber processing method is that we can easily control the fiber cross-sectional geometry, unlike in extrusion-based processes which requires complex spinneret engineering as well as optimized cooling and solidification conditions [Zhou et al., 2010]. The preform acts here as a template for the porous fiber, and by machining the internal geometry of the preform into arbitrary shapes, we could produce porous fibers with complex external geometries such as triangular, or cross-shaped (Fig. 2-4.a-d). The ability to do so is a consequence of the large viscosity contrast between the cladding and the solution during the drawing process. At the high draw temperature, the cladding material exhibits a viscosity close to 10^4 Pa.s, roughly 4-5 orders of magnitude higher than that of the polymer solution (as shown in Figure 2-5). This high viscosity of the cladding kinetically prevents the capillary rounding of sharp features to occur, while the low-viscosity solution fills the whole accessible volume, and phase separates into a porous fiber of the same shape. Therefore the external geometry of the porous fiber is only limited by our ability to machine a preform of the matching shape, and does not require complex spinneret engineering and optimization of spinning conditions. Even with advanced spinneret design and spinning processes, obtaining geometries that significantly deviate from equilibrium presents significant challenges [Zhou et al., 2010].

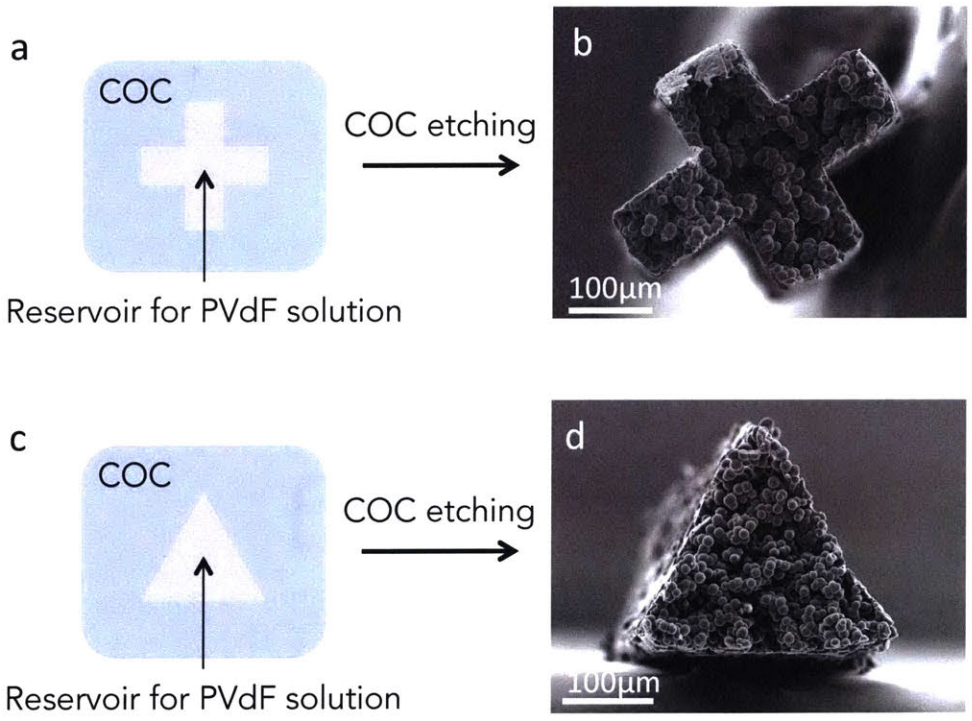

Figure 2-4: Control of external geometry. (**a**) Schematic illustration of a preform with a cross-shaped reservoir for PVdF solution, and (**b**) SEM micrograph of the cross-shaped porous PVdF fiber after drawing and cladding dissolution. (**c**) Schematic illustration of a preform with a triangle-shaped reservoir for PVdF solution, and (**d**) SEM micrograph of the triangle-shaped porous PVdF fiber after drawing and cladding dissolution.

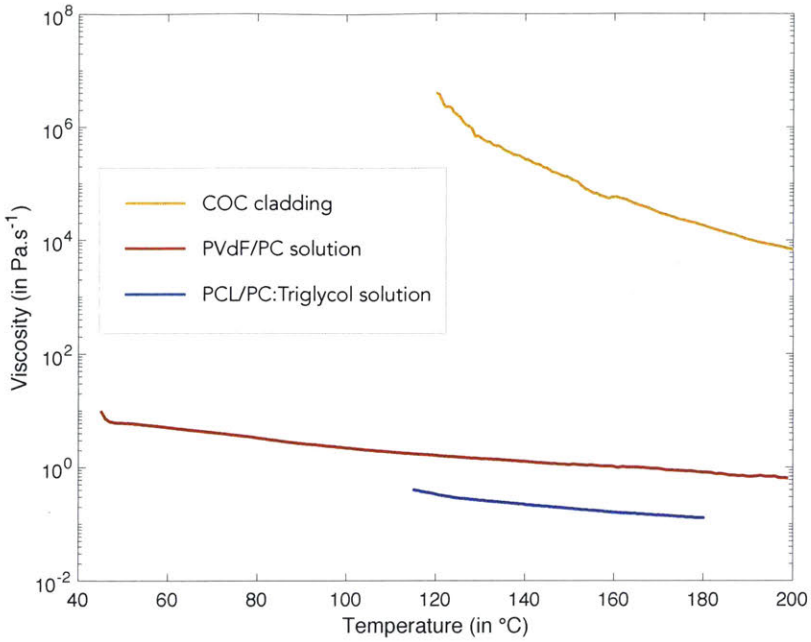

Figure 2-5: Zero-shear viscosity of COC cladding, PVdF/PC solution, and PCL/PC:Triglycol solution.

Control over materials distribution

The second key benefit from this preform-to-fiber TIPS is the ability to combine multiple materials adjacent to a porous domain. In solution extrusion-based methods this requires the design of complex concentric co-extrusion nozzles. Here, we could achieve it by initially designing and assembling the preform template with the desired materials. We demonstrated this by producing a porous PCL core/dense LDPE shell fiber, using our in-fiber TIPS approach. First, we constructed a preform consisting of a hollow core lined by a shell of LDPE of 200μm, embedded in a large centimer-size COC cladding (Fig. 2-4.a). Second, we introduced the PCL solution into the hollow-core and drew the multimaterial preform into a fiber. Finally, we selectively dissolved the COC cladding using cyclohexane and dried the solvent out of the core to leave only a thin shell of LDPE surrounding a porous PCL core (Fig. 2-4.b-c). Here, the in-fiber LDPE shell wall thickness was 10 μm, but in principle it could be made thinner by faster drawing speeds. This type of structure could be useful for gas separation fibers with dense selective barriers [Li et al., 2004; Hosseini et al., 2010].

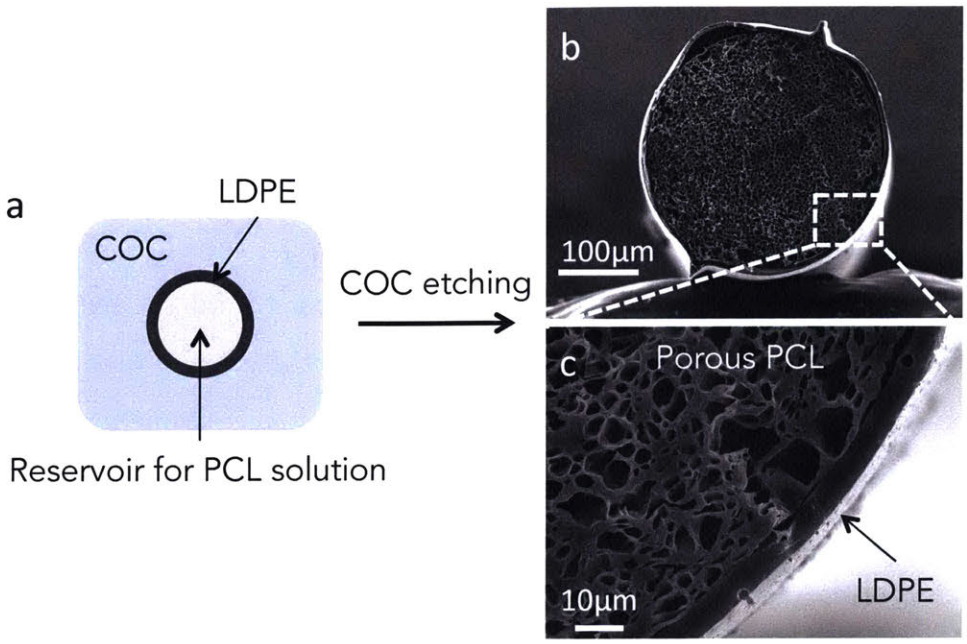

Figure 2-6: Control of architecture. (**a**) Schematic illustration of a COC preform with a cylindrical reservoir for PCL solution lined with a thin LDPE wall, and (**b-c**) SEM micrographs of the final porous PCL core/dense LDPE shell fiber after drawing and cladding removal.

2.3.2 Control over microstructure

In addition to external geometry and materials distribution, the preform-to-fiber TIPS method also allows some degree of control over the microstructure of the porous domain through control of the quenching temperature, specifically for L-L demixing solutions. Figure 2-7 demonstrates the effects of fiber quenching temperature on the average pore size of a PCL porous core fiber, estimated from an image analysis of the cross-sectional micrographs.

For this study, fiber samples were reheated post-draw to T_{reheat} =150°C in order to rehomogenize the solution, and quenched for a fixed time Δt=5min in a water/ethylene glycol bath at set temperatures T_{bath}. Three fiber samples were post-processed per quenching temperature, and a total of 6 SEM micrographs were analyzed per cooling condition. The results indicate that fibers quenched in colder baths exhibit smaller average pore sizes, with an apparent transition in the behaviour of pore size versus quenching temperature around 40°C. These results can be rationalized

considering the specifics of the PCL solution's phase diagram, schematically represented in the inset of Figure 3a. At our working concentration, the solution exhibits a liquid-liquid demixing at a relatively elevated temperature (≈110°C, observed visually by appearance of turbidity in the solution), followed by a PCL solidification at lower temperatures, around 40°C (also observed qualitatively). Therefore when quenched above 40°C, we expect the liquid-liquid phase separated structure to exhibit coarsening. During coarsening, the system seeks to minimize the interfacial energy between the polymer-rich phase and the solvent-rich phase by minimizing the surface area and forming larger voids [Van de Witte et al., 1996; Balluffi et al., 2005]. This can happen either through diffusion of molecules from small to large droplets (Ostwald ripening), coalescence of droplets, or hydrodynamic flow [Aubert, 1990; Song and Torkelson, 1994]. All these processes result in scaling laws of the form:

$$\langle R\rangle^{\alpha} = \langle R_0\rangle^{\alpha} + K_{\alpha}(T)\Delta t \tag{2.1}$$

where α is 3 for Ostwald ripening or coalescence-based coarsening, and 1 for coarsening through hydrodynamic flow, K_{α} is a prefactor depending on temperature and on the exact mechanism involved, and $\langle R_0\rangle$ is the average droplet nucleus size [Aubert, 1990; Song and Torkelson, 1994]. While the exact functional for K_{α} is unknown for our system, all of the associated processes are thermally activated and thus their rates grow with increasing temperature - explaining the increase in pore size with temperature. For samples quenched in a bath below 40°C the PCL will rapidly crystallize, thus setting the structure and preventing further coarsening. The effective time of coarsening Δt_{eff}, or time during which the structure is in a liquid-liquid state, is reduced as the sample is convectively cooled from T_{reheat} to T_{bath} . At deep enough quenching, coarsening is almost completely suppressed and the average pore size approaches the droplet nucleus size, setting a lower limit on pore size for L-L demixing solutions. For this reason, the pore size is nearly temperature independent for deep quenching as seen in Figure 2-7.a. In practice, this cooling step could be added in series with the drawing process itself to permit direct control of the pore size

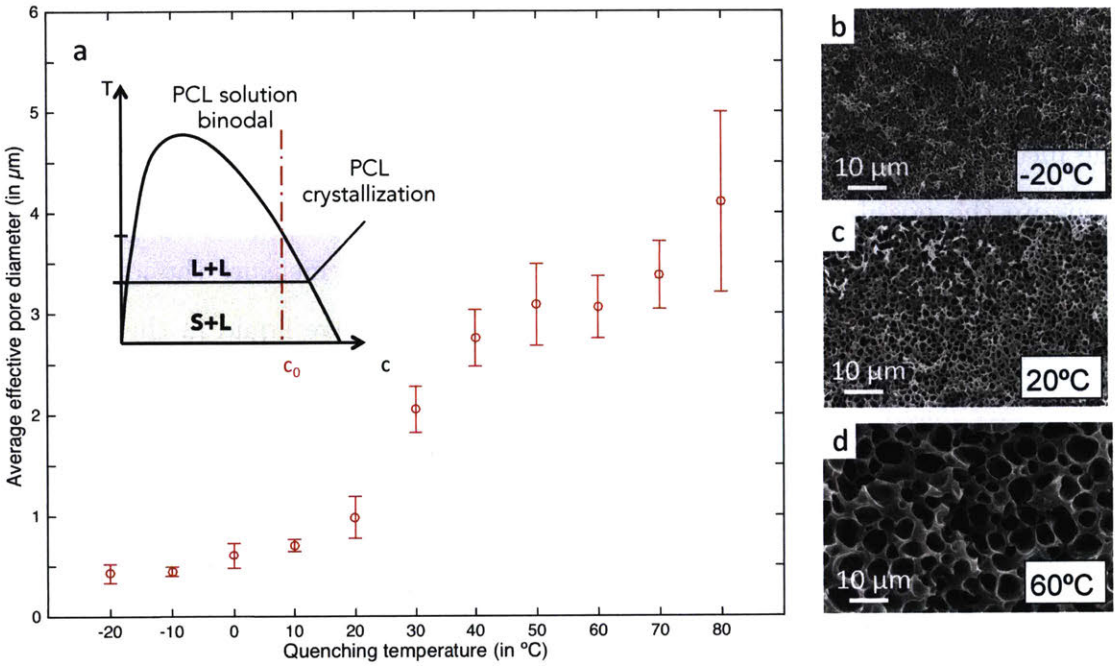

Figure 2-7: Influence of quenching temperature on microstructure. (**a**) Average pore size for different quenching temperatures in ethylene-glycol-water bath. The error bar corresponds to the standard deviation over the mean pore size in the 6 images analyzed per quenching conditions. The inset displays an illustration of the possible phase diagram with a dashed line at the working concentration, highlighting both liquid-liquid and solid-liquid demixing. (**b-d**) Associated cross-sectional SEM images for fibers quenched at -20°C, 20°C and 60°C.

along arbitrary lengths of fiber. The coarsening mechanism varies between solution systems, specific concentrations, temperatures, and time - but α and K_α can be determined experimentally by performing measurements of the average pore size with time at fixed temperatures [Song and Torkelson, 1994; McGuire et al., 1995]. This knowledge could then be used to determine specific cooling conditions required to obtain a desired pore size.

2.4 Demonstration of transport and fiber functionality

The incorporation of multiple materials adjacent to a porous domain within a fiber opens up the possibility of introducing functionalities in porous fibers. To demonstrate this idea, we developed a fiber that can be used to measure the ionic conductivity of a porous domain filled with an ionically conductive liquid in the core of the fiber.

In our process, when the fiber exits the furnace and cools down, the core consists of a porous polymer filled with a solvent-rich liquid phase. By initially introducing a soluble and thermally stable ionic liquid in the core solution, we can therefore fill the pores with an ionically conductive electrolyte in a single step. We can then use ionic conductivity measurements to probe the transport properties of our fibers, in both axial and transverse directions.

2.4.1 Transverse conductivity measurements

Fiber design

We start by employing the in-fiber TIPS method to fabricate a fiber with the cross section shown in Fig. 2-8.a. The initial preform core is filled with a solution of of 1:4 wt. PVdF and propylene carbonate, with the addition of a 10^{-3}m (mol/kg of solvent) PYR13TFSI (Solvionic) ionic liquid in propylene carbonate providing ionic conductivity. When the solution phase separates in the fiber, it generates a porous domain with an ionically conductive solvent-rich phase. We used PYR13TFSI as an ionic liquid owing to its solubility in propylene carbonate and high thermal stability preventing degradation during the draw. We purposefully chose a low ionic liquid concentration to decrease the conductivity of the electrolyte, and later be able to neglect resistive contributions from other elements in the system. Adjacent to the porous core are two carbon-loaded polyethylene electrodes (CPE), contiguous with two low-temperature Bi-In metal buses. The combination of a porous domain, com-

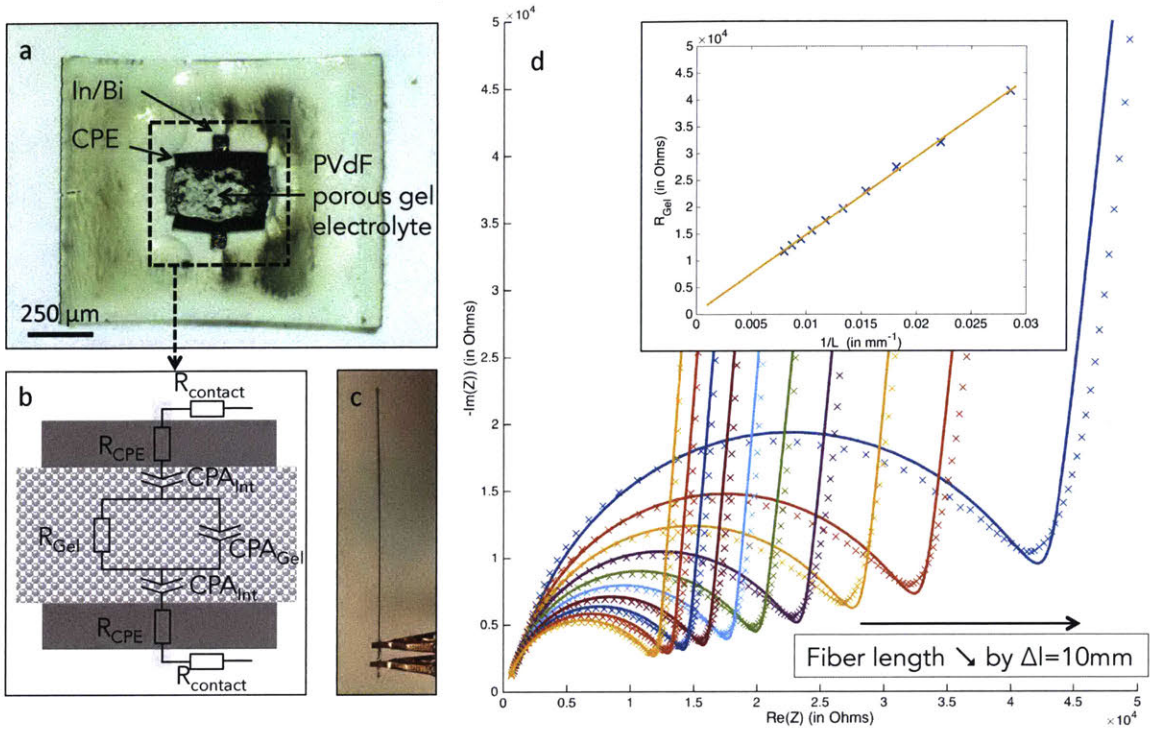

Figure 2-8: Transverse ionic transport measurement through impedance spectroscopy of ionic liquid-filled porous core fibers. (**a**) Optical micrograph of fiber sample displaying a porous core filled with a 10^{-3}m PYR13TFSI in PC solution, adjacent CPE electrodes, and contiguous Bi-In metal buses. (**b**) Simple equivalent circuit expected from fiber samples. CPA refer to Constant Phase Angle elements. (**c**) Photograph of a connected fiber sample. (**d**) Impedance spectra for a fiber between 12cm and 1cm, sequentially cut by 10mm decrements with best fit curves. The inset shows the dependence of R_{Gel} as a function of the inverse-length of the fiber and shows a linear relationship, as expected from geometric considerations.

posite electrodes, and metal buses within a single fiber is out-of-reach to standard extrusion-based processing methods for porous fibers. Here we are able to produce the fiber by initially combining the different materials in a prescribed architecture at the preform level, and subsequently inserting a solution in the core and drawing the preform into a fiber.

AC impedance spectroscopy

We then proceed to measure the ionic conductivity by AC impedance spectroscopy. This method consists in measuring the impedance of a sample over a wide frequency range, and mapping the results to a physically motivated equivalent circuit [MacCallum and Vincent, 1987]. In our case, the simplest equivalent circuit is presented in Fig. 2-8.b, following typical analysis of electrolyte systems. For a given fiber length, the CPE electrodes are counted for their resistive contribution through R_{CPE}, while the electrode/gel-electrolyte interface is modelled as a Constant Phase Angle element Z_{Int}^{CPA}. The bulk porous-electrolyte is modelled with a parallel circuit of a resistive component R_{Gel} associated with ion-transport in the liquid region, and a capacitive component in the form of a CPA element Z_{Gel}^{CPA} - taking into account polarization effects. CPA elements, also known as *Constant Phase Elements* are used in AC impedance models and data fitting to represent so-called "imperfect capacitor" behaviors. Their complex impendance is given by:

$$Z^{CPA} = \frac{1}{Q_0 \omega^n} e^{-jn\frac{\pi}{2}} \tag{2.2}$$

Where $n = 1$ describes an ideal capacitor of capacitance Q_0, while the case $n = 0$ represents pure resistor with resistance $1/Q_0$. In practice here we expect values of n to be close to 1.

To perform the measurement, we cut fiber samples to a specific length and seal the tips with wax to prevent solvent evaporation. Then we connect the fibers by mechanically exposing the metal buses on both sides, and connecting to the instrument using copper clips (Fig. 2-8.b). We measure the impedance over the frequency range 1MHz-100Hz, and gradually cut the fiber by 10mm increments. Data for a sample cut from 120mm to 10mm are shown in the form of Nyquist plots in Fig. 2-8.d, with the best fits obtained with the equivalent circuit detailed above. From the best fit results we can extract the resistance R_{Gel} - which in practice is close to the value of the diameter of the high frequency semicircle. Plotting this as a function of inverse length $1/L$ yields a linear relation (cf. inset of Fig. 2-8.d), as expected from geometric

considerations:

$$R_{Gel} = \frac{1}{\sigma_{Gel}} \times \frac{t}{w \cdot L} \text{ where: } \begin{cases} \sigma_{Gel} = & \text{conductivity of electrolyte} \\ t = & \text{thickness of electrolyte region} \\ w = & \text{with of electrolyte region} \end{cases} \quad (2.3)$$

By measuring the fiber dimensions with a microscope, we can use Eq. 2.3 to deduce σ_{Gel} from the slope of the insert curve in Fig. 2-8.d. We obtained an ionic conductivity of 2.87±0.47μS/cm (n=5 samples), compared to 2.6 μS/cm for the undrawn PVdF/PYR13TFSI/PC electrolyte with the same composition.

This experiment not only demonstrates our ability to produce complex fibers with multiple materials, but also that we are able to build functionality into the fiber. In this case we can add electrical capabilities by introducing conductive materials adjacent to the porous core, and use these capabilities to get information on the electrolyte contained in the core. This for example could be applied later on to smart textiles with the ability to intake and electrochemically monitor sweat.

2.4.2 Axial conductivity measurements

For axial transport demonstration, we also rely on ionic conductivity. We use fibers with neither CPE nor metal electrodes; just a PVdF/PYR13TFSI/PC gel core. Because of the difference in aspect ratios, we could not use the sample solution composition as for the transverse measurement - this would have led to impedance values outside the range of the instrument. Therefore we increased the concentration in ionically conductive species to 1m (mol/kg of solvent) PYR13TFSI in PC, and 1:4 wt. PVdF in PC.

We cut the samples to desired length and immediately applied low-temperature solder (Bi-In) on the tips. We then connected the samples to the impedance analyzer with copper clips, and performed impedance measurements in the frequency range 1Hz-1MHz. We cut the samples by 20mm decrements, ramping the size from 20cm to 2cm. We took the diameter for the high frequency semicircle as the value

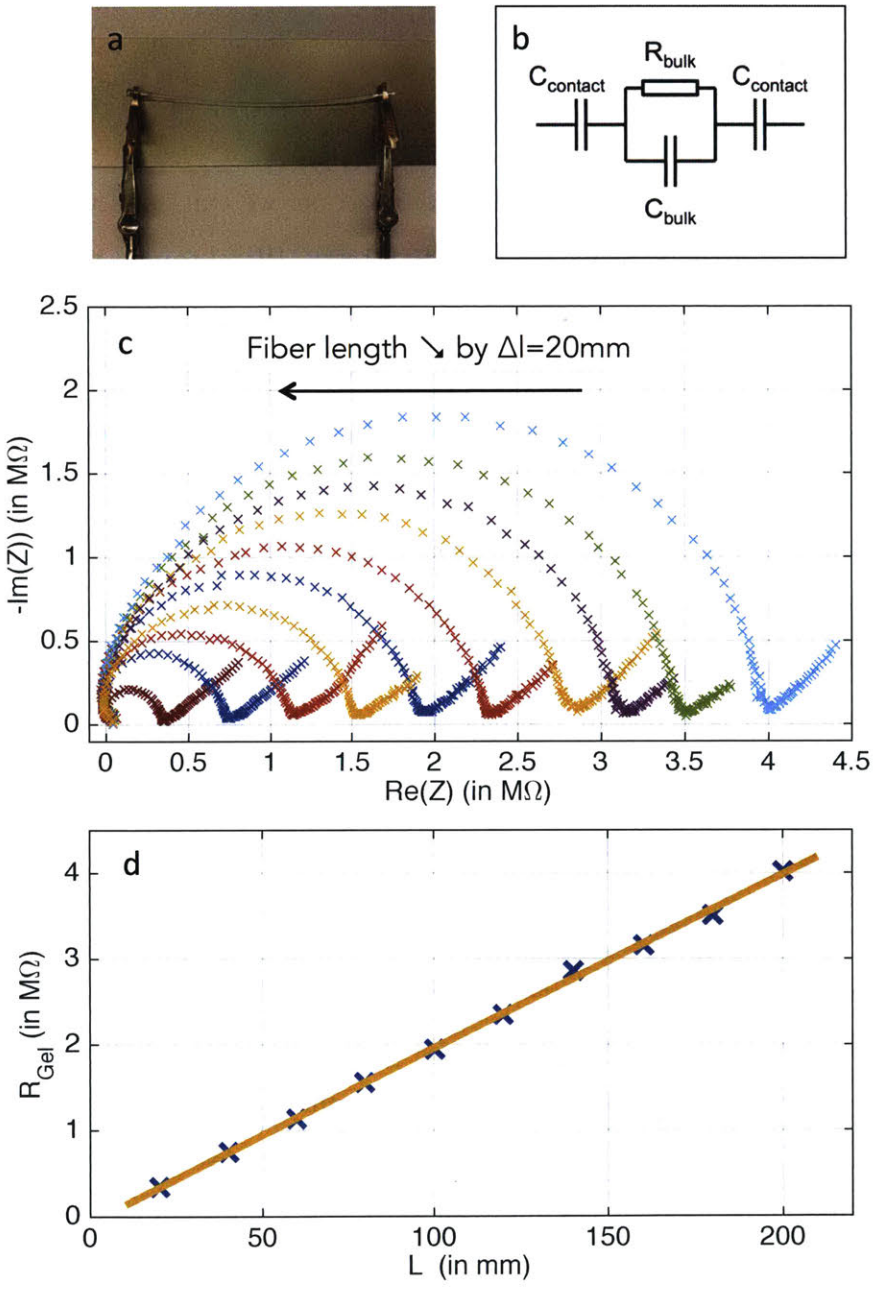

Figure 2-9: Demonstration of axial conductivity. (**a**) Photograph of a connected fiber sample. (**b**) Simple equivalent circuit. (**c**) Nyquist plots a sample from 20cm to 2cm, cut by 2cm decrement. (**d**) Plot of R_{Gel} as a function of fiber length L.

of the bulk resistance of the electrolyte. The bulk resistance of the electrolyte scaled linearly with length and the associated conductivity value from geometric considerations was found to be 6.4±0.6 mS/cm - comparing with 8.0 mS/cm for the undrawn PVdF/PYR13TFSI/PC electrolyte with the same composition.

2.5 Production of porous spheres through capillary breakup of porous fibers

Finally, the in-fiber TIPS method is not only a new platform for production of porous fibers, but it can also be harnessed to produce porous microspheres. To this end we build on previously established results regarding controlled capillary instabilities in thermally-drawn fibers [Kaufman et al., 2012; Gumennik et al., 2013; Kaufman et al., 2013].

2.5.1 Methodology

After the draw, we reheat the core/cladding fibers above the glass transition of the cladding material and critical temperature of the solution. The solution homogenizes and the cylindrical core evolves into a row of particles, under the effect of capillary forces. The timescale to complete breakup is a function of the core size, viscosity of both cladding and core, as well as the surface tension of the core/cladding interface. Depending on the sizes and processing temperature, this timescale is on the order of tens of minutes to hours. After the complete formation of spheres we can quench the sample and thus obtain a fiber whose core consists of a series of discrete porous particles, which can later be extracted by cladding dissolution. A schematic representation of this general process is shown in Fig. 2-10.a.

2.5.2 Results and discussion

By applying this method to COC cladding fibers with cores filled with either PCL or PVdF solutions, we obtained porous spherical particles of both polymers. We

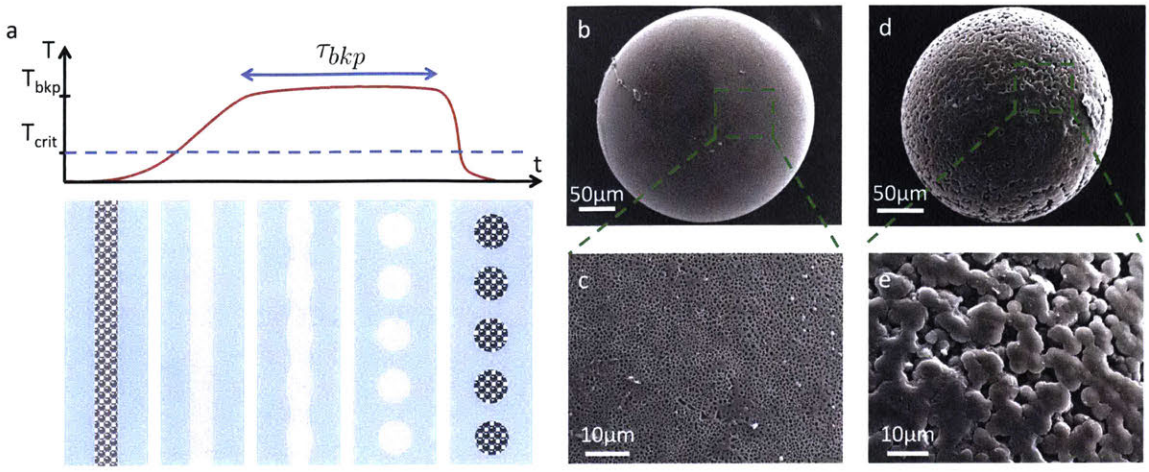

Figure 2-10: Porous microsphere production with controlled capillary breakup of porous core fibers. (**a**) General illustration of the capillary breakup process. Fibers are reheated above the phase transition temperatures of the solution and glass transition of the cladding. The core then evolves into a row of spheres under the effect of surface tension. Once breakup is completed samples are rapidly quenched. (**b,c**) SEM image and close-up of a PCL porous microsphere and of (**d,e**) a PVdF porous microsphere.

show SEM micrographs of both types of particles in Fig. 2-10.b-e. A timelapse of the capillary breakup step for a PCL-solution core/COC cladding fiber at 160°C is shown in Figure 2-11. Those particles could find applications in solid phase extraction or chromatography [Gokmen and Du Prez, 2012]. Furthermore, one could combine breakup with multimaterial porous fibers to generate structured multimaterial porous microspheres.

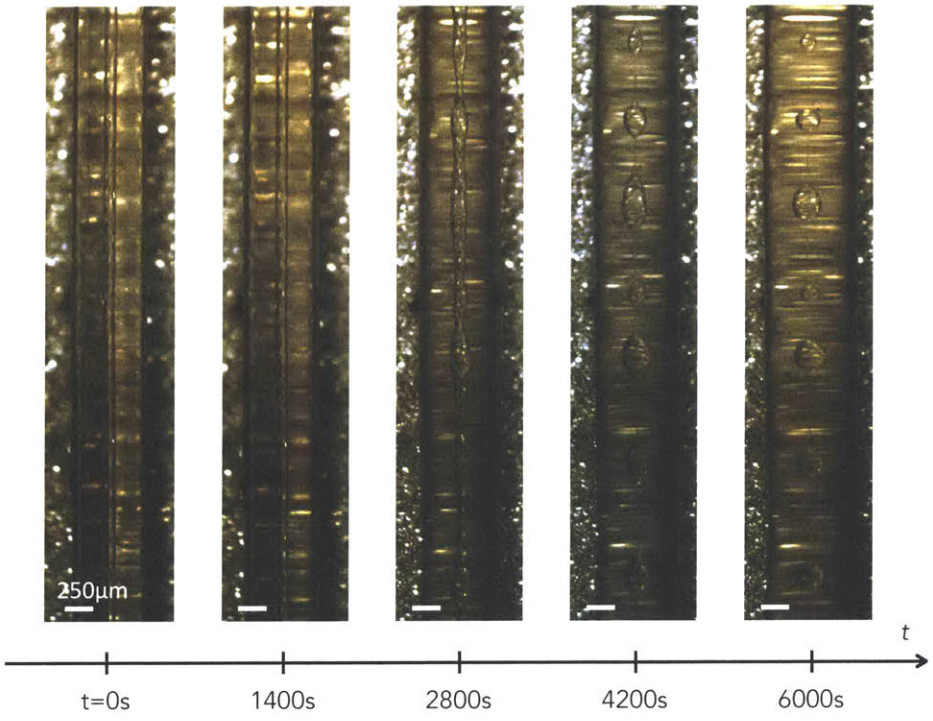

Figure 2-11: Timelapse of a PCL-solution core/COC cladding fiber undergoing capillary breakup at 160°C.

2.6 Discussion

The described method combines the advantages of fiber thermal drawing with the basic principle of thermally-induced phase separation of polymer solutions to produce unique porous fibers. The preform design process involves the choice of at least three materials: a polymer cladding and a solvent/polymer system as a solution. The set of constraints on the materials selection is the following:

1. the solvent used should not dissolve the cladding material in the processing temperature range;

2. the solution must not boil at the drawing temperature;

3. the solution must exhibit either a liquid-liquid or liquid-solid separation temperature between ambient temperature and the drawing temperature.

Despite these constraints, this new approach offers unparalleled possibilities for controlling the architecture and functionality of porous fibers. We have shown that we can dictate the external geometry of the fibers as well as tune the porous microstructure, and most importantly associate porous domains with non-porous domains of various materials within a single fiber. The as-drawn fibers can also be post-processed to produce porous microspheres of various materials. This preform-to-fiber TIPS method provides a compelling platform for the production of new types of porous fibers, and could enable a transition from passive fiber membranes to active multifunctional devices.

The following two chapters will revolve around this method for two different applications: the fabrication of a porous fiber neural scaffold, and the fabrication of a lithium-ion fiber battery.

Chapter 3

Fibers with external porous domains: Porous neural scaffolds

3.1 Motivations and background

3.1.1 Clinical need

The nervous system

The nervous system in the body consists of two main parts: the central nervous system (CNS), and the peripheral nervous sytem (PNS) [Kandel and Schwartz, 2013].

The CNS on the one hand is formed of the brain and the spinal cord. It performs the core function of the nervous system in that it collects, treats, and sends out information via neurons to the rest of the body. To prevent damage to the CNS, the brain is protected by the skull as well as the blood-brain barrier which keeps chemicals or unwanted substances in the blood from penetrating the brain, and the spinal cord is hosted in the vertrebral column.

On the other hand the PNS is made up of all nerves outside of the CNS, connecting it to the limbs and organs of the body. The PNS is namely responsible for transmitting sensory and motor information respectively to and from the CNS. Unlike the CNS, the nerves in the PNS are generally not protected by any bone or blood barrier. Because of that, the PNS is a lot more prone to injuries and nerve lesions with associated

symptoms such as paralysis or loss of sensory abilities [Kandel and Schwartz, 2013]. The regenerative ability of nerves and neural tissues is in general quite limited, thus often leading to permanent disabilities [Noble et al., 1998].

For small enough lesions ($\leq$ 2cm), the nerve may be able to regenerate on its own [Schmidt and Leach, 2003]. Axons from the proximal stump of the nerve (side of lesion closest to the CNS) can grow back and reconnect with the distal stump (side no longer connected with the CNS). Transected nerves with gaps larger than 2cm in general do not regenerate spontaneously. In fact because the distal stump is no longer connected to the nerve cell bodies and associated metabolic resources, it starts to degenerate and is eventually attacked by macrophages [Lee and Wolfe, 2000; Schmidt and Leach, 2003]. For such lesions, a surgical intervention is therefore necessary.

Types of surgical interventions

There are 3 main types of interventions for PNS injuries.

Direct suture The first type of intervention is direct end-to-end suture of the proximal and distal stumps (illustrated in Figure 3-1.a). This is only recommended if the suture can be achieved without introducing any kind of tension in the nerve [Schmidt and Leach, 2003], therefore direct suture is generally only appropriate for very small gaps or even adjacent stumps. In addition, even when possible, this type of intervention is only effective in about 50% of patients [Lee and Wolfe, 2000].

Nerve autograft For gaps around 2cm, when direct suture is not possible without producing significant tension in the nerve cable, the most common intervention is autologous nerve grafting [Schmidt and Leach, 2003]. A piece of nerve is taken from a donor site at another location in the body, and implanted and sutured at the injury site - as shown in Figure 3-1.b. Although this method is the gold standard for PNS nerve repairs, it has many shortcomings. Namely it necessitates multiples surgical interventions, and may result in loss of functions at the donor site [Schmidt and Leach,

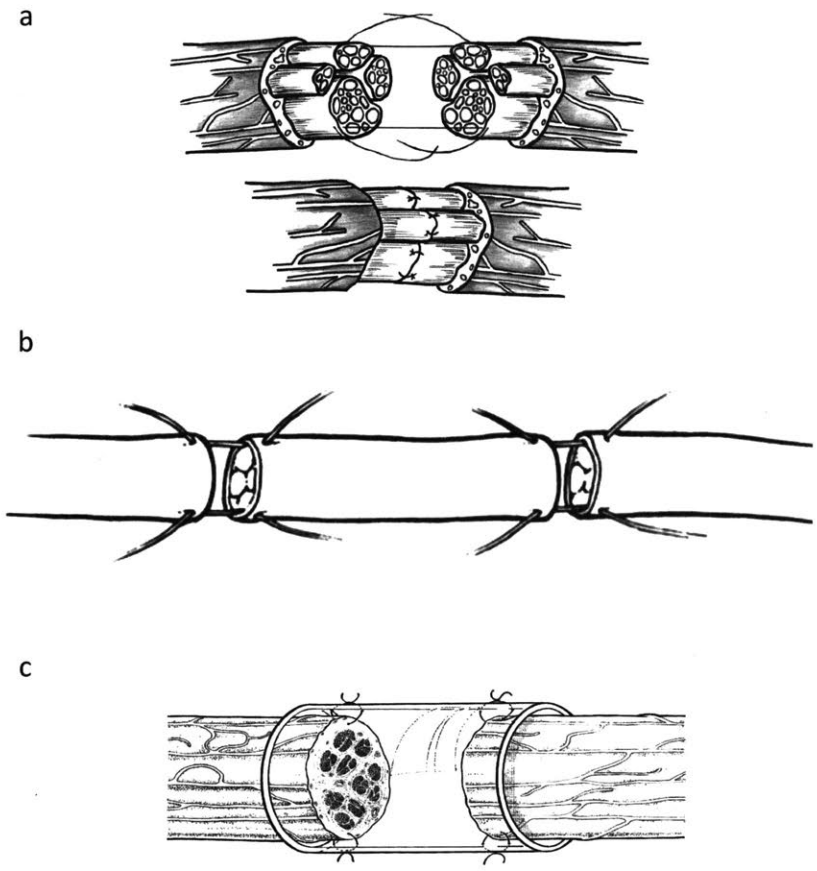

Figure 3-1: Schematics of the main surgical interventions for peripheral nerve repair. (**a**) From Schmidt and Leach [2003]: Direct nerve suture. (**b**) From Newton and Nunamaker [1985]: Nerve autograft; the central portion being a nerve transplanted from a donor site elsewhere in the body. (**c**) From Lundborg [2000]: Insertion of a nerve guidance conduit to guide regeneration.

2003]. Furthermore functional recovery is not guaranteed, and highly improbable for gaps larger than 4cm [Robinson, 2000].

Implantation of a nerve guidance channel When the availability of donor sites is scarce or for gaps larger than 3-4cm, implantation of a nerve guidance conduit may become the preferred option over autologous nerve grafting. The principle is to insert at the injury site an artificial conduit to guide axonal regrowth and bridge the proximal and distal stumps [Schmidt and Leach, 2003]. To this date only a few devices have been FDA-approved, however none truly outperform autografts [Kehoe

et al., 2012]. A large research effort is therefore underway to develop new devices that would provide a real therapeutic alternative.

3.1.2 Overview of neural scaffolds

In general for tissue engineering, the ideal synthetic scaffold aims at mimicking the actual tissue as well as displaying relevant cues to both accelerate and organize the cell regrowth. For nerves, these cues can be chemical gradients and presence of neurotrophic factors [Boyd and Gordon, 2003], topographical constraints [Hoffman-Kim et al., 2010; Kim et al., 2008], electrical stimulation [Schmidt et al., 1997; Al-Majed et al., 2000], or in more recent studies optical stimulation on optogenetically modified neurons [Park et al., 2015]. Hudson et al. define the properties of an ideal nerve guidance conduit, in addition to obvious biocompatibility and implantability.

Materials

The materials that have been investigated broadly fall in two categories: biopolymers and synthetic polymers.

Biopolymers Biopolymers are polymeric molecules from biological origin, *i.e.* that are produced by living organisms. They are generally either proteins, polysaccharides, or polynucleic acids. In the context of nerve guidance scaffolds, proteins like collagen [Alluin et al., 2009], gelatin (denatured collagen) [Gámez et al., 2004], chitosan [Wang et al., 2006], or silk fibroin [Madduri et al., 2010] have been investigated, as well as polysaccharides like alginate [Suzuki et al., 1999]. In general, the advantages of using such polymers in the context of tissue engineering are their high biocompatibility, and intrinsic bioactivity and ability to mimic the extra-cellular matrix of the cells. The main drawbacks however are the difficulties to synthesize and the large batch-to-batch variations in bio-sourced polymers, in addition to the difficulty to tune mechanical properties or biological responses.

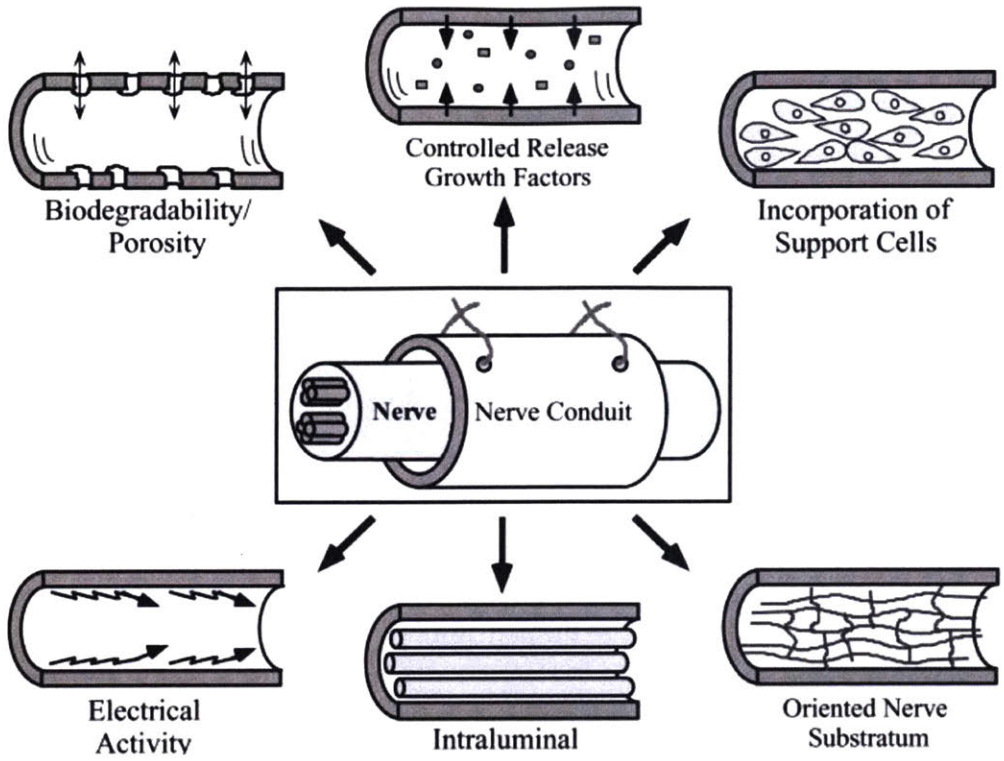

Figure 3-2: Ideal properties of a nerve guidance conduits as defined by Hudson et al.. From top left clockwise: scaffold porosity for nutrient transport and biodegrabability for reduced scarring and nerve compression; slow release of growth factors; ability to pre-incorporate support cells to help regeneration; internal oriented matrix to guide cell migration; intraluminal channels to mimic fascicular structure of nerves; electrical activity to monitor and stimulate regrowth.

Synthetic polymers By definition synthetic polymers refer to any man-made polymer, not naturally present in the world. Research on neural scaffold materials has primarily focused on biodegredable polyesters already found in FDA-approved devices, the most common being: polylactic acid (PLA), poly(L-lactic acid) (PLLA) [Evans et al., 1999], polyglycolic acid (PGA), poly(L-glycolic acid) (PLGA) [Widmer et al., 1998], poly-ϵ-caprolactone [Vleggeert-Lankamp et al., 2007] as well as some of their copolymers [Nakayama et al., 2007; Dadaci et al., 2016]. Typically, synthetic polymers enable more precise control on composition and therefore ability to tailor mechanical properties, degradation rates, and chemical interactions with cells. It is worth noting that non-degradable polymers have been used as well, such as polyvinyl alcohol (PVA) [Rutkowski and Heath, 2002], or more recently studies around conductive polymers like polypyrrole (PPy) [Lee et al., 2009] or polyaniline (PANi) [Zhang

et al., 2014] in hybrid degradable/nondegradable structures.

Fabrication processes

The objective in making a neural guidance scaffold is to produce a tubular structure with dimensions close to a nerve cable and commonly porous. To achieve this, a varietey of fabrication processes have been utilized such as dip-coating, injection molding, braiding, and electrospinning [Wang and Cai, 2010; Arslantunali et al., 2014]. In dip-coating a mandrel is dipped and removed from a bath containing a polymer solution so as to viscously entrain a layer of solution on the mandrel , which can then either be photocured, or forced to phase-separate by immersion into a non-solvent bath or freezing [Wang and Cai, 2010]. For injection molding, a solution is cast into a mold defining the conduit shape - and post-processed in similar ways as in dip coating to generate a solid porous structure in the mold [Wang and Cai, 2010]. Perhaps the most widely investigated method for nerve scaffold production is electrospinning. In electrospinning, a solution (or a melt) o polymer is extruded through a syringe, and a high voltage ($\approx$kV) is applied between the liquid and the substrate [Wang and Cai, 2010; Arslantunali et al., 2014]. The high voltage drives the formation of submicron size threads, which deposit on the substrate. A tubular structure can be realized for example using a rotating cylindrical mandrel as substrate. One of the main advantages of electrospinning is the built-in porosity along with the the submicron-filamentous structure which can be harnessed to promote neuronal guidance - while challenges include the difficulties to precisely control the geometry of the final device over multiple lengthscales [Arslantunali et al., 2014]. More recently, neural scaffolds have also been produced using 3D-printing. Johnson et al. show that they can use 3D scanning of an injured area to 3D print a hydrogel-based guidance channels precisely matched to the injury site, and preloaded with slowly-releasing nerge growth factor.

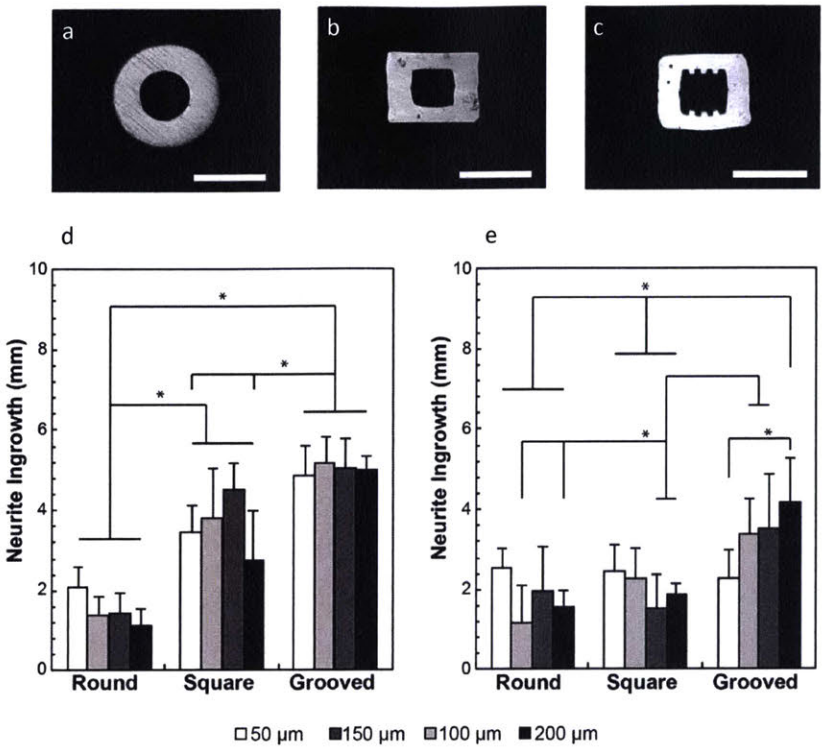

Figure 3-3: From Koppes et al.: Thermally drawn fibers as nerve guidance scaffolds. (**a-c**) Cross-sectional images of round, square, and grooved PEI fibers. Scalebars are 200 μm (**d,e**) Neurite ingrowth in fibers of different shapes and sizes; (**d**) shows data for 5mm-long fiber samples while (**e**) shows data for 10mm-long fiber samples.

Common limitations

Despite successes of various designs both *in vitro* and *in vivo*, current scaffold technologies still fall short of the ideal scaffold illustrated by Hudson et al., in particular in their ability to combine modalities to stimulate nerve regenaration. As we have seen, axongal growth can be influenced by chemical, topographical, electrical, or optical cues. The various fabrication processes used in general prevent or impede the ability to combine multiple materials with different functionalities, as well as pattern the scaffold structure over multiple lengths scales - thereby limiting their functionality.

3.1.3 Thermal-drawing for neural scaffolds: current results and setbacks

Recent work from Koppes et al. focused on using the thermal-drawing process to produce fiber nerve guidance scaffolds. The preform-to-fiber thermal drawing method indeed enables the fabrication of fibers and tubular structures combining different materials with well-defined geometries and structures from the submicron scale to the millimeter scale - thereby presenting topographical and geometrical cues to the neurons. Furthermore if offers the possibility to combine multiple materials such as electrodes for electrical stimulation or waveguides for optical stimulation. Therefore the thermal-drawing process appears as a very promising method for advanced multifunctional fiber scaffolds.

The aim of the study by Koppes et al. was to first demonstrate that the thermal-drawing process could be a suitable production method for neural scaffolds, as well as to perform a detailed analysis of the influence of channel size, shape, and topography on neurite growth inside dense polyetherimide (PEI) fibers.

Among other results, Koppes et al. were able to show that in their PEI fibers:

- Neurites growing in square grooved cross-section fibers extended more than in round or square and ungrooved cross-section fibers of similar sizes.

- Neurites growing from a single source in 5mm samples extended more than when growing in 10mm samples.

The last point seems counter-intuitive: neurite extension is larger in smaller devices. This was attributed to the diffusion-limited growth of the neurites: nutrients diffuse more slowly into longer devices therefore limiting growth. In this chapter, we wish to extend upon the results of Koppes et al. by employing the method and results presented in Chapter 2 to produce porous fiber scaffolds with tunable structures and functionalities.

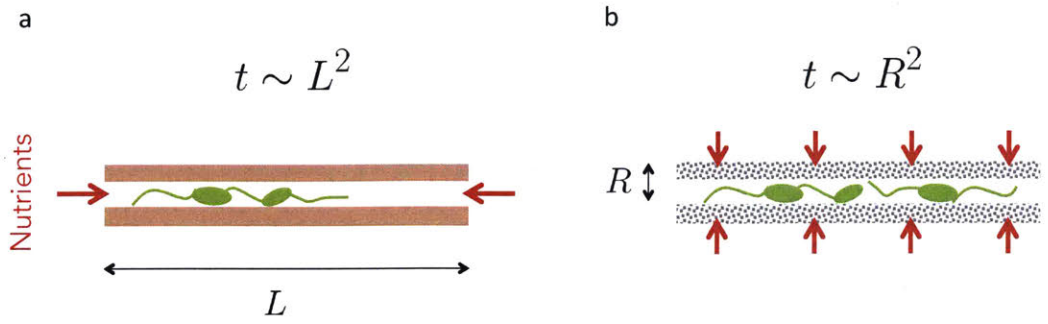

Figure 3-4: Schematic comparison of nutrient supply with dense fibers (**a**), and porous wall fibers (**b**).

3.2 Fiber scaffold design and fabrication pathway

3.2.1 Rationale for porous fibers

When growing neurons in dense PEI fibers, we have seen that maximum neurite extension is smaller in long fiber samples than in short fiber samples. This is indicative of a nutrient-diffusion-limited growth. In dense fibers, nutrients can only diffuse from the fiber edges into the core. Therefore the characteristic time for nutrient supply to growing neurons scales as the the length of the fiber squared, owing to the kinetics of the diffusion transport. In addition, dense fibers induce a risk of neuron "self-suffocation" in the event where neuronal growth induces a complete or partial blockage of the hollow-core. On the contrary with a porous fiber the nutrients could in principle diffuse from the environment to the core directly through the porous cladding of the fiber, as illustrated in Figure 3-4. Therefore the characteristic nutrient supply time would be independent of sample length, and scale only as the radius of the fiber squared.

3.2.2 Challenges in drawing a hollow-core porous fiber

Contstructing a hollow-core/porous cladding structure similar to a hollow-fiber membrane is challenging with our fabrication method. In our preform-to-fiber method, the preform is a template for the final porous fiber we wish to produce. Templating a

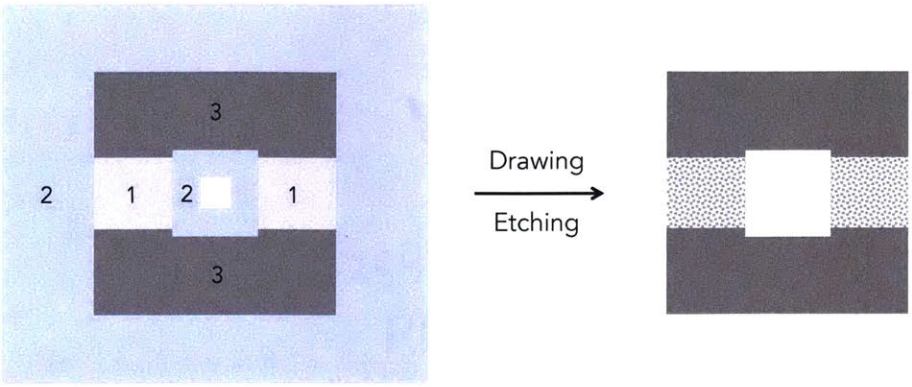

Figure 3-5: Schematic of the preform and fiber cross-sections in an ideal case.

fiber with a hollow-core is difficult, because during the draw the core needs to be filled with a viscous fluid immiscible with the solution (and in particular insoluble in the organic solvent used for the solution) that would later be dissolved. In practice this could be achieved using a center element of the same material as the cladding filling the hollow-core region during the draw and later dissolved; however maintaining the viscous core in the center during the draw is challenging, as it will tend to buckle when surrounded with very low viscosity solution.

3.2.3 Fiber design and materials selection

In our approach, we designed a preform cross-section schematically shown in Figure 3-5. Each region in the preform has a particular role during the draw:

- The light grey regions (regions **1**) should be filled with a polymer solution during the draw, leading to porous domain in the final fiber.

- Blue regions (regions **2**) represent a material resistant to the polymer solution solution but that will be etched out in an appropriate solvent after drawing. In particular, the region at the center of the preform would lead to the hollow-core in the final fiber after dissolution. It could contain a hollow core for faster dissolution.

- The dark grey regions (regions **3**) should be a co-drawable material that is

resistant to the solvent used in the polymer solution as well as the solvent used to dissolve the cladding material. During the draw, it should be viscous enough so as to maintain the green core at the center of the fiber and avoid buckling.

In terms of materials selection, in addition to constraints listed above, the materials in the final fiber should all be biocompatible. We have chosen poly-ϵ-caprolactone (PCL) as our porous material because of its excellent biocompatibility, existing literature as neural scaffold material, as well as our ability to process it to form porous domains in fibers (cf. Section 2.2.2). The cladding and core material was chosen to be cyclic olefin copolymer (COC), again for our ability to process it and etch it selectively from PCL. Finally, we chose low-density polyethylene (LDPE) as our support material. Again, we demonstrated co-drawability of LDPE with PCL solution and COC as well as its ability to resist the COC etching process in Section 2.3.1.

With these materials, careful preform preparation, drawing, and COC etching should in principle leave a final fiber with a cross-section shown in Figure 3-5. A hollow-core hosting neuronal growth adjacent to two porous windows enabling transverse nutrient transport, along with two dense supports providing mechanical stability to the fiber. However the key issue in realizing the structure presented in Figure 3-5 is to guarantee the adhesion between PCL and LDPE regions. In fact when no special attention is given to this issue, drawn fibers lead to samples that systematically delaminate upon COC etching - and are therefore not useable.

3.3 Adhesion enhancement between PCL and LDPE

3.3.1 Intrinsic adhesion issue

Adhesion in general refers to the collection of forces causing different materials to stick to one another. Adhesion is an intrinsically multiscale phenomenon where intermolecular forces, surface topography, and shape add up to a macroscopic behavior. Adhesion can in general be mediated by three main classes of intermolecular forces [Israelachvili, 2011].

Chemical bonding The first one is known as chemical adhesion, where the molecules of two dissimilar materials interact at the interface to form either covalent, metallic or ionic bonds. Hydrogen bonding is sometimes added to this category although not a chemical bond *per se*. If materials joint at an interface do not spontaneously form any chemical bonds, chemical bonding can be mediated by an adhesive.

Van der Waals bonding When disparate materials are brought in contact they may interact at the molecular scale through van der Waals forces, finding their origins in dipole-dipole interactions between molecules at the interface. Despite being of a much lower magnitude than covalent bonds ($\approx$10 kJ.mol^{-1} compared to 200-800 kJ.mol^{-1} for covalent bonds [Israelachvili, 2011]), these forces can still lead to macroscale adhesion through high surface polarity and large effective surface areas. The gecko's adhesion to many substrates is a classic example of van der Waals adhesion [Autumn et al., 2002].

Diffusive bonding In diffusive bonding molecules from the two materials brought in contact interdiffuse in one another, eventually joining the materials together. Diffusive bonding can dominate when the two materials brought in contact are compatible or miscible to some extent in one another [da Silva et al., 2011]. It can be particularly useful for polymer-on-polymer adhesion, provided long polymer chains from one material can diffuse and extend into the second material thus molecularly "interlocking" both materials.

In our case, PCL and LDPE do not spontaneously form any type of covalent bonding at their interface, furthermore van der Waals and electrostatic interfactions between the two materials are not enough to hold the materials together at the fiber level. Diffusive adhesion also does not contribute to any significant adhesion, because of the low solubility and interdiffusion of PCL and LDPE - which is in fact quite common for two disparate polymers. We therefore need to devise a method to enhance the adhesion without sacrificing drawability.

3.3.2 Surface grafting protocol

General method

In general using copolymers A/B as an interfacial compatibilizer is a common solution to increase the adhesion between two polymers A and B [da Silva et al., 2011]. The method we have developed follows this idea, and consists in surface-polymerizing chains of PCL directly onto an LDPE surface. This creates a covalent bond between LDPE chains and extending chains of PCL grafted on the surface of LDPE (cf. Figure 3-6.a). When laminating a film of surface-modified LDPE with a film of PCL, the grafted PCL chains will interdiffuse into the PCL film while being covalently attached to LDPE. Adhesion between both materials will therefore result from the combination of chemical and diffusive adhesion.

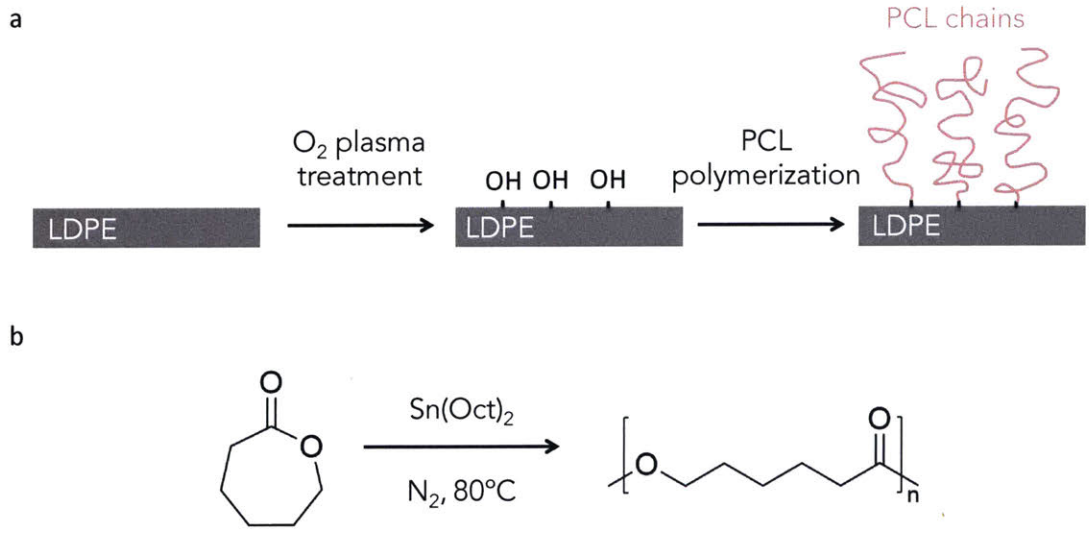

Figure 3-6: (**a**) Schematic description of the surface grafting protocol on LDPE. First step is the O_2-plasma treatment to introduce hydroxy-group on the surface of LDPE; second step is the PCL chain polymerization. (**b**) General ring-opening polymerization mechanism of PCL from ϵ-caprolactone monomer with a stannous octoate catalyst.

Detailed protocol

Here, we wish to polymerize PCL directly on top of an LDPE surface. PCL can be polymerized from ϵ-caprolactone as monomer through a ring-opening polymerization (ROP), using a wide range of catalysts and solvents [Labet and Thielemans, 2009]. For the following, we focused on the most common catalyst, stannous octoate ($Sn(Oct)_2$) [Labet and Thielemans, 2009], and did not use any solvents during polymerization to avoid LDPE dissolution. A schematic of the polymerization mechanism is shown in Figure 3-6.b. In order for the chains to polymerize on the surface using $Sn(Oct)_2$ as catalyst, the reaction should be initiated from hydroxy -OH groups [Labet and Thielemans, 2009]. With no pretreatment, the surface of LDPE is relatively inert and does not contain many hydroxy groups from which PCL can start polymerizing. Therefore, we start the process by introducing -OH groups on the surface of LDPE through oxygen plasma treatment. Oxygen plasma was indeed reported to introduce a variety of oxygen-containing functional groups on the surface of LDPE in particular -OH groups, rendering the surface hydrophilic [Sanchis et al., 2006; Patra et al., 2013]. In our process, the LDPE sample can be a bulk preform part or a film.

Following O_2-plasma treatment for 10 min, High RF power and a pressure of 1000 mTorr of O_2, LDPE samples are rapidly transferred in a 3-neck 1L flask half-filled with ϵ-caprolactone monomer with $Sn(Oct)_2$ catalyst, in a 72.6.:1 wt:vol ratio, chosen according to Labet and Thielemans. The flask is set up in a Schlenk line where the polymerization is allowed to happen at 80°C under nitrogen for 24 hours, and stirred with a magnetic stir bar around 300 rpm. The reason why the samples are transferred rapidly is because reports have shown that functional groups introduced on LDPE from O_2-plasma treatment are relatively short-lived, and the surfaces tend to restore to their initial state within hours [Sanchis et al., 2006]. In our case, a typical sample transfer time between the end of the plasma treatment and the flask setup in the Schlenk line is around 10 min.

After polymerization, we remove the LDPE samples from the flask and rinse them in chloroform for 2 hours to dissolve away any PCL homopolymer not covalently-

bound to the LDPE surface. We then dry the LDPE samples overnight under vacuum.

3.3.3 Adhesion testing at the preform level and role of roughness

Adhesion testing at the preform level

In order to quantitatively test our idea, we performed our surface grafting protocol on 1mm×20mm×50mm LDPE samples. Following the surface-grafting protocol we observed the surfaces under SEM and performed an energy dispersive spectroscopy analysis (EDS) to quantify the oxygen content at the surface (cf. Table 3.1). This high oxygen content at the surface of the surface-modified LDPE is indicative of a successful polymerization.

Sample	Average oxygen content (at. %)
Untreated LDPE	4.21 ± 0.05
Plasma treated LDPE (24hrs after treatment)	5.27 ± 0.08
Surface-grafted LDPE	15.95 ± 1.62

Table 3.1: Oxygen content in atom % on the surface of LDPE films measured by energy dispersive spectroscopy.

We also proceeded to test adhesion strength of the modified LDPE sheets with pure PCL. First, we laminated our LDPE samples with 1mm×30mm×60mm pure PCL films (PCL $M_n \approx$ 80k, Sigma-Aldrich). We achieved lamination by stacking LDPE and PCL films on a glass slide, and placing the glass slide on a hot plate set at 220°C for 5min - followed by immediate removal of the glass slide and natural convective cooling. Qualitatively, laminates formed from untreated LDPE samples and PCL spontaneously delaminated either from cooling or from any minor vibration due to handling. On the opposite, laminates formed from treated LDPE and PCL were quite robust and mechanically stable when handled.

Laminated samples were cut into 1mm×4mm×45mm strips and used for quantitative adhesion strengths measurements. For this we employed a T-peel test, depicted schematically in Figure 3-7. The principle is to measure the force required to peel

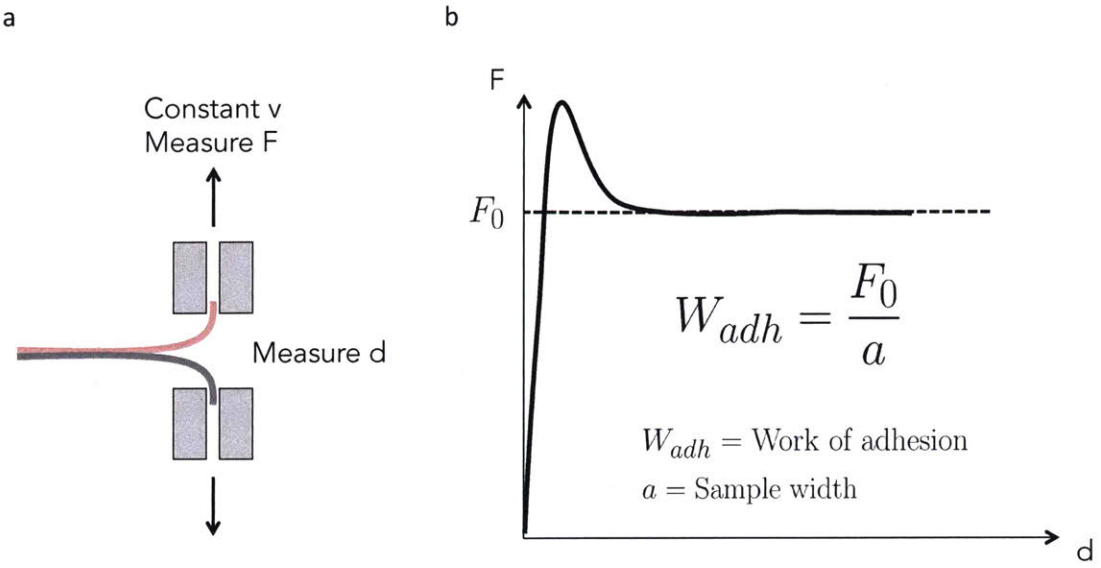

Figure 3-7: (**a**) Schematic of T-peel test. Laminates of LDPE and PCL are clamped and pulled apart at a constant velocity in a mecahnical tester while measuring the force. (**b**) Ideal Force vs. Separation distance curve obtained from a T-peel test. After an initial overshoot, the force stabilizes to a constant related to the work of adhesion through the relation displayed.

apart both materials for a strip of constant width. In the case where neither material undergoes strong plastic deformation, it is assumed that the input energy is entirely used to separate the surfaces [da Silva et al., 2011]. In such case the adhesion strengths can be directly deduced from the force and width by $W_{adh} = \frac{F_{avg}}{a}$. We measured works of adhesion on the order of 100-250 N/m, comparable for example to the adhesion of a commercial bandage on skin.

Role of roughness

Our surface polymerization protocol grafts PCL chains on the surface of LDPE, which will act as anchor points for the adhesion. Increasing the grafting density at constant PCL chain molecular weight should lead to an increase in adhesion. Alternatively, increasing the effective surface area by introducing roughness on the interface should also lead to an effective increase in grafting density and should result in an increased adhesion.

We tested this idea by preparing LDPE samples that we sanded with different grit

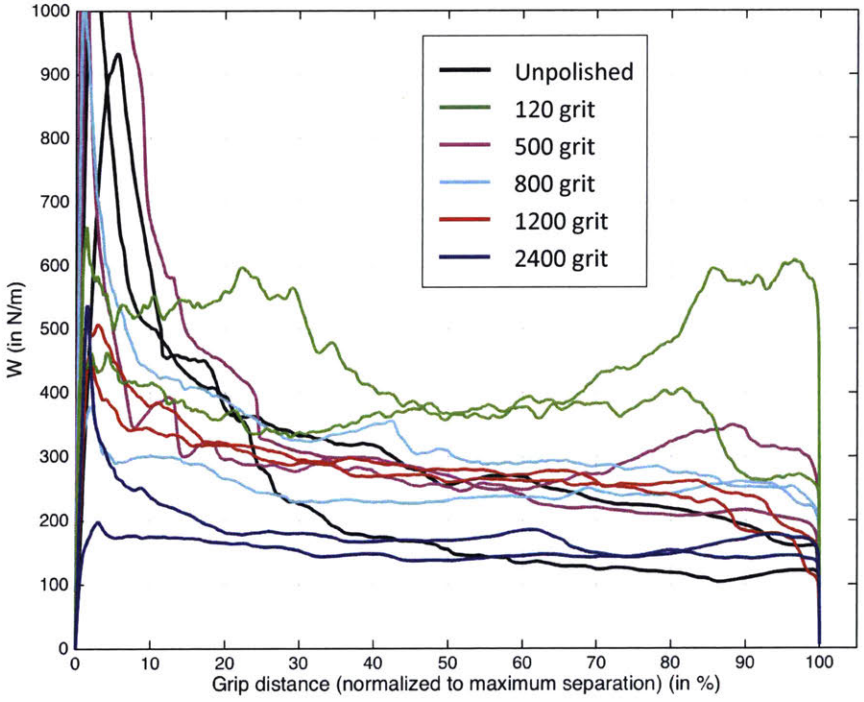

Figure 3-8: T-peel curves obtained from surface-grafted LDPE/PCL laminates for different roughnesses on LDPE - two measurements for each condition.

size sandpaper prior to undergoing O_2-plasma treatment and surface polymerization. The results in terms of adhesion strengths are shown in Figure 3-8. They show a relatively small impact of roughness on adhesion strengths. In addition, the influence of roughness on adhesion strengths seems to be decreasing with grit size with an apparent maximum for samples roughened with 120 grit size paper. We believe this is due to the fact that higher grit size papers introduce a finer roughness which may eventually influence the polymerization kinetics either by chain hindrance or diffusion-limited supply of monomer to the reaction sites.

3.3.4 Adhesion at the fiber level

Our initial goal was to avoid delamination between porous PCL and LDPE at the fiber level. To test whether our surface polymerization method in fact leads to in-fiber adhesion, we first prepared simple preforms with cross section shown in Figure 3-9. The aim of these preforms was to test adhesion at the fiber level of LDPE and porous PCL for a single interface, and for two interfaces respectively. Here, the bulk LDPE preform slabs were first machined, their surface roughened with 120 grit size paper, washed with isopropyl alcohol, and then underwent as such the O_2-plasma treatment and surface polymerization on the relevant surfaces in a 1L flask. After rinsing in chloroform and drying, the treated LDPE part was milled in its upper section to machine off 100μm of material. This creates a region with no treated surface that we can use as a reference to test the impact of the surface grafting approach on the adhesion in the fiber. The treated LDPE parts were directly used to assemble the preforms. After consolidation, we filled the hollow channel of the preform with a solution of 1:6 wt. PCL (Mn $\approx$80k) in 1:1 wt. PC/Triglycol, prepared at 220°C and poured directly into the channel - similar to the method described in Section 2.2.2. The preform was set in the draw tower immediately after insertion of the solution and drawn.

After drawing, we dissolved the COC in cyclohexane overnight. Fibers originating from the untreated top section of the preform delaminated in the vial upon COC etching; while fibers from the treated LDPE section remained in a single piece - as

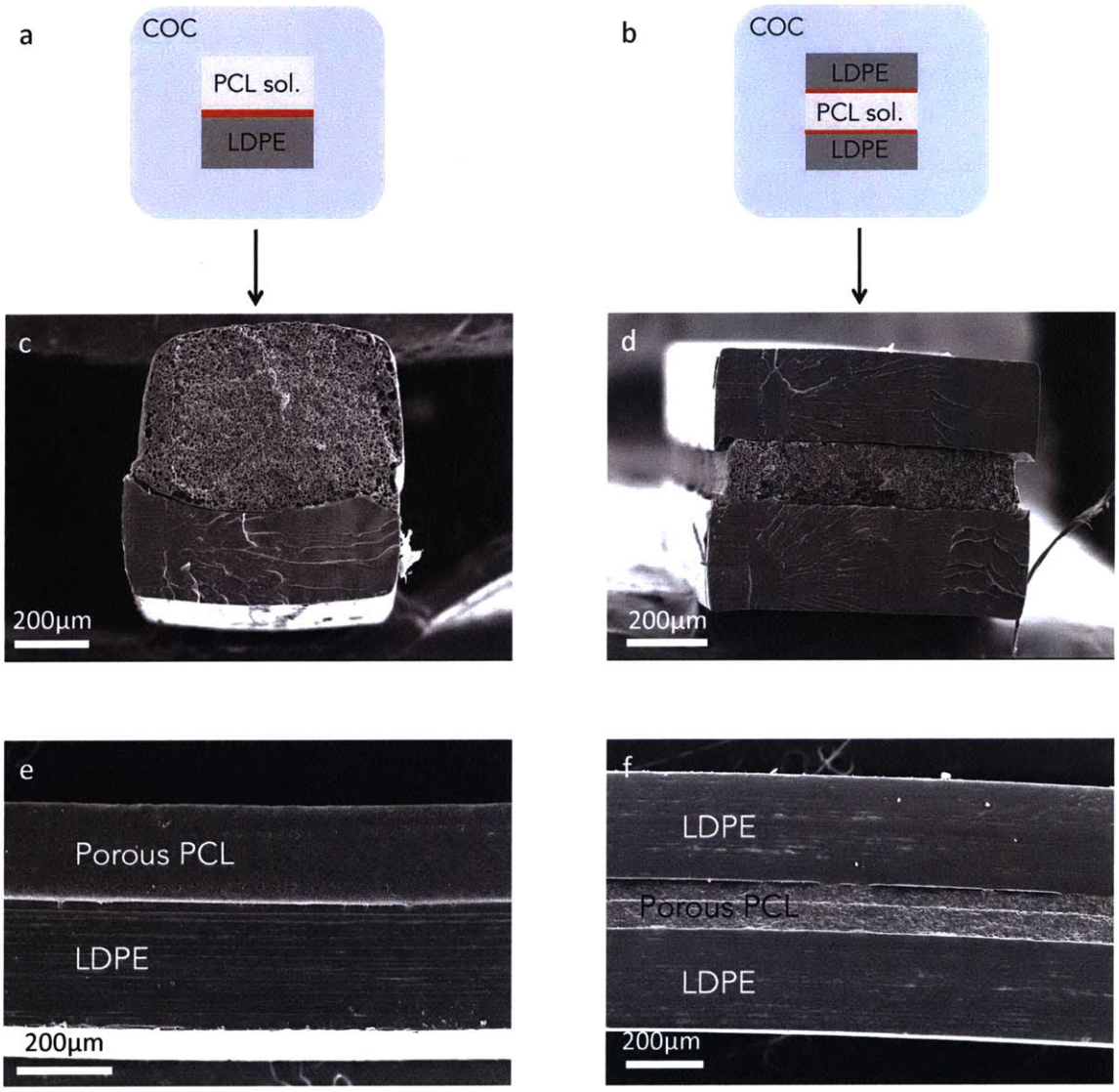

Figure 3-9: (**a, b**) Schematics of the preforms designed for fiber-level adhesion testing. The red line at the interface of PCL solution region and LDPE indicates the surface-grafted LDPE interface. (**c, d**) Cross-section SEM images of the fibers obtained after drawing and COC etching. (**e, f**) Longitudinal SEM view of the above fibers.

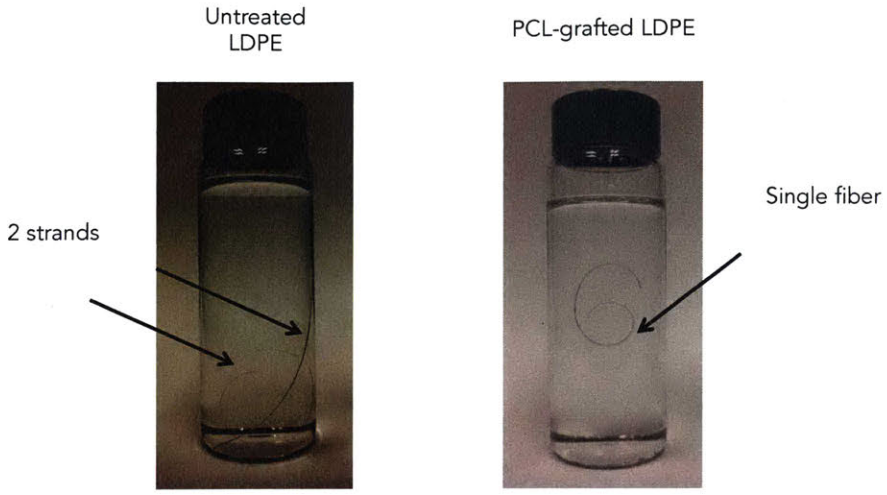

Figure 3-10: Photographs of fibers obtained from the preform described in Figure 3-9.a after COC etching. On the left, a fiber in the preform region where LDPE was not surface-treated; the fiber delaminates into two strands, LDPE and porous PCL respectively. On the right, a fiber from the preform region where LDPE was surface-grafted with PCL; the fiber stays in one piece.

evidenced by the photographs in Figure 3-10. The latter fibers were very resilient to handling, and did not show any sign of delamination even when twisted or bent. Quantitative measurement of the adhesion strength could however not be made, since the force levels required to split the fibers lie below the force resolution of the Zwick mechanical tester we used - essentially because of the small contact area between both materials in the fiber.

We imaged the intact fibers under SEM after freeze-fracturing the samples. Typical cross-section is shown in Figure 3-9.c-d. The freeze-fracture process sometimes introduced defects and small gaps between PCL and LDPE on the cross section, but we imaged the fiber longitudinally as well to confirm the adhesion along the length and far away from the freeze-fracture plane (cf. Figure 3-9.e-f).

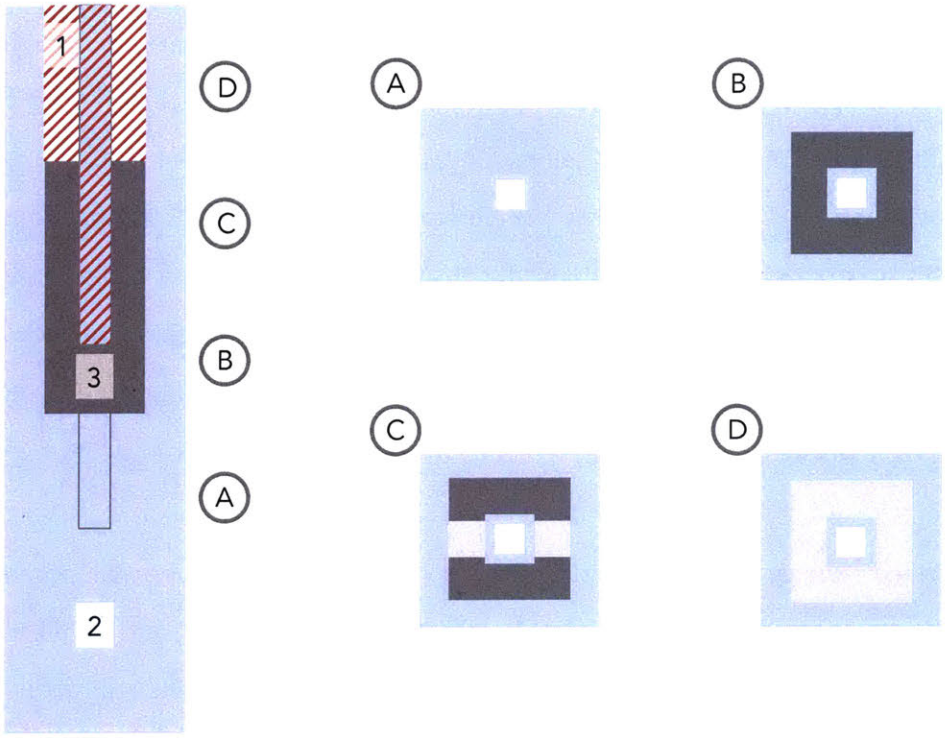

Figure 3-11: Schematic of the scaffold preform assembled. On the left, a longitudinal cross-sectional view of the preform. Region 1 contains the PCL solution forming the porous domain; region 2 is COC; region 3 is LDPE. **A,B,C,D** show the preform cross-sections at different locations, from first drawn to last. Region **C** is the actual scaffold region of interest.

3.4 Fiber scaffold fabrication and characterization

3.4.1 Fiber fabrication and morphological characterization

We proceeded to built the preform structure shown in Figure 3-11, where region (C) is the actual scaffold region.

LDPE machining and surface-grafting Following the path explicited in Section 3.3.4, we first machined LDPE slabs into their desired preform geometry and size. The preform parts were then roughened with 120 grit size paper, washed, and underwent O_2-plasma treatment and surface polymerization. The parts were then rinsed and dried and used to assemble the preform.

Preform assembly and consolidation To produce the preform with the cross-section shown in Figure 3-5. we used the treated LDPE parts and machined all COC parts individually to the correct size. In addtion, we machined PTFE inserts to fit with a 100-μm precision in the hollow-channels of the preform. All parts are cleaned with IPA prior to assembly. With careful machining of all individual parts, the assembly process is trivial. The preform was consolidated in a hot press at 110°C for 6 hours. In the press, the preform was gently clamped on both sides to two aluminum spacers delimiting a 1.5mm gap between the unconsolidated preform and the hot press' surface.

Preform drawing The preform channels to host the polymer solution were too small for the solution to be poured in directly. Due to its viscosity, the solution would clog the channels and prevent proper filling. To circumvent this issue, we cast the solution in a grooved PTFE mold with groove sizes corresponding to the channel size, and let the solution phase separate and solidify in the mold. Then, we inserted the phase separated solid gels into the preform channels by hand. The idea behind this method is that once in the draw tower furnace, the solution would rehomogenize. After gel insertion, the preform was set in the draw tower and drawn into a fiber.

SEM characterization of fibers After drawing, we cut 6cm samples along the length of the fiber and etched out the COC cladding as well as the center core in cyclohexane overnight. We obtained non-delaminated fibers from a region of about 5m long on the 40m total length of drawn fiber. The relatively poorer adhesion compared to fibers shown in Section 3.3.4 was attributed to both batch-to-batch variation in the surface grafting process, as well as lower surface area of contact between LDPE and PCL in a given fiber sample - indeed the hollow core region does not participate in adhesion.

Intact samples were freeze-fractured and imaged using a SEM. Cross-sections of various region are shown in Figure 3-12. Overall, the cross section were very close to the intended structure. One notable deviation is the "butterfly" shape of the

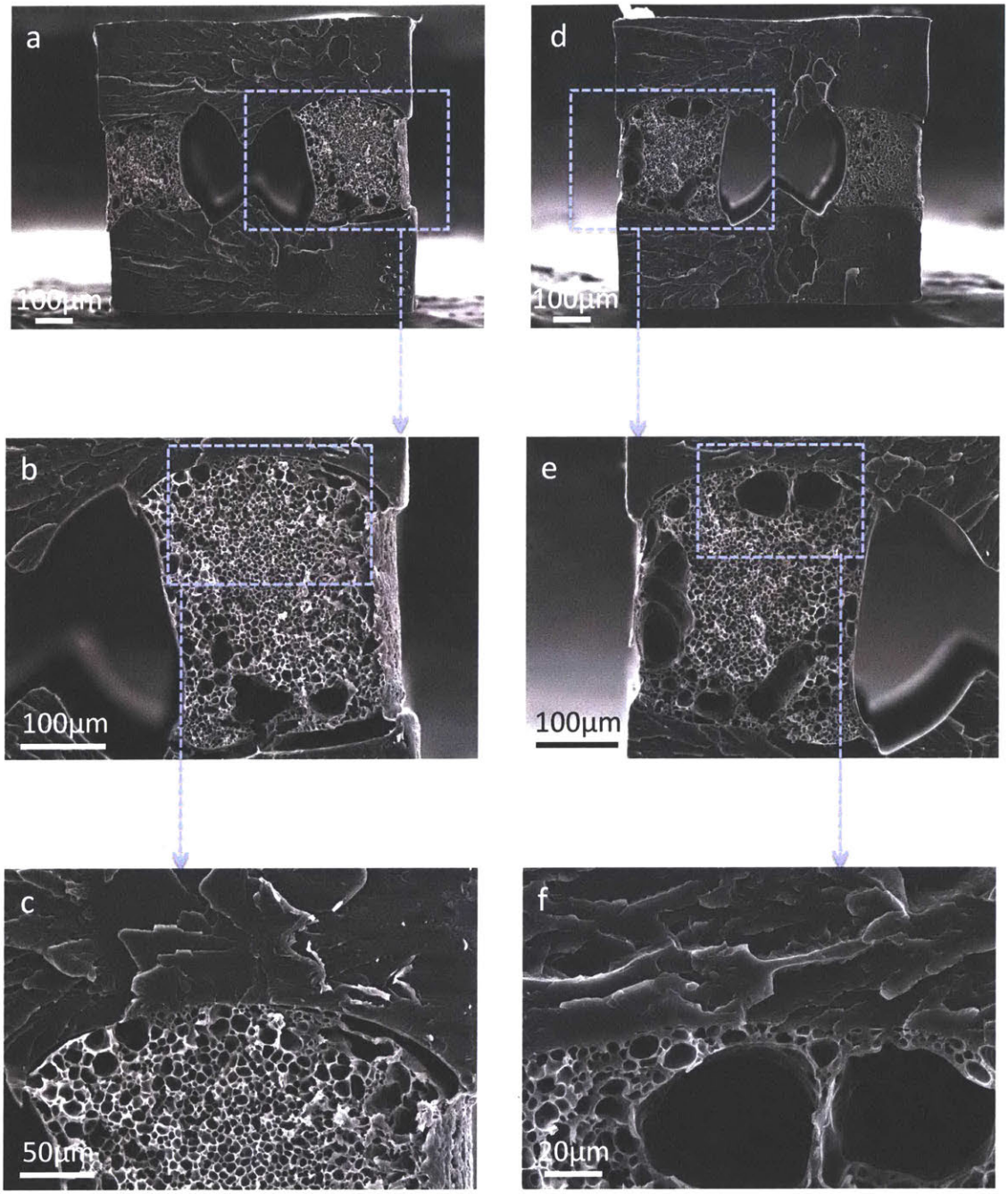

Figure 3-12: SEM micrographs of scaffold fiber.

core. This is an artefact of the core consolidation. The COC core used to define the hollow-core was consolidated from two U-shaped parts pressed together such as to define a hollow channel for fast etching. The consolidation of the this center part was not perfect and likely caused the part to buckle during the fiber draw, leading to this butterfly core. We also observed some gaps at the interface of PCL and LDPE in the cross sections, which we believe are results of the freeze-fracturing process. Longitudinal imaging of the fibers did not evidence any gaps in the structure.

3.4.2 Scaffold viability: neuron seeding and growth

We tested the scaffold viability *in vitro*, with neural cultures of dorsal root ganglia (DRG) harvested from neonatal rats - following a protocol close to that of Koppes et al.. All animal procedures were approved by the MIT Committee on Animal Care and conducted in accordance with the National Institutes of Health Guide for the Care and Use of Laboratory Animals.

Dorsal Root Ganglia harvesting

Dorsal root ganglia Dorsal root ganglia (DRG) are clusters of neurons located in the dorsal root of the spinal cord. They contain sensory neuron bodies projecting axons into limbs and towards organs [Kandel and Schwartz, 2013]. Owing to a large neuron body density as well as a tendency to project axons outwards, DRGs from chicks and neonatal rats have been used as an *in vitro* platform for tissue engineering in a number of studies [Yu and Shoichet, 2005; Yang et al., 2007].

DRG harvesting DRGs were isolated from the spinal cord of Sprague Dawley neonatal rats at day 1. In this procedure, we euthanized the neonates by decapitation and exposed their spinal cords from the back of the animals, in a so-called *posterior approach.* Careful removal of the spinal cord then exposed DRGs, apparent as small $<$1mm translucent beads located in small cavities in between spinal discs. We then collected the DRGs by cutting them from connective tissues and nerve roots, and

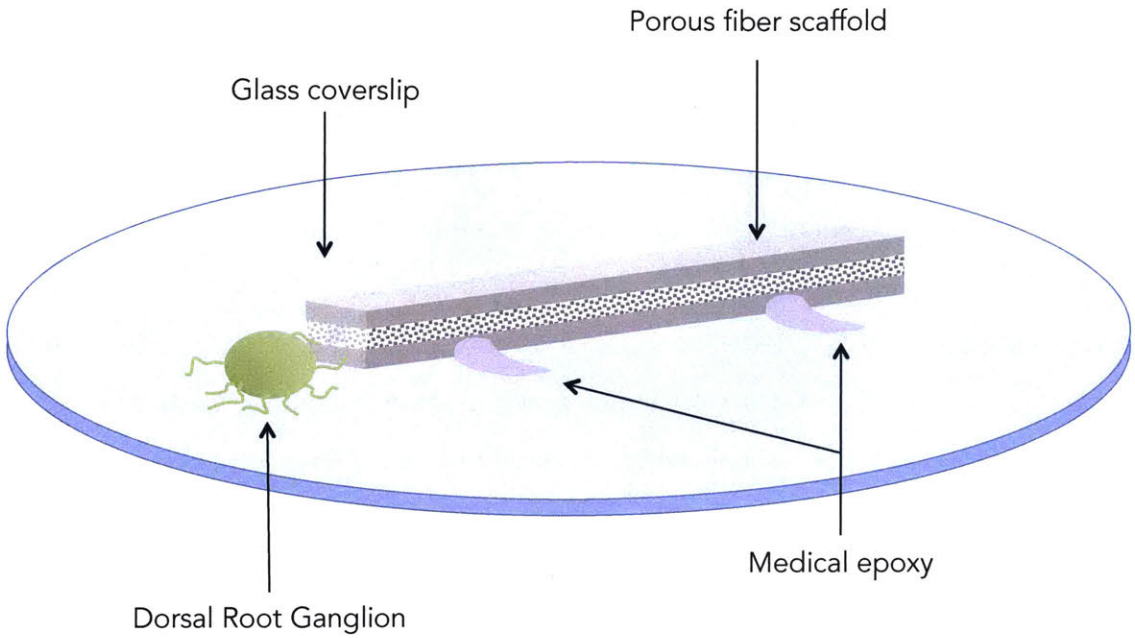

Figure 3-13: Illustration of the DRG seeding setup.

placed them in Hiberbate A solution at 4°C for up to 7 days. Roughly 10-15 DRGs were extracted per each animal.

Fiber seeding and neuron culture

Fiber samples preparation We cut 6cm fiber samples and etched out the COC in cyclohexane overnight. After rapid drying in air, we then cut these 6cm samples into 12mm samples. Samples were then dried under dynamic vacuum for 3-4 days. We then placed and fixed our dried samples with medical epoxy on 12-mm glass coverslips precleaned in 10% HCl solution and rinsed with 99% ethanol (EtOH). After curing of the epoxy, we treated the coverslip-sample assemblies with O_2-plasma to make the surface of the polymers hydrophilic. Following O_2-plasma treatment, coverslip assemblies were placed in individual wells in a 24-well tissue culture plate. Samples were then rinsed 3 times with EtOH and incubated 24hrs in EtOH, after which they were rinsed 3 times in sterile water and allowed to dry in air.

Prior to DRG seeding, the coverslip assemblies were sterilized under a UV lamp for

15min. In order to facilitate DRG cell adhesion, samples were subjected to a 3-hour incubation (37°C, 5% CO_2) in a 1:30 vol./vol. dilution of Matrigel in growth media (Neurobasal-A medium supplemented with B-27 Glutamax (Life Technologies), 1% penicilin-streptomycin (Lonza), 25ng/mL 2.5 nerve growth factor (Life Technologies)). Matrigel is tradermarked mixture of proteins produced by mouse sarcoma, a type of cancer, and sold by BD Biosciences. It is commonly used to generate a protein base-layer on synthetic scaffolds for tissue engineering [Hughes et al., 2010]. The exact composition of Matrigel is not precisely known, and varies strongly from batch to batch due to its animal origin. It mainly consists of structural proteins such as collagen or laminin, as well as glycosaminoglycans like heparan sulfate.

DRG seeding and culture After incubation in Matrigel dilution, the samples were rinsed in phosphate buffer solution (PBS) and individual DRGs were placed at one end of each fiber sample, adjacent to the tip - as illustrated on Figure 3-13. Each well was then filled with growth media and incubated for 14 days, with growth media replacement every 3 days. In order to get statistically relevant data, DRGs were randomly chosen from harvestest DRG originating from 8-10 animals.

3.4.3 Fiber scaffold immunocytochemistry

In order to visualize the different biological entities in our scaffolds resulting from the cell culture, we employed immunocytochemistry techniques. The general idea is to fix the cells and affix primary antibodies that will specifically target certain antigens present on different types of cell structures. Then a "stain" is used, which is a fluorescent secondary antibody which will selectively bind to the primary antibodies and enable imaging of specific cell structures using a confocal fluorescence microscope.

Cell fixation and staining

At the end of the 14-day incubation, fiber-DRG assemblies were fixed in a 4% solution of formaldehyde in PBS for 45min at room temperature. Formaldehyde is an organic

compound known to cross-link primary or secondary amino groups of proteins [Olivier and Jamur, 2010], thus "fixing" the cells.

Following fixation and rinsing in PBS, the cells were permeabilized with a 0.1% Triton X-100 solution for 25min. Triton X-100 is a nonionic surfactant with a polyethylene oxide hydrophilic group and a hydrocarbon hydrophobic group. At low concentrations, Triton X-100 molecules insert their hydrophobic group into the bilipid layer of the cell membranes thus disrupting the cell membrane and locally opening small gaps or holes where water and solute can diffuse [Olivier and Jamur, 2010]. At higher concentrations the molecules form micelles with the lipid molecules of the membranes thus completely destoying the membrane integrity and lysing the cells. Here we used low concentrations to simply permeabilize the membrane and be able to deliver antibodies into the cytosol.

Once the cells were pearmabilized, the samples were blocked overnight using 2.5% vol. goat serum in PBS solution at 4°C. Goat serum is a mixture of antibodies and proteins used as a blocking agent in immunocytochemistry [Olivier and Jamur, 2010]. The principle of blocking is to create a "blank slate" on the scaffold material by adsorbing proteins from the serum on the materials surface as well as on the cells. These adsorbed proteins prevent primary and secondary antibodies used in the following steps to nonspecifically bind. Without this step, the primary antibodies used later would nonspecifically bind to the scaffold material as well as many cell sites, and induce a large noise in the fluorescence signal.

At this point we incubated the samples for one hour at room temperature with 1:500 vol. rabbit anti-neurofilament 200 and 1:500 vol. mouse anti S-100 primary antibodies in goat serum, and rinsed three times in PBS. The anti-neurofilament antibody binds specifically to antigens present on neurites, while the anti-S-100 antibody binds to antigens present on the membranes of Schwann cells. Finally, we incubated the samples 1 hour at room temperature with 1:1000 goat anti-rabbit Alexa Fluor®633 IgG (A21070, Life Technologies), 1:1000 goat anti-mouse Alexa Fluor®568 IgG (A11004, Life Technologies). The two secondary antibodies specifically bind to the primary antibodies used before and allow fluorescence imaging of

the labelled structures. After rinsing in PBS, the samples are lastly incubated at room temperature for 15min with 1:1000 4'-6-diamidino-2-phenylindol (DAPI, Life Technologies), which labels all cell nuclei.

Confocal imaging

The stained samples were imaged using an Olympus FV1000 laser scanning confocal microscrope with a 10× dry objective (cf. Figure 3-14). Because of the relatively high absorbance of LDPE, the collected fluorescence signal was quite low. In particular, we were only able to collect the fluorescence signal from the DAPI channel - therefore Schwann cells and neurofilaments were not visibile in the fiber.

Despite this, we were able to observe the presence of cells in our fiber scaffolds thus indicating an outgrowth of the DRG into the scaffold. We measured the distance between the fiber tip and the furthest visible cell nucleus as a metric to quantify outgrowth. Extensions between 6 and 8.3mm were measured over 12 samples. As a comparison, previous studies showed a maximum neurite extension in dense PEI 200μm-square core fibers to be 4mm, with an average around 2.8mm Koppes et al..

3.5 Discussion and next steps

In this chapter we have laid the ground for the fabrication of porous nerve guidance scaffolds through thermal drawing. We designed an initial structure, developped the materials processing pathway, and solved the main materials-related challenge which was adhesion between disparate components in the fiber. We finally demonstrated the biological viability of our scaffold material by performing *in vitro* neural culture. The initial results show promising neurite extension beyond the maximum achieved with comparable fiber structures made of dense PEI [Koppes et al., 2016].

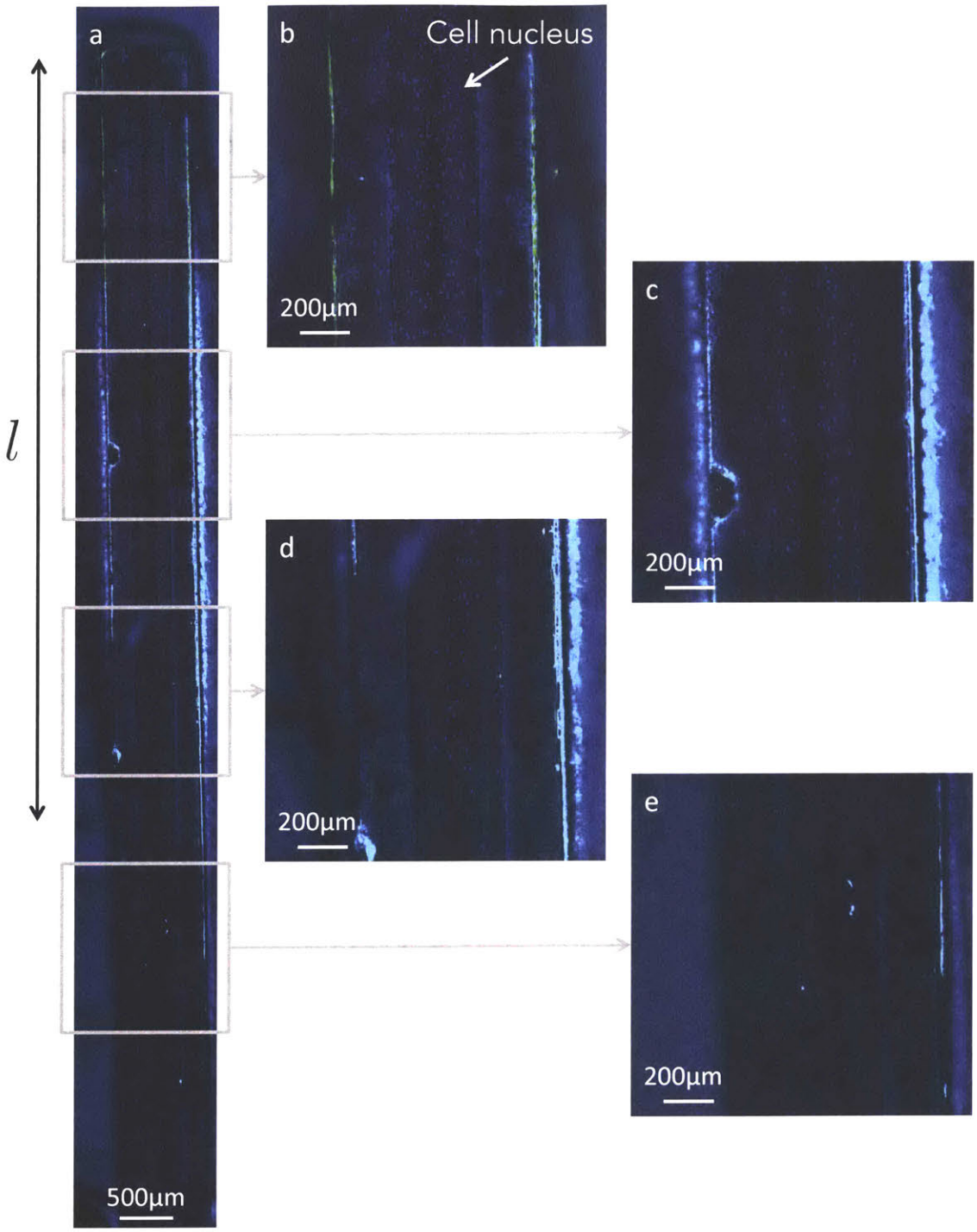

Figure 3-14: Confocal micrographs of scaffold fiber. (**a**) Global view of 12mm-sample. DRG was seeded near top tip. (**b-e**) Close-up views of locations along the scaffold fiber. Blue dots are DAPI-stained cell nuclei. Density of nuclei decreases away from DRG. Position of last visible cell nucleus marked as extension length l.

With this new fabrication platform, we can aim to complexify the structure and build in multiple cues and functionalities within the scaffold device. For instance, future studies can involve:

- Addition of electrodes into the structure, and study of effect of electrical stimulation on neurite outgrowth;
- Addition of electrodes into the structure, and study possible regrowth monitoring;
- Incorporation of topography in the fiber core, and study of the effects on neurite growth and alignment;
- Exogenous optical stimulation through fiber walls, and study on the effects on neurite growth in optogenetically modified neuron populations;
- *In vivo* assessment of scaffold in animal model

Chapter 4

Fibers with internal porous domains: Lithium-ion fiber battery

4.1 Motivations for a lithium-ion fiber battery

The domain of flexible electronics has been attracting considerable research and public interest over the past few years. Flexible electronics potentially offers a scope of applications much larger than that enabled by traditional wafer-based electronics. Devices such as flexible organic light-emitting diodes displays [Gustafsson et al., 1992; Choi et al., 2008], flexible solar cells [Yoon et al., 2008; Fan et al., 2009], or flexible sweat sensors [Gao et al., 2016] are being developed by various groups around the world, and slowly transitioning to market. The domain of wearables and smart fabrics stands out as a main field of application for these new technologies. The ability to develop electronic devices that seemlessly integrate in our ordinary clothes is of considerable interest - putting a special spotlight on multifunctional fibers.

Among all flexible electronic devices, flexible power sources occupy a crucial position. Indeed, flexible power sources are a key element to achieve fully flexible electronic systems. So far, lithium-ion batteries [Nishide and Oyaizu, 2008; Hu et al., 2010; Xu et al., 2013] as well as supercapacitors [Meng et al., 2010; Wu et al., 2010] have been considered as flexible power souces. However owing to higher energy density and good cycle life [Armand and Tarascon, 2008], lithium-ion batteries are the

preferred candidates for many applications. Typical fabrication methods for such flexible lithium-ion batteries include pouch-cell fabrication, microbattery arrays on flexible substrates, electrodeposition on fabrics, and lithography in serpentine structures [Liu et al., 2016]. However these methods are limited in terms of device sizes and scalability [Liu et al., 2016]. One of the key research objectives in the realm of flexible power sources - and more generally flexible electronics - is thus to achieve large area and low-cost production of conformal flexible systems.

In this chapter, we propose and present a fabrication scheme based on the thermal drawing process leading to flexible lithium-ion fiber battery devices. Motivations for this work are three-fold:

- First, fibers with appropriate mechanical properties can be extremely easily integrated into flexible objects of any shape and size through the millenial technique of weaving. Thus, a lithium-ion fiber battery could be the building block to large-area conformal flexible power sources.

- Second, fibers are ubiquitous. Transforming traditional fibers into potential energy storage devices could have a significant impact on the fields of advanced fabrics and wearables, but also in composite materials design. A back of the enveloppe calculation shows that a pair of jeans could withhold enough energy to charge an iPhone, assuming it's made of fiber batteries with an gravimetric capacity as low as one tenth of a traditional lithium-ion battery.

- Last, the thermal drawing process is an intrinsically scalable fabrication method, which is not the case of current Li-ion flexible batteries fabrication methods, and in principle could lead to hundred to thousands of meter of fiber from a single 30cm long preform.

In order to propose a suitable architecture and materials processing pathway one needs to grasp the mechanisms at play in lithium-ion batteries, in addition to the repertoire of established materials and processing methods. Thus we will start by giving a quick review of the fundamentals of lithium-ion batteries.

4.2 Background on lithium-ion batteries

4.2.1 Working mechanism

There are three components to any battery: the anode, the cathode, and the electrolyte. The anode and cathode are respectively the negative and positive electrodes of the battery. The electrolyte is an ionic conductor enabling lithium ions to travel back and forth between the anode and cathode; but also an electronic insulator to prevent short-circuits. During discharge, a spontaneous oxidation reaction occurs at the anode liberating lithium ions and electrons. The lithium ions migrate through the electrolyte towards the cathode, driven by a chemical potential difference - while electrons travel through the external circuit where they perform useful work. Lithium ions and electrons react at the cathode in an reduction reaction. During charge, the reverse reaction occurs provided an external voltage source is connected to the battery to supply the energy.

More specifically the working mechanism for most Li-ion rechargeable batteries is often reffered to as "the rocking chair" mechanism, or intercalation/deintercalation mechanism [Daniel and Besenhard, 2011]. Upon discharge, for instance, lithium ions flow through the electrolyte from the anode to the cathode where they intercalate directly into the crystal structure of the cathode material (cf. Figure 4-1). The open circuit voltage of the cell is dictated by the lithium chemical potential difference, which drives the reaction:

$$V_{\mathrm{OCV}} = -\frac{\mu_{\mathrm{Li}}^{C} - \mu_{\mathrm{Li}}^{A}}{zF} \tag{4.1}$$

where μ_{Li}^{C} and μ_{Li}^{A} are the chemical potential for lithium at the cathode and anode respectively, z is the number of charges transferred in the redox reaction, and $F = 96485\mathrm{C.mol}^{-1}$ is the Faraday constant.

4.2.2 Anode and cathode materials

Good electrode materials should exhibit high gravimetric capacities to maximize the energy storage, high diffusivity of lithium ions to ensure rapid charging, as well as

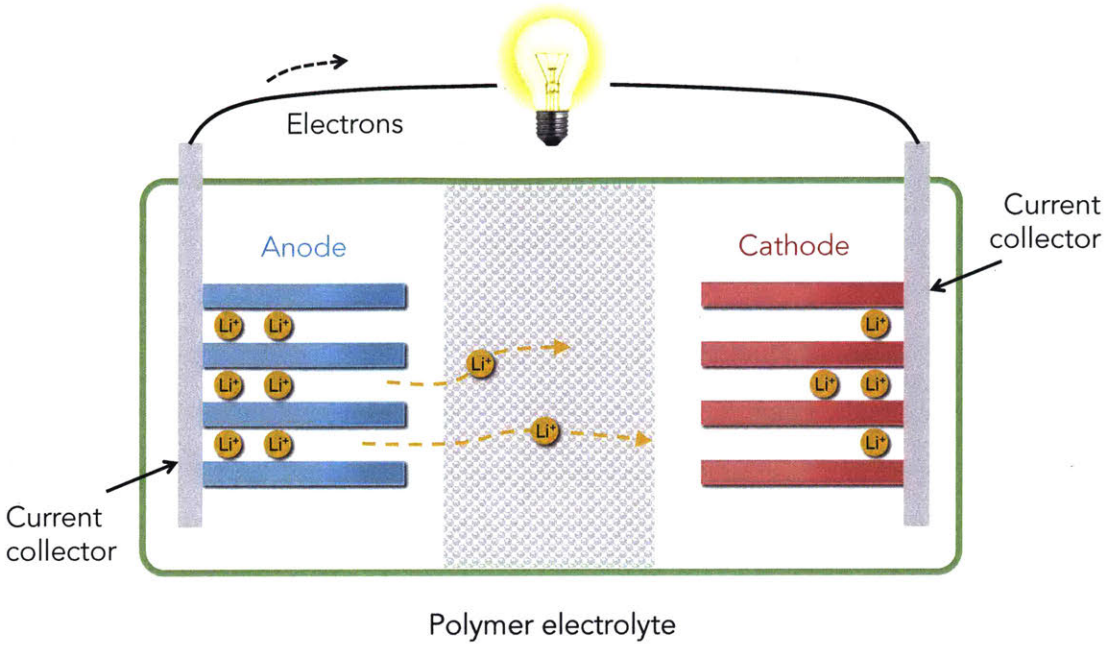

Figure 4-1: Schematic representation of a Li-ion polymer battery under discharge.

small volume changes between lithiated and unlithiated states to limit strains and possible mechanical failure. For a high battery operating voltage and therefore a higher energy density, the difference in lithium chemical potentials between cathode and anode should be as large as possible (owing to Equation 4.1) - within the electrochemical stability window of the electrolyte. This leads to privilege cathode materials with high (negative) lithium intercalation potentials, and anode materials with low (negative) lithium intercalation potential.

Cathode materials

Intercalation cathode compounds generally lie in three categories of crystal structures: layered oxides, spinels, and olivines. The most common and widely used cathode material is lithium cobalt oxide (LCO), a layered compound with the formula $LiCoO_2$ first introduced by Mizushima et al.. It has a theoretical specific capacity of 274 $mAh.g^{-1}$, a relatively high discharge voltage of 3.8 V vs. Li/Li^+, as well as good cycling performances [Nitta et al., 2015]. However it is quite expensive due to the high cost of cobalt, and prone to exothermic runaway reactions that can cause battery

explosions. Spinel structures such as $LiMn_2O_4$ show benefits such as lower cost, higher voltage, and good rate performances - while not performing as well in long-term cycling [Nitta et al., 2015]. More recently olivine structures of the form $LiMPO_4$ (where M=Fe, Co, Mn) have been investigated. Lithium iron phosphate $LiFePO_4$ (LFP) has emerged as a promising cathode material, with relative low cost, good specific capacity, and good rate performance as nanoparticles. Still, LFP has a lower discharge voltage of around 3.4 vs. Li/Li^+ thus limiting the energy density of LFP-based full cells. All three of these materials are well established and are being used in commercialized cells.

Recently a new type of cathode materials was introduced, known as conversion cathodes. Here, lithium ions react directly with the cathode material without intercalating. Most work in this area has focused on metal fluorides, and sulfur cathodes, as well as Li-air [Nitta et al., 2015]. Despite promises of much higher specific capacities (*e.g.*, 1675 $mAh.g^{-1}$ for sulfur), this materials system is less mature and we have chosen to not consider these in a first step.

Anode materials

The most common anode material is graphite. Upon charging, lithium ions intercalate in between the graphene layers of the graphitic structure to eventually form the structure LiC_6 with a small volume change ($\approx$10%) and high theoretical capacity of 372 $mAh.g^{-1}$ [Daniel and Besenhard, 2011]. Still, it suffers from a relatively low volumetric capacity compared to intercalation cathode materials, in addition to relatively high capacity losses in the first cycles due to reactions with electrolyte components. Lithium titanium oxide $Li_4Ti_5O_{12}$ (LTO) is an alternative candidate, also commercially successful. It displays higher volumetric capacity than graphite (600 $mAh.cm^{-3}$ theoretically), high cycle life and high rate performance associated with a "zero-strain" intercalation mechanism [Ohzuku et al., 1995]. However its high delithiation voltage around 1.55 V limits the energy density of LTO-based cells.

On top of these materials, conversion anodes also exist. They mechanism here is direct alloying of the anode material with lithium. Promising candidates to date

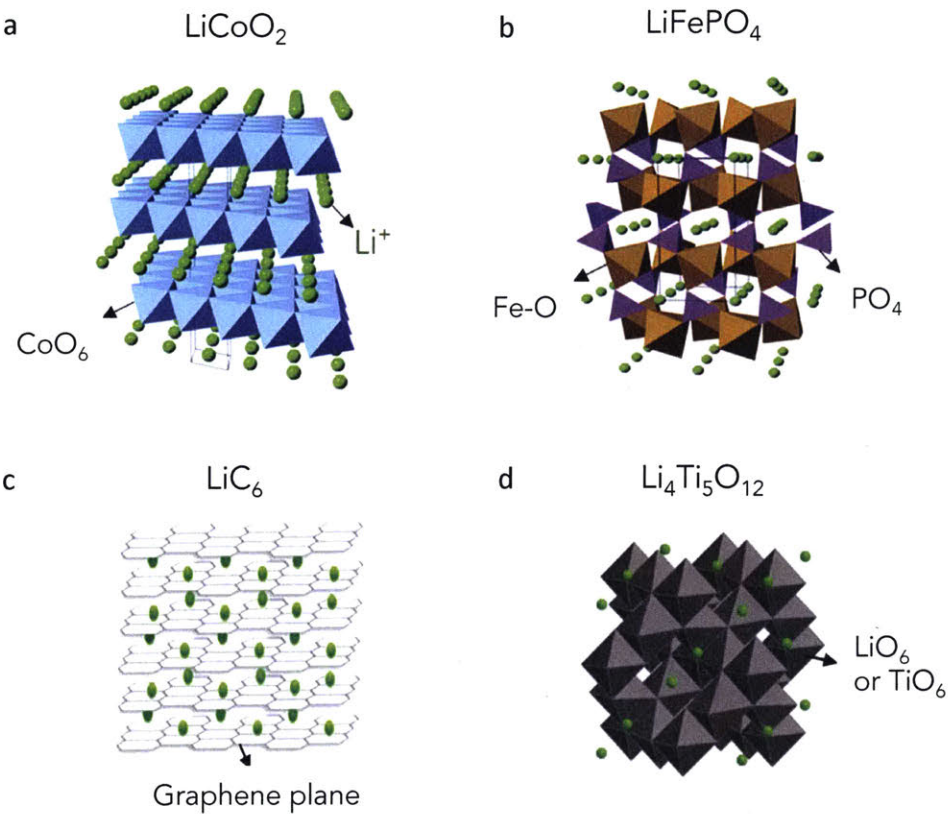

Figure 4-2: From [Nitta et al., 2015]: Crystal structures of conventional cathode and anode intercalation compounds. Green spheres represent lithium ions. (**a**) Lithium cobalt oxide, cathode, layered structure. (**b**) Lithium iron phosphate, cathode, spinel structure. (**c**) Lithiated graphite, anode, layered structure. (**d**) Lithium titanate, anode, spinel structure.

include silicon, germanium, or tin. Those materials share extremely high volumetric capacities (typically >1000 $mAh.g^{-1}$), but also extremely high volume changes upon lithiation causing rapid mechanical failure and short lifetimes [Nitta et al., 2015].

Conventional electrode processing

Anode and cathode intercalation coumponds are not used as pure monolithic materials in practice. They are generally introduced into a polymer composite electrode, by mixing the active material particles with a suitable polymeric binder and adding carbon black for electrical conduction. The choice of binder is dictated by its electrochemical stability and also its affinity to the particles [Daniel and Besenhard, 2011]. Poly(vinylidene fluoride) (PVdF) is a common choice as a polymeric binder. The role of the added carbon black is to ensure a sufficient electrical conductivity. Indeed, it is important that the electrodes have a high enough conductivity such that the electrons generated at the anode reaction sites during discharge, for instance, travel through the electrode up to the current collector where they are to be carried away into the external circuit. Electrodes are processed so as to maximize the amount of active material without sacrificing the cohesivity of the final structure nor the electrical conductivity. Typical electrode contents in practical applications show ratios close to 90% active material, $\approx$ 5% carbon black, and 5% PVdF binder in weigth [Daniel and Besenhard, 2011].

Both anode and cathode are always in contact with a current collector whose role is to ensure conduction of the electrons from the electrode to the external circuit. Generally, copper and aluminum are used as anode and cathode current collectors - but quite generally any metal with a low reactivity towards the electrode is a good choice for a current collector.

4.2.3 Electrolyte materials

The properties of an ideal electrolyte material are numerous, but importantly it should display a high ionic conductivity (order of $mS.cm^{-1}$ or higher), wide electrochemical

stability window, chemical compatibility with other battery components, on top of safety considerations [Julien et al., 2015]. No ideal electrolyte exists to date, but the field has attracted a huge research effort in namely three categories of materials: liquid nonaqueous solutions, polymer-based, and solid electrolytes.

Liquid nonaqueous electrolytes

In the first case, a lithium salt is dissolved into a nonaqueous solvent. This type of electrolyte requires the use of an insulating membrane in between the electrodes called a separator, preventing direct electrode contact which would cause the battery to short. Many lithium salts have been studied, but the most common are lithium hexafluorophosphate $LiPF_6$, lithium perchlorate $LiClO_4$, lithium tetrafluoroborate $LiBF_4$, or bis(trifluoromethane)sulfo-nimide lithium salt (LiTFSI). Organic solvents from the alkyl carbonate family are typically used such as ethylene carbonate (EC), dimethyl carbonate (DMC) or propylene carbonate (PC). Commonly, binary or ternary solvent mixtures are employed so as to obtain a wider phase stability window as well as well as wider electrochemical window [Xu, 2004]. Liquid nonaqueous electrolytes exhibit relatively high ionic conductivity, on the order of 10 $mS.cm^{-1}$ [Daniel and Besenhard, 2011]. However because of safety issues due to solvent leakage, high vapor pressure and flammability [Julien et al., 2015], liquid electrolytes are gradually being replaced by other systems.

Gel-polymer electrolytes and polyelectrolytes

Polymer-based electrolytes can be of different types. On the one hand, gel-polymer electrolytes are microporous polymeric structures filled with liquid electrolyte. The term "gel" comes from the swelling of the polymer phase by the solvent [Zhang et al., 2004]. Several host polymers have been investigated such as poly(acrylonitrile), poly(methyl methacrylate) or poly(vinylidene fluoride) [Manuel Stephan, 2006]. Performances are measured based on ionic conductivity, electrochemical stability towards the electrodes, and cycling behavior. Despite a somewhat lower ionic conductivity in general (on the order of 1-5 $mS.cm^{-1}$), gel-polymer electrolytes display many advan-

tages over their liquid counter parts such as increased safety due to lower leakage risk and effectively low solvent vapor pressure [Daniel and Besenhard, 2011].

Recently, systems in which lithium salts are dissolved directly into a polymer network have received a growing interest. Such systems are known as polyelectrolytes or solid polymer electrolytes. They are particularly compelling due to the absence of liquid phase and thus of toxic solvent. Typically they revolve around a polyethylene oxide or polyethylene glycol polymer, although increasingly more complex systems are being developed. However such polyelectrolytes still display low conductivity on the order of 10^{-3} mS.cm^{-1} at 25°C, rendering them unsuitable for room temperature applications [Manuel Stephan, 2006; Daniel and Besenhard, 2011].

Solid electrolytes

Lastly, we mention solid electrolytes which are ionically conductive solid ceramic materials in which ion migration occurs by diffusion in a crystal lattice. Solid electrolytes are a relatively novel kind of electrolytes and are currently attracting a growing research interest [Fergus, 2010], but intrinsically seem not suited for thermal drawing.

4.3 Challenges towards a lithium-ion fiber battery

We aim to produce a fiber with a cathode, electrolyte, and anode enclosed within a cladding, using the preform-to-fiber thermal drawing process. Challenges in doing so immediately arise from the constraints imposed by the fabrication method, namely: high temperature processing (≈ 200°C), and flowability of the different components.

4.3.1 Materials stability and compatibility

First and foremost, the materials chosen need to be thermally stable at our relatively high temperature process. Namely, all active materials, salts, and polymers should have degradation temperatures higher than the processing temperature. In addition, any organic solvents introduced in the preform should have a higher boiling point

than the drawing temperature, as well as melting points below ambient temperature. This sets intrinsic limits on materials.

Lithium salt stability Lithium salts used in lithium-ion batteries have in general relatively low thermal stabilities. In Table 4.1 we present the peak degradation tempertures for various lithium salts as measured by thermogravimetric analysis under nitrogen gas. Some salts display a two-step degradation mechanism with a stability plateau in between the two steps. LiBOB, LiTFSI and $LiBF_4$ emerge as the most thermally stable salts, and could be compatible with the drawing process.

Salts	T_P^I (in °C)	T_P^{II} (in °C)
$LiPF_6$	80	220
$LiClO_4$	62	501
$LiBF_4$	238	-
LiTFSI	431	-
LiBOB	355	-

Table 4.1: Peak degradation temperature of stage I and stage II for the most common lithium salts used in lithium-ion battery electrolytes measured by thermogravimetric analysis.

In addition lithium salts are commonly extremely moisture and O_2-sensitive, and require handling in dry environments such as a gloveboxes under inert nitrogen or argon gas. Already this calls for special preform preparation and drawing conditions which we will go further into later.

Solvents melting and boiling points Solvent melting and boiling points have been reported in literature. A summary for most common solvents is presented in Table 4.2. In addition, it is quite common to resort to mixture of multiple solvents to tune the physical properties such as liquid temperature range or viscosity. Only ethylene carbonate, propylene carbonate, and γ-butyrolactone appear compatible with typical drawing temperatures around 200°C.

Solvent	T_M (in °C)	T_B (in °C)
Ethylene carbonate	36.5	238
Propylene carbonate	-54.5	242
Diethyl carbonate	-43	126.8
Dimethyl carbonate	4.6	90
Ethyl methyl carbonate	-53	109
γ-butyrolactone	-43.5	204

Table 4.2: Melting and boiling points of commonly used lithium-ion battery electrolyte solvent. Data from [Daniel and Besenhard, 2011].

Constraints on active materials Most of the common active materials for anode and cathode have generally high intrinsic thermal stabilities with decompositions initiating generally above 300°C [Martha et al., 2011]. However purely chemical or electrochemical compatibility issues may exist between a given pair of active material and either electrolyte salt or solvent. For instance, it has been widely reported that graphitic anode material is electrochemically incompatible with propylene carbonate-based electrolytes. At 1.1V versus Li/Li^+, propylene carbonate molecules intercalate in graphite and exfoliate the graphene layers [Daniel and Besenhard, 2011; Xu et al., 2002]. In addition, thermal stabilities of active materials mixed with electrolyte components can be lower than for the pure material [Martha et al., 2011], adding another layer of complexity on materials selection.

4.3.2 Drawability of a functional electrolyte

From the standpoint of our drawing process, it seems gel-polymer electrolytes are the most suited electrolyte architecture. Liquid electrolytes pose significant safety issues, and solid ionorganic electrolytes are typically based on ceramics that do not flow in the temperature range of the drawing process. Solid polymer electrolytes are a promising technology with potentially suitable rheological properties, but these typically do not perform well at room temperature due to intrinsically low ionic conductivities. We therefore focus on the gel-polymer electrolyte architecture. In the context of thermal drawing, this requires introducing a porous PVdF domain in the fiber core, filled with a liquid electrolyte to provide ionic conductivity of lithium ions.

4.3.3 Drawability of functional electrodes

Direct drawing of pure active materials electrodes is in practice not possible, as most of the conventional electrode materials do not have melting points in our processing temperature range. Graphite for example sublimes before melting at atmospheric pressure, and lithium cobalt oxide decomposes before it melts. It is worth mentioning that some conversion anode and cathodes do have melting points in the appropriate range, but due to issues mentioned with these new materials we did not consider them.

Conventional lithium-ion batteries rely on composite electrodes, which could in theory be drawable for an appropriate concentration of host polymer versus active material and carbon black. For example, composites of low-density polyethylene (LDPE) with carbon black in weight contents of up to 30% have been used in various thermally-drawn fiber devices [Egusa et al., 2010; Chocat et al., 2012]. However there is a direct trade-off between the electrode rheology and flowability and the amount of active material particles that we can incorporate. In practice, the flowability limits the active material and carbon black content drastically, and typical electrode compositions lead to non-flowable systems.

4.3.4 Structural integrity

Assuming all components of the battery are able to co-flow in a relatively low-viscosity state, the issue of structural integrity then arises. Depending on the components' viscosities and channel sizes, convective mixing could be possible during the drawing process itself, yielding mixed structures displaying no electrochemical activities.

4.4 In-fiber phase separation of battery components

4.4.1 Principle of gel-based components

To circumvent processing constraints on both electrolyte and electrodes, we propose an approach based on phase separation of polymer-solvents systems enabling both to

introduce porosity in the electrolyte system as well as reduce the viscosity during the draw of the electrodes at high partice loading.

For the gel-polymer electrolyte

The objective is to incorporate a porous PVdF domain in the core of the fiber, filled with a solution of a lithium-ion battery organic solvent and lithium salt providing ionic conductivity. This naturally reminds the structure developed in Section 2.4, consisting of a porous PVdF domain filled with propylene carbonate and PYR13TFSI, produced with our in-fiber phase separation method. We aim here to employ the same approach with a relevant choice of solvent and lithium salt.

For the electrodes

The challenge for the electrodes is the produce composites with high active material and carbon black content per polymer, while still having suitable rheological properties. The idea here is to reduce the viscosity at high loading by solvating the polymer in appropriate organic solvent such that the system behaves as a relatively low viscosity slurry at high temperature, but like a solid-like gel in the fiber as the polymer phase separates from the solvent and solidifies at low temperatures.

4.4.2 Materials selection and gel production

With the challenges on materials stability and compatibility in mind, we targetted a set of materials compatible with the drawing process that we used to produce gels.

Polymeric matrix We chose PVdF as our polymeric matrix for the electrolyte as well as binder material for the electrode. This choice was dictated by its good electrochemical stability in addition to our ability to process it and form porous domain through in-fiber phase separation.

Anode and cathode active materials We chose lithium titanate $Li_4Ti_5O_{12}$ and lithium iron phosphate $LiFePO_4$ as anode and cathode materials respectively. We

chose LTO over graphite for ease of identification through energy dispersive spectroscopy, and LFP over lithium cobalt oxide for its low cost and commercial availability in micron-sized particles.

Lithium salt We chose LiTFSI as a lithium salt, due to its high thermal stability, good solubility in various battery organic solvents.

Organic solvents We chose to use a 1:1 vol. mixture of ethylene carbonate and propylene carbonate as our solvent. This mixture enables to depress the melting point of pure EC in order to have a liquid phase at room temperature while still having the electrochemical advantages of using EC, namely good electrochemical compatibility with many active materials.

We process gels in a glovebox under argon. For the electrolyte, we mix 20% wt. PVdF in a 1m (mol.kg^{-1} of solvent) LiTFSI in EC/PC 1:1 vol. solution. For the electrodes, we mix to the desired ratios PVdF with carbon black and active materials with 1m (mol.kg^{-1} of solvent) LiTFSI in EC/PC 1:1 vol. solution. The slurries are homogenized at 200°C for a few hours under stirring. At high temperature, both electrolyte and electrodes slurries behave as viscous liquids - but phase separate when cast on a glass plate to form solid-like gels. Figure 4-3 shows a photograph of a cast gel, as well as zero-shear viscosity measurements over a range of temperature for a typical electrode slurry.

4.4.3 Drawability of gel-based components

To demonstrate the drawability of our gel-based electrodes, we fabricated a simple core-cladding preform as shown in Figure 4-4.a. We used COC as a cladding material because of its chemical resistance to the solvents EC and PC at high temperature. We produced electrode slurries with 1:12:4 wt. ratios of CB/Active material/PVdF binder, mixed in 60 parts electrolyte solution (1 mol.kg^{-1} of solvent LiTFSI in EC/PC 1:1 vol). After homogenization at 200°C, we introduced electrode slurries in the indi-

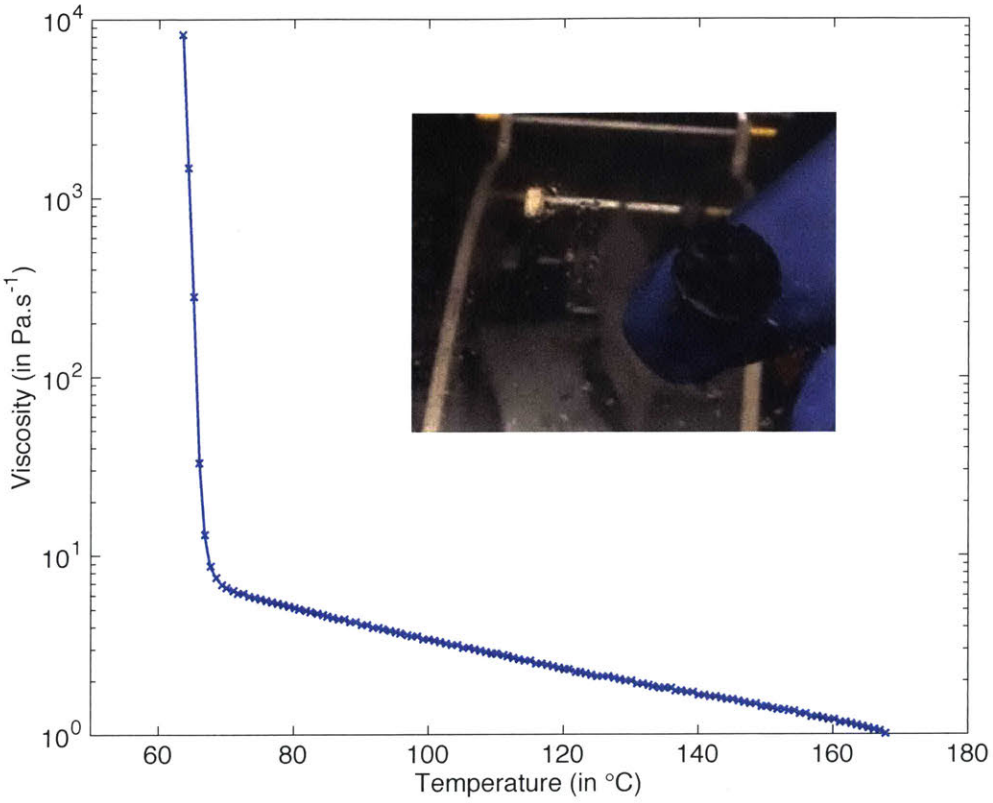

Figure 4-3: Gel component production and rheology. Zero-shear viscosity for a gel-cathode with composition 1:12:4:60 wt. ratios of CB/LFP/PVdF/electrolyte. Inset shows a photograph of gel at room temperature.

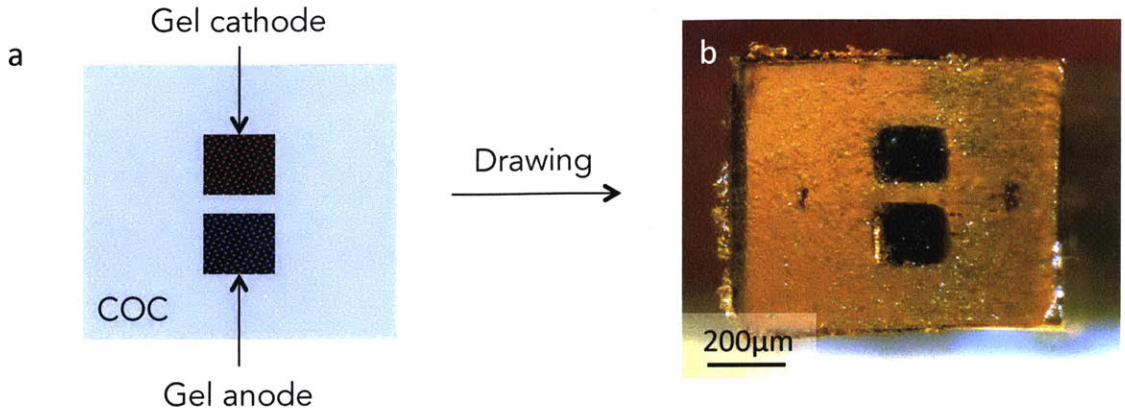

Figure 4-4: Gel-electrodes drawability test.(**a**) Schematic of preform structure. (**b**) Optical micrograph of final fiber.

vidual perform channels and carried out the thermal drawing around 200°C middle-zone temperature. The slurries coflowed with the COC and we obtained a fiber with cross-sections as depicted in Figure 4-4.b.

4.4.4 Electrochemical characterizations

Apart from drawability, we importantly needed to test whether our gel-based components were electrochemically functional even before drawing. We did this by assembling custom coin-cells comprising our gel-based materials and testing their electrochemical performances.

Coin-cell assembly

We assembled full cells of gel-based components. We used electrode slurries with the same composition as Section 4.4.3 : 1:12:4 wt. ratios of CB/Active material/PVdF binder, mixed in 60 parts electrolyte solution (1 mol.kg^{-1} of solvent LiTFSI in EC/PC 1:1 vol). The electrolyte was made from 20% wt. PVdF in electrolyte liquid solution. After homogenizing at 200°C in the glovebox, we cast the slurries on a clean glass plate with 1mm spacers. Then we punched out 9/16" electrodes and 3/4" discs electrolytes from the cast gels. The gel electrode discs were weighed to estimate the capacity based on particle loading and active materials gravimetric capacities. We assembled

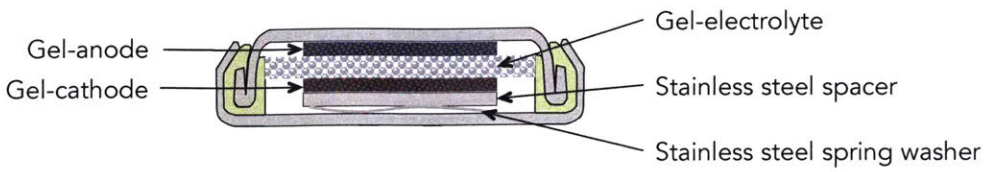

Figure 4-5: Schematic cross-section of the coin-cell assembly.

and crimped CR2032 coin-cells in the glovebox. A cross-sectional schematic of the coin-cell is shown in Figure 4-5.

Galvanostatic cycling

In galvanostatic cycling, cells are charged and discharged within a predefined voltage range at a constant current - positive current for charging, negative current for discharging. This allows to observe electrochemical activity in the presence of voltage plateaus in the cycling curves, as well as monitor the capacity and coulombic efficiency of the battery as a function of cycle number. The coulombic efficiency is the ratio of discharge capacity to charge capacity in a given cycle.

For our measurement, we chose a current corresponding to a rate of C/20 based on the electrode capacities estimated from weighing - this means that each charge and discharge steps takes about 20 hours. Full cell data is shown in Figure 4-6.(a-c). It shows good cycling ability over the first 25 cycles, with capacity rententions close to 100% and coulombic effiency above 95% after cycle 10. The shapes and values of retention and efficiencies are very close to those obtained by other groups with standard electrodes using the same active materials [Wang et al., 2013; Kurc and Jakóbczyk, 2016], albeit we are operating at a much lower rate thereby significantly limiting polarization effects.

Cyclic voltammetry

Cyclic voltammetry (CV) is a potentiodynamic electrochemical measurement, in which the voltage between two electrodes is ramped back a forth between two predefined values at a constant rate, while the current flowing in the system is measured [Bard and Faulkner, 2000]. In lithium-ion batteries, it is used to study the nature

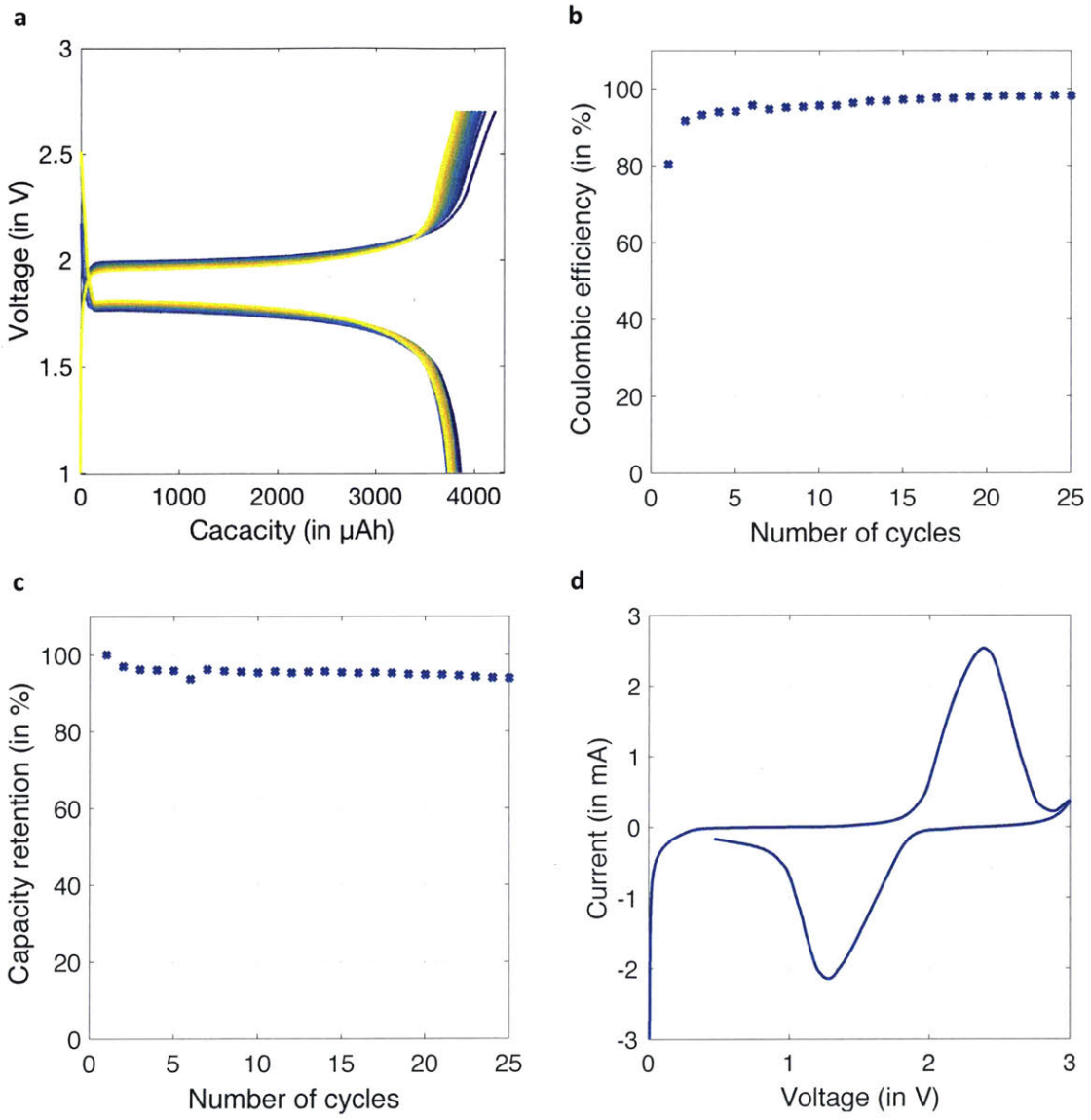

Figure 4-6: Typical full-cell data for gel-based system. (**a**) Galvanostatic cycling for first 25 cycles at a rate of C/20. (**b**) Coulombic efficiency for first 25 cycles. (**c**) Capacity retention for first 25 cycles. (**d**) Typical cyclic voltammogram at a rate of 100 μV.s^{-1}

of electrochemical processes and their reversibility. For an ideal lithium-ion battery with zero internal resistance, the cyclic voltammogram should be two bell-shaped curves of the same magnitude centered around the same voltage; one with positive current corresponding to the charging reaction and one with negative current corresponding to discharge. In practice though, internal resistance of the battery causes so-called overpotentials to develop and shift charging peak to higher voltages, and the discharging peak to lower voltages; while finite coulombic efficiencies reduce the magnitude of the discharging peak current.

We performed cyclic voltammetry measurements on the full cell at a rate of 100 $\mu V.s^{-1}$. The data presented in Figure 4-6.d confirms the electrochemical activity of our gels and the ability of lithium ions to undergo intercalation/deintercalation in the electrode active materials. The positive peak at 2.4 V corresponds to the charge reaction, with lithium intercalating into the LTO electrode with a positive current; and the reverse discharge reaction occuring at 1.27 V and negative current. The voltage hysteresis is associated to polarization effect resulting from the battery internal resistance. Again, the CV profile we obtained with the gel system is close in shape to conventional electrodes with the same materials [Wang et al., 2013].

4.5 Preform design, fabrication, and characterization

4.5.1 Issue of intermixing

We want to use the gel-based components to produce a lithium-ion fiber battery with a cross section similar as shown in Figure 4-7.a. However a major issue remains. Because of the low viscosity of the gel-based components at high temperature (cf. Figure 4-3.c), the structure is prone to intermixing during the drawing process if no special care is taken. Specifically if we assemble a preform structure by sandwiching a layer of gel-electrolyte in between two gel-electrodes in their low-temperature solid-like form, then heating of the structure in the draw tower will cause complete mixing

and loss of structure and result in a fiber preform with a cross-section schematized in Figure 4-7.b.

The strategy we employed here is to place a physical barrier between the components that would prevent mixing while still permitting ion conduction in the final fiber. In Figure 4-4 we have shown an example of a COC physical barrier maintaining structure; however COC is not ionically conductive and therefore does not enable electrochemical activity. Instead, our approach is to use a non-porous PVdF barrier at the interface between electrolyte and electrodes at the preform level, as represented in Figure 4-7.c. In the furnace, the high viscosity of the PVdF layer would permit to physically separate the components while being slowly solvated by the EC/PC solvents present in the electrolyte and electrodes. The challenge is to tune the kinetics of the solvation process such that the PVdF barrier remains viscous enough in the drawing process to prevent mixing, while being solvated enough or fully dissolved in the final fiber to grant ionic conduction through the interface Figure 4-7.d.

4.5.2 Preform design and assembly

We assemble a preform with the cross-section schematized in Figure 4-7.c. The center channel is lined with a non-porous PVdF film (Solef), 100μm in thickness. A carbon-loaded polyethylene (CPE) conductive electrode is placed in each electrode channel, with an Bi-In eutectic alloy wire playing of the role of current collector. The CPE layer is necessary to prevent to inflow of the dense metal wire into the electrode channel during the draw.

Once assembled and consolidated, the preform is taken into the glovebox where we prepare the electrolyte solution and both electrode slurries. Once homogenized, these are individually cast on a clean glass plate with spacers corresponding to the preform channel thickness, cut to width, and inserted into the appropriate preform channels by sliding. The top of the preform is sealed with a 100-μm film of COC epoxied to the preform using high-temperature chemically resistant epoxy.

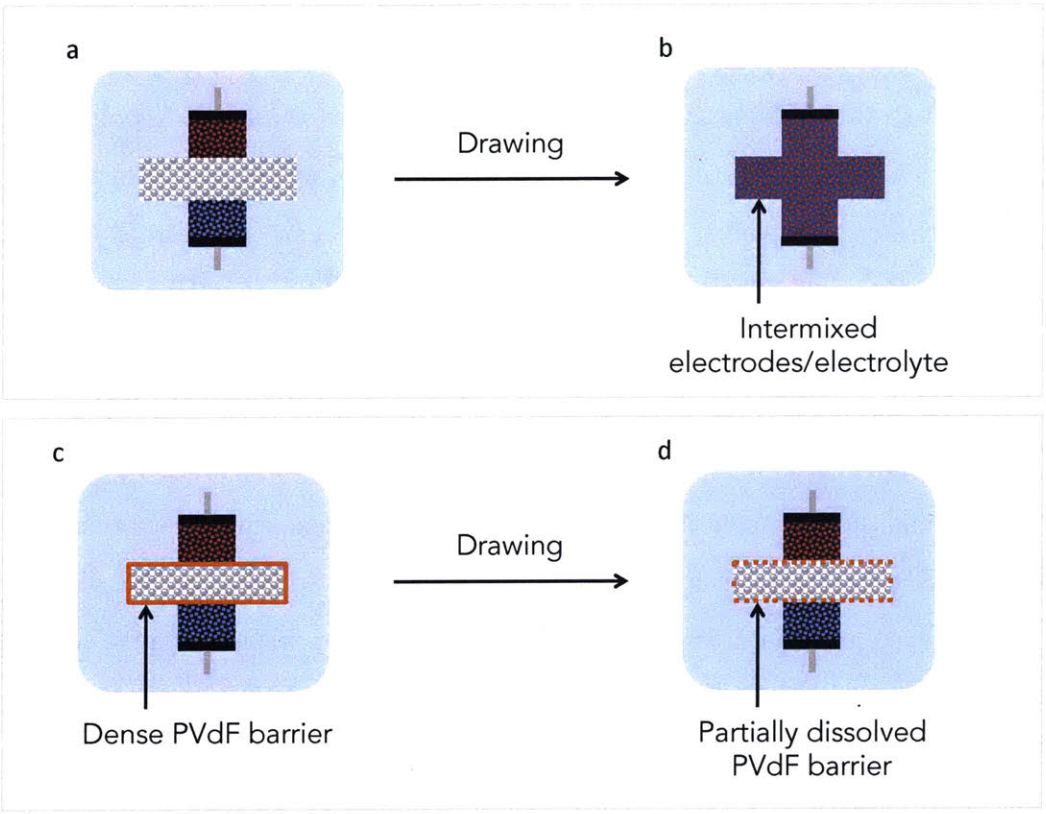

Figure 4-7: Intermixing issue. Top panel: (**a**) Preform prepared with no barrier between electrolyte and electrodes, resuling in (**b**) complete intermixing during the drawing process. Bottom panel: (**c**) Preform prepared with dense PVdF barrier at the electrode/electrolyte interface, resulting in (**d**) separated components with ionic conductivity at the interface.

4.5.3 Drawing under reduced moisture conditions

As mentioned previously, the lithium-ion battery chemistry is extremely sensitive to moisture and oxygen. Even though effort is taken to seal the preform in an argon glovebox, moisture or oxygen intake may still be important during the thermal drawing process - where the materials are heated to about 200°C for at least one hour in ambient atmosphere.

To reduce the risk of contamination during the drawing process, we designed and built a setup to perform the draw in a nitrogen-rich environment. A polycarbonate extension sleave is attached to the bottom of the furnace, while the top of the furnace is sealed with a rubber gasket. We flow high purity nitrogen gas from the top of the furnace at a rate of 20-30 $cm^3.s^{-1}$. The furnace is purged with nitrogen for 2 hours while being preheated to bait-off temperature. We then rapidly transfer the preform from the glovebox to the draw tower and undergo the drawing process. With this setup we are able to maintain a relative humidity level around 1% in the furnace and extensional sleeve, such that the fiber only experience ambient humidity levels when cold. The drawn fiber is not cut but spooled to avoid exposing the fiber cross-section to air. When the draw ends the fiber tip is sealed with wax, and the fiber is transferred as a whole into the glovebox for cutting and sample preparation.

4.5.4 Morphological characterization

We analyzed the fibers' morphology to assess the degree of electrode materials segregation.

Optical microscopy

Optical micrographs of the fibers are presented in Figure 4-8.a-d. Most sections display clearly segregated electrodes and electrolyte proving the ability of the PVdF barrier to physically separate the components during the draw (cf. Figure 4-8.a-b). The presence of intermixed regions such as seen in Figure 4-7.c-d can be a consequence of initial PVdF film non-unformity or local temperature non-uniformity. The

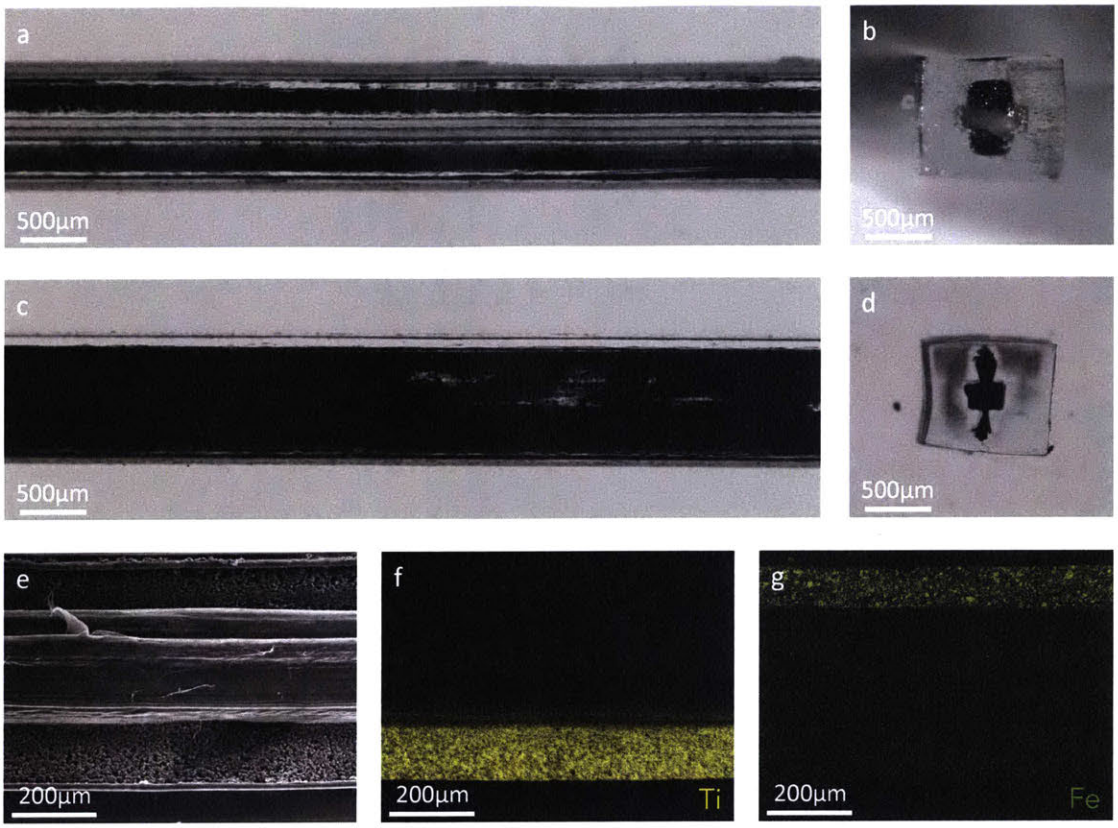

Figure 4-8: Structural analysis. Top panel: (**a**) longitudinal and (**b**) cross sectional optical micrographs of segregated electrodes region. Middle panel: (**c**) longitudinal and (**d**) cross sectional optical micrographs of intermixed electrodes region. Bottom panel: (**e**) SEM micrographs and (**f-g**) EDS elemental mapping for Ti (yellow) and Fe (green), marking respectively $Li_4Ti_5O_{12}$ anode and $LiFePO_4$ cathode.

timescale for PVdF solvation will scale as $t_d \sim a^2/D_0 e^{-\frac{E_a}{kT}}$, therefore local variations in film thickness or temperature can both have a strong impact on the time to total dissolution and therefore on the local disruption of the barrier. We also noted that even in segregated regions, the electrode thicknesses did not appear necessarily constant, hinting at additional tuning of drawing parameters for more controlled structures.

SEM and EDS analysis

To confirm segregation at the microscale, we prepared samples for SEM analysis by dissolving the COC cladding in cyclohexane overnight, drying the obtained core and

observing the core region longitudinally. The cyclohexane does not affect the PVdF, however it does remove the organic solvents naturally present in the battery structure initially, and drying further distorts the structure. Therefore the SEM images are not an exact representation of the in-fiber structure, but do serve to analyze segragation and interfacial microstructure in greater details. EDS mapping enables to detect the presence of titatnium atoms (cf. Figure 4-8.f) and iron atoms (cf. Figure 4-8.g), thus marking respectively the $Li_4Ti_5O_{12}$ anode and $LiFePO_4$ cathode active materials and confirming the good segregation of active material particles and the barrier role of the PVdF layer in segregated regions.

4.5.5 Electrochemical characterizations

Fiber connection

The first step to testing the electrochemical performances of the fiber batteries is connection. Because of moisture sensitivity of the core battery structure, the fiber samples were cut in the glovebox. We only used fibers from cleanly segragated regions. After cutting, the tips of the samples are sealed in wax and the samples are removed from the glovebox for connection. The connection method is similar to that presented in Section 2.4.1; namely we expose the metal buses on each side under a microscope using a razor blade. Then we solder a metal wire onto the exposed metal, and apply 5-min epoxy around the connection for sealing and mechanical robustness.

Galvanostatic cycling

We performed galvanostatic cycling on various fiber samples. Results for two typical samples are shown in Figure 4-9. The cycling curves in Figure 4-9.a,c demonstrate electrochemical activity, with lithium intercalation/deintercalation plateaus around 2.2 and 1.6 V. However, compared to a conventional lithium-ion battery, there is a large voltage hysteresis between charge and discharge, indicating a large battery internal resistance causing high polarization. Second, the coulombic efficiency is extremely low - 65% for sample 1, only 44% for sample 2. Third, the overall discharge

capacity is very low, on the order of μAh per centimer of fiber. Lastly, the capacity retention is in general low, as evidence by Sample 2 on Figure 4-9.d - after 20 cycles the discharge capacity is only half of its value at the first cycle.

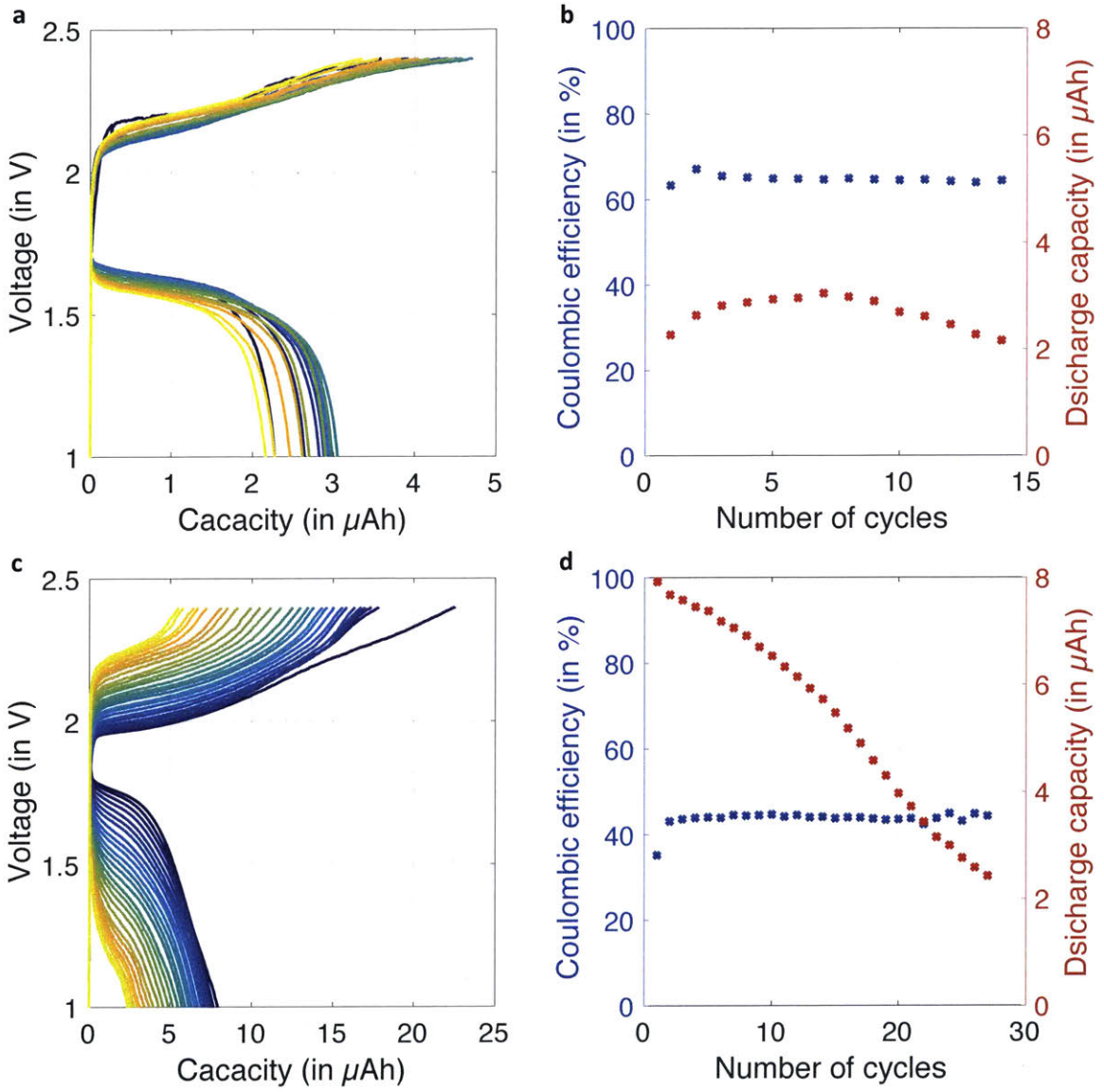

Figure 4-9: Galvanostatic cycling. Top panel: 9cm fiber sample, (**a**) charge/discharge voltage profiles abd (**b**) Coulombic efficiency and discharge capacity as a function of cycle number. Bottom panel: 6cm fiber sample, (**c**) charge/discharge voltage profiles abd (**d**) Coulombic efficiency and discharge capacity as a function of cycle number.

4.6 Discussion and next steps

In this chapter we demonstrated a fabrication approach to produce lithium-ion batteries in a fiber form factor, using the preform-to-fiber thermal drawing. The key concept is that of gel-components, which enables processing as relatively low-viscosity fluids during the drawing process but phase separate in a solid-like component at low temperatures in the fiber. We made the first samples displaying electrochemical activity and showing lithium intercalation/deintercalation behavior. However, many aspects remain to be improved. Future work should focus on:

- Optimize preform geometry and drawing conditions to produce high quality fiber structures, with segregated electrodes and small structural variability from sample to sample.
- Investigate gel-electrode composition to maximize active material content, as well as electrical conductivity in order to lower battery internal resitances.
- Improve fiber drawing and sample preparation to reduce moisture exposure and contamination.
- Analyze effects of deformations on battery performances.
- Integrate multiple fiber batteries to demonstrate concept of energy storage fabric.

Chapter 5

In-fiber Si-Ge microspheres with controlled morphologies

5.1 Motivations

Control over the structure of micro- and nanoparticles is often key to attaining the desired properties for a specific application [Oldenburg et al., 1998; Ow et al., 2005; Lee et al., 2011; McConnell et al., 2010], however the ability to do so is strongly limited by the synthesis method. For example non-spherically symmetric inorganic materials distribution are difficult to achieve from bottom-up approaches [Yu et al., 2005; Ye and Carroll, 2010]. In particular, there is a large effort in producing Si/Ge anisotropic particles with applications spanning solar cells, infrared photodetectors, and ultrafast radiofrequency circuitry [Mehringer et al., 2014; Cristobal et al., 2012; Xiang et al., 2006]. However scalable methods to produce Si-Ge anisotropic particles with precise morphological control have remained elusive thus far.

Recent breakthroughs from Kaufman et al. and Gumennik et al. have shown how fluid instabilities can be harnessed to break the axial invariance of thermally-drawn fibers and produce micro- and nanospheres of a core material encapsulated within the cladding - both in polymeric fibers [Kaufman et al., 2012] and in silica fibers [Gumennik et al., 2013]. These results stem from the ubiquitous phenomenon of capillary breakup, *i.e.* the spontaneous evolution of a liquid cylinder into a row of

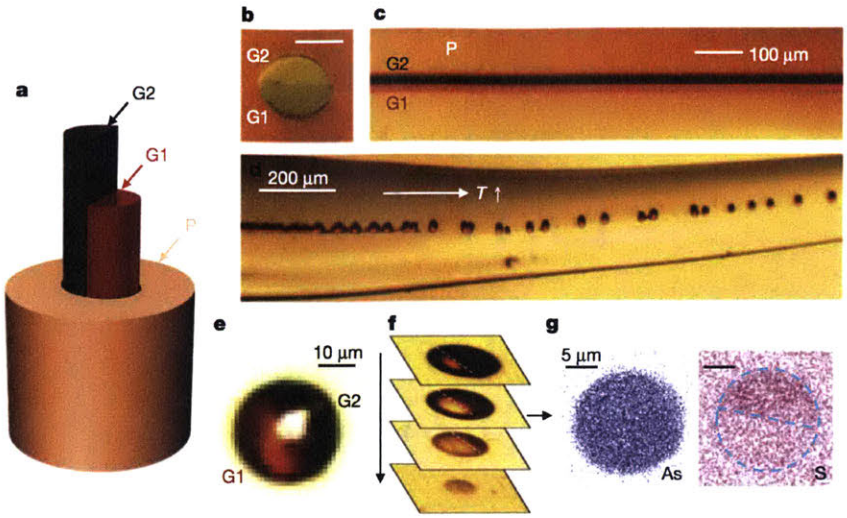

Figure 5-1: From [Kaufman et al., 2012]: demonstration of the fabrication of a Janus-particle from breakup of a Janus core fiber consisting of two glasses G1 and G2 with respectively high and low sulfur content.

spheres driven by reduction in surface energy [Rayleigh, 1892; Tomotika, 1935].

In particular Kaufman et al. showed they could form structured spheres of different materials, as shown in Figure 5-1. By assembling at the preform level a core with a broken symmetry consisting of mulitple materials, the authors were able to produce structured spherical particles. For example Figure 5-1 shows the fabrication of a Janus particle from a core consisting of two half-cylinders of different chalcogenide glasses.

However, the challenges in structuring spheres of silicon and germanium are unique, and the pathway to succeed is fundamentally different from the one for structured chalcogenides particles. In the latter case, the high viscosity of the chalcogenide glasses prevents the mixing of the materials at high temperature, and enables for instance two half cylinders to be drawn into a fiber without intermixing, and breakup into Janus particles. The situation is critically different for silicon and germanium: their low viscosity and high solubility causes the materials to mix in the liquid state thus destroying any kind of predefined structure. Even if a preform were prepared with two half-cylinders of silicon and germanium, the fiber core would consist of a homogeneous alloy. In this chapter we propose a method to produce Si-Ge Janus

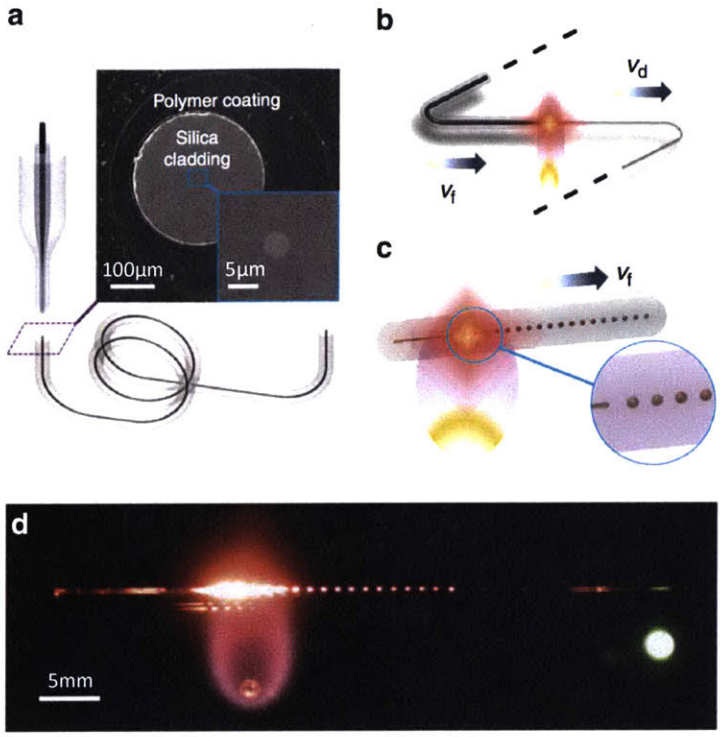

Figure 5-2: From [Gumennik et al., 2013]: General approach for the production of silicon and germanium spheres via the flame-induced breakup method.

particles by taking advantage of germanium segregation occurring in Si-Ge alloyed spheres solidifying in strong axial thermal gradients - a type "kinetic phase separation".

5.2 Production of Si-Ge Janus particles in a flame gradient

5.2.1 General approach to production of silicon and germanium spheres

Our general method follows the approach of Gumennik et al.. We start with the fabrication of a fibre consisting of a crystalline semiconductor core surrounded with a silica cladding, through the preform-to-fibre thermal drawing process [Ballato et al., 2008, 2009]. This fiber is fed through a flame which locally heats the core and the

cladding above their melting and softening temperatures respectively, and induces local capillary breakup of the semiconductor core into a liquid droplet surrounded by silica, as illustrated in Figure 5-2. Particles are produced one-by-one, in the manner of a dripping faucet.

5.2.2 Breakup of Si-Ge particles in a strong thermal gradient

As opposed to the isothermal breakup technique of Kaufman et al., the flame method imposes a strong axial thermal gradient on the particles. As the fibre exits the flame, it cools down. Because both silicon and germanium have melting points below the softening point of silica, the cladding hardens first and creates a smooth hermetic pressure vessel surrounding the molten semiconductor droplet in a process that resembles float glass fabrication. Then, the droplet subsequently solidifies in the temperature gradient imposed by the flame, and the solidification front (denoted by ξ in Figure 5-4.a) is expected to propagate from the colder side towards the hotter side.

In the case of a droplet comprised of a Si-Ge binary alloy, the lower solubility of germanium in the solid phase compared to the liquid phase would cause germanium to get extruded into the liquid, and would eventually lead to an axial distribution of the germanium content across the droplet - much like in a conventional Bridgman process [Schilz and Romanenko, 1995]. More specifically, Figure 5-3 shows an illustration of the anticipated solidification process. As a homogeneous $Si_{0.5}Ge_{0.5}$ droplet in step (1) is cooled in the flame thermal gradient, it starts solidifying from its colder side. The solid formed in (2) has a higher silicon content close to 80% as defined by the phase diagram of Si-Ge, and germanium is therefore rejected into the liquid, raising the germanium content of the liquid and lowering its melting point. The system "phase separates" both in terms of Si/Ge content and solid/liquid. As the temperature continues to decrease, the solidification front propagates along the thermal gradient and more solid is formed with a composition following the solidus line defined by the phase diagram. In parallel, the germanium content in the liquid keeps increasing owing to its lower solubility in the solid phase. Eventually the sphere solidifies entirely with an axial distribution of germanium content.

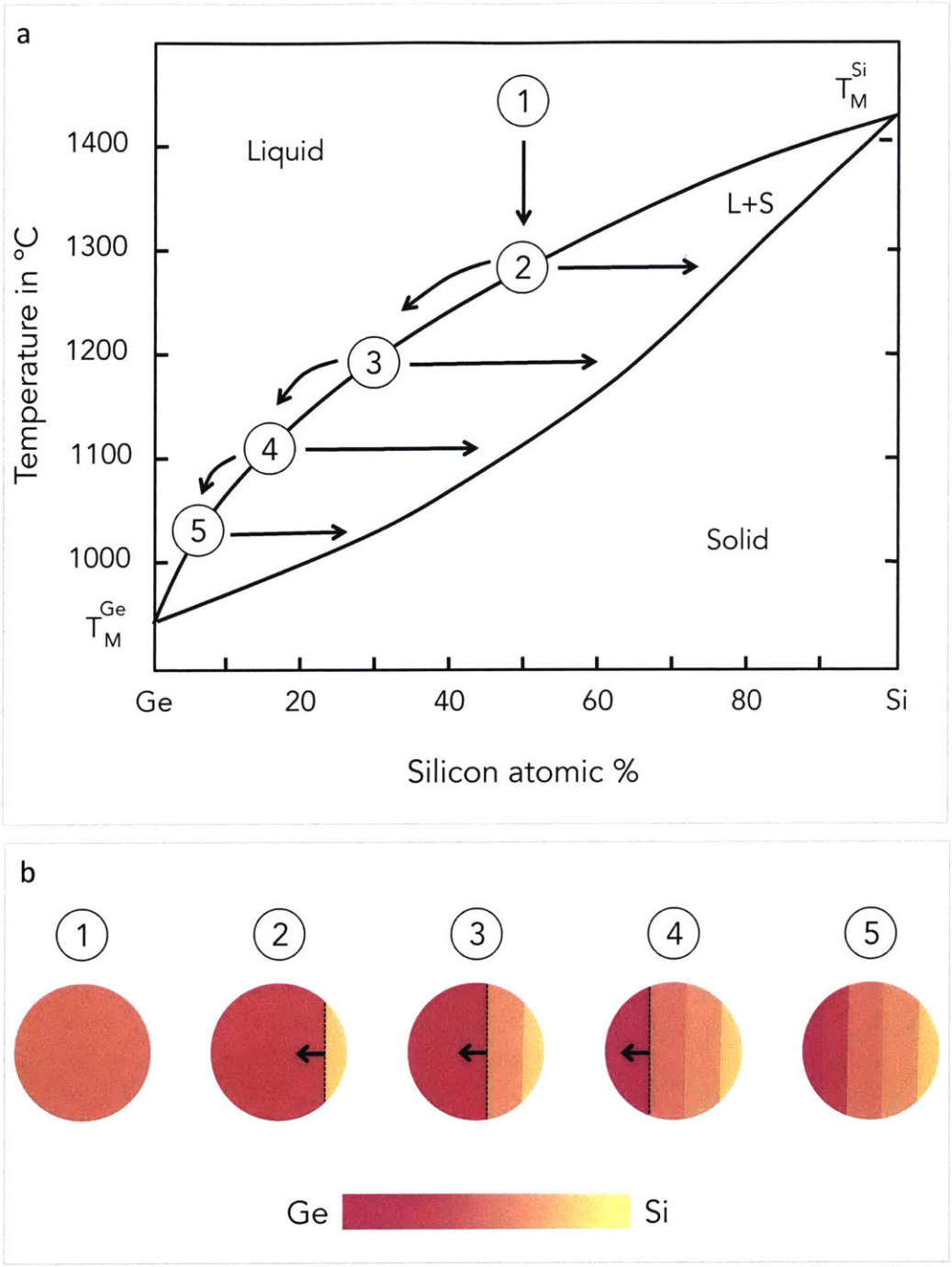

Figure 5-3: (**a**) Phase diagram of Si-Ge [Schilz and Romanenko, 1995] with anticipated solidification path. (**b**) Illustration of Si-Ge compositions in a sphere solidifying on a strong thermal gradient. The black dashed line is the solid-liquid interface, and the arrow denotes the propagation of the solidification fron.

5.2.3 Results

We have experimentally demonstrated a stable lateral solidification of Si-Ge droplets by fabricating an array of axially oriented Si-Ge Janus particles from a $Si_{0.5}Ge_{0.5}$ core fibre. Scanning Electron Microscopy (SEM) and Electron Dispersive Spectroscopy (EDS) mapping of the fabricated $Si_{0.5}Ge_{0.5}$ spheres suggest that the Si/Ge distribution has a distinct axial dependence, oriented along the fibre axis (Figure 5-4.b-d). The Si/Ge map in Figure 5-4.d clearly shows that the sphere is a Janus particle having a Si-rich lobe and a Ge-rich lobe. The quantitative analysis of EDS shows that the Si:germanium ratio in the Si-rich lobe is roughly 5:2 (Figure 5-4.f), similar yet not identical, to what is expected from the respective isothermal quasi-static segregation coefficient for $Si_{0.5}$-$Ge_{0.5}$ melt resulting from the Si-Ge phase diagram [Schilz and Romanenko, 1995] (Figure 5-4.e). The calculations leading to the theoretical silicon and germanium contents in the solid were performed by Etgar Levy, and will not be detailed in this thesis. We found however a good agreement between experimental and theoretical composition distributions (Figure 5-4.f). The small discrepancy in the Si-rich lobe can be explained by the fact that the initial solidification occurs through fast dendritic growth as opposed to slow stable solidification which our model assumes. This initial transient regime known as recalescence [Nagashio et al., 2002] proceeds until the latent heat released causes the droplet to heat up back to the melting point, allowing the solidification to then proceed in a stable planar fashion.

The stability of the solidification front propagation appears to be a requirement for the axial germanium distribution. If cooling conditions are such that the solidification front in the droplet is indeed unstable throughout the sphere volume, the resulting spheres would likely display cellular or dendritic microstructures with no particular orientation [Balluffi et al., 2005]. The flame setup does not allow sufficient control over the cooling kinetics and thermal gradient direction, and we have therefore devised a technique of laser-induced recrystallization allowing us to not only study more precisely the effect of the cooling conditions, but also control the axis of the Janus particle within the fibre.

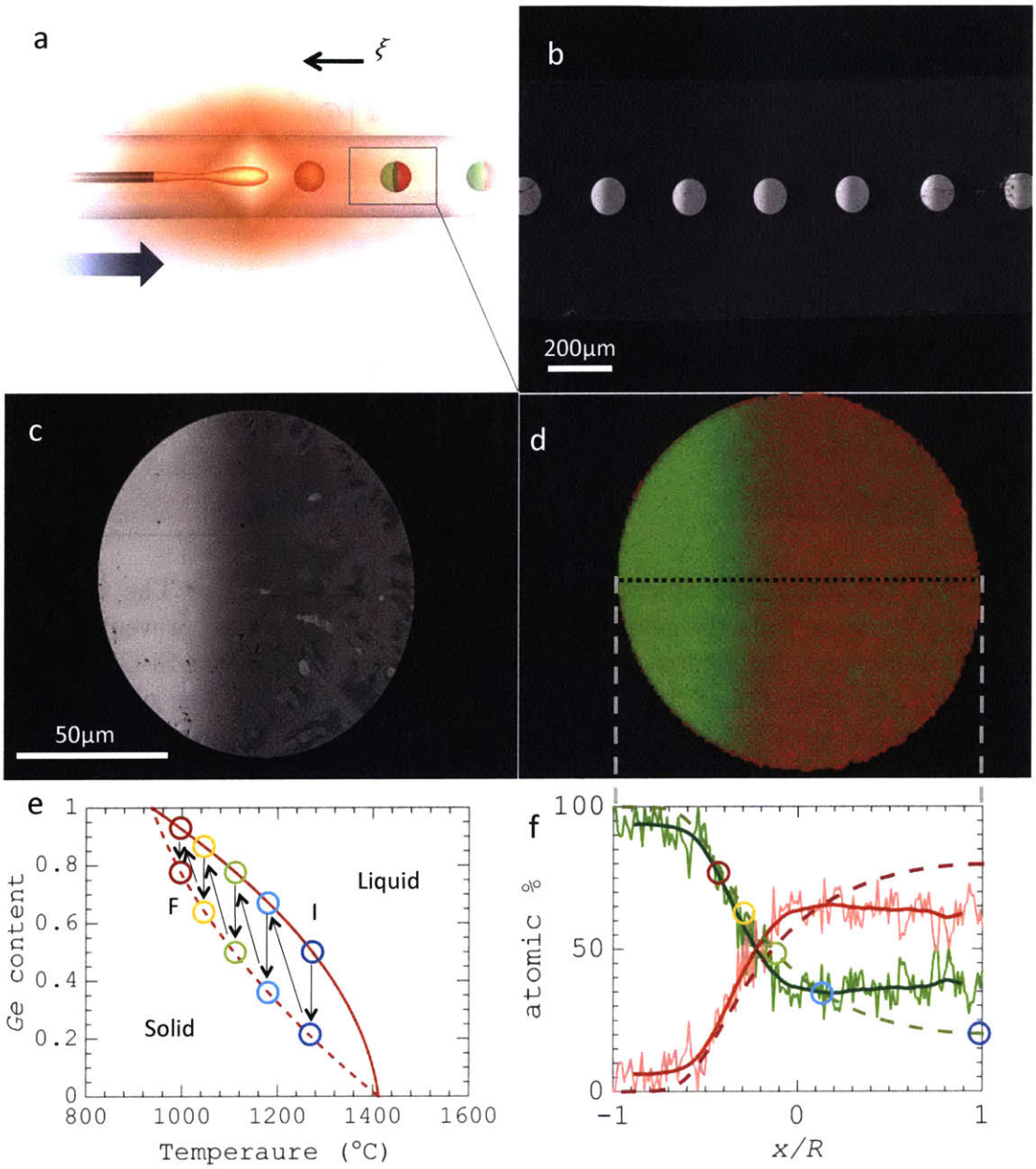

Figure 5-4: (**a**) Schematic of flame-breakup process for Si-Ge particles. (**b**) SEM micrographs of Si-Ge particles embedded in silica fiber. Brighter regions in spheres indicate Ge-rich areas. (**c**) SEM close-up on an individual Si-Ge particle - again brigther regions indicate Ge-rich areas. (**d**) EDS mapping of silicon (red) and germanium (green) on sphere. (**e**) Phase diagram of Si-Ge with projected solidifcation pathway from I to F. (**f**) Si/Ge atomic content along dashed line of image above. Measured data in solid lines are overlaid with theoretical calculations in dashed lines.

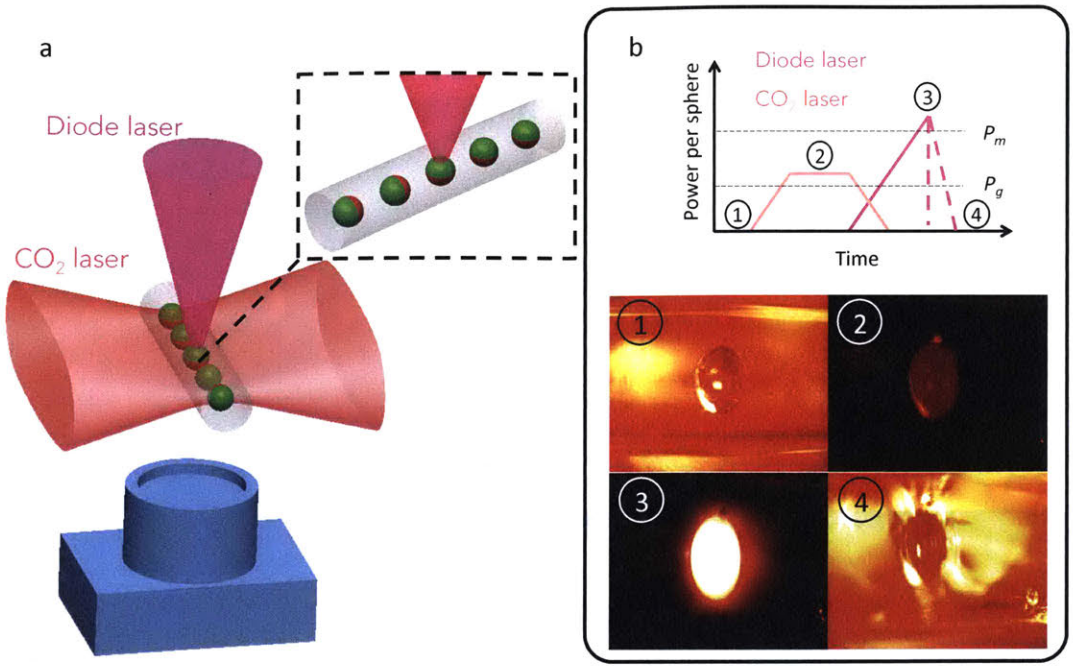

Figure 5-5: (**a**) Schematic description of the experimental setup. The CO_2 laser illuminates the fiber from the side to prefeat the silica cladding and prevent fracture; while the diode laser illuminates the fiber from the top and melts the Si-Ge particles. (**b**) Schematic description of the preheating and heating process. The silica cladding is first preheated with the CO_2 laser (steps 1 and 2) above the power threshold P_g. The sphere is then melted by heating with the diode laser above melting threshold power P_m (step 3). Finally the sphere is recrystallized by turning off the diode laser at a prescribed rate (step 4).

5.3 Recrystallization of Si-Ge particles

5.3.1 Laser-recrystallization method

Here, a post-breakup particle is illuminated perpendicularly to the fibre axis by a focused diode laser beam at a wavelength of 808 nm, with a spot size of about 50 μm. In order to prevent the cracking of the cladding, which might occur as a result of the stress applied by the droplet on its cladding due to an anomalous expansion of diamond-cubic semiconductor upon solidification, we uniformly preheat and soften it with a CO_2 laser (Figure 5-5.a). The absorption length of silica and silicon at 808 nm is about 1.5 m and 12.5 μm, respectively. Therefore, the diode laser radiation is expected to be transmitted by the silica cladding but to be absorbed by the particle,

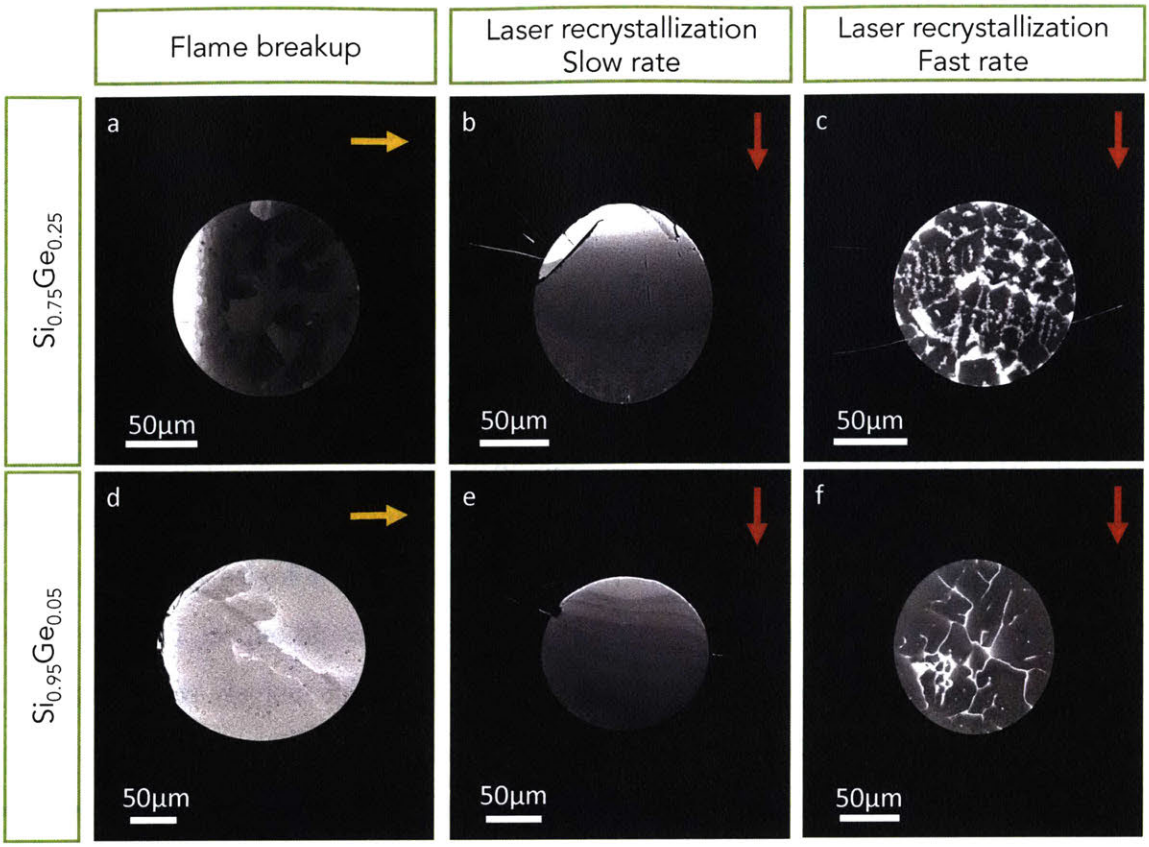

Figure 5-6: Summary of the morphologies obtained from flame breakup, slow laser recrystallization and fast laser recrystallization, on particles of different compositions. The arrows indicate either the direction of the fiber motion in the flame, or the direction of the diode laser. In both cases it points in direction opposite to the positive thermal gradient.

which heats. Once the particle is molten, the laser power is gradually reduced and the particle cools down and recrystallizes, while exposed to a thermal gradient defined by the diode laser direction. The process is schematically represented in Figure 5-5.b. By controlling the laser shut-off rate we can effectively control the cooling conditions and the magnitude of the imposed temperature gradient.

5.3.2 Morphologies with rate and composition

We have recrystallized spheres of $Si_{0.75}Ge_{0.25}$ and $Si_{0.95}Ge_{0.05}$ under different laser shut-off rates, as shown in Figure 5-6. Spheres recrystallized by abrupt laser diode shut-off led preferentially to cellular structures with no axial distribution, whereas spheres

recrystallized at low shut-off rates displayed Janus morphologies aligned along the diode laser direction. We can therefore control the microstructure of Si-Ge particles by simply controlling the shut-off rate of the laser, as well as reorient the axis of the Janus particles by choosing the diode laser direction.

5.3.3 Role of constitutional supercooling

To explain the microstructure's dependence on the laser shut-off rate, we need to understand what governs the stability of the solidification front propagation in the Si-Ge system. In general, a solid-liquid interface propagating into a supercooled melt tends to become unstable, resulting in dendritic or cellular morphologies [Balluffi et al., 2005]. For a proof of this, see Appendix B. Therefore, one could expect that the large degrees of supercooling associated with abrupt cooling are exclusively responsible for the cellular structures. However, in silicon or germanium spheres, the latent heat released even from the partial solidification is enough to reheat the spheres back to their melting point, thus arresting solidification altogether [Nagashio et al., 2005]. To convince ourselves of that, let's assume a fraction f of the sphere solidifies dendritically in the presence of a large supercooling. This leads to a release of latent heat of $f\Delta H_M$, where ΔH_M is the enthalpy of fusion. We can neglect the heat transfer towards the silica cladding, which will occur on a longer timescale owing to the much lower heat diffusivity of silica compared to solid and liquid Si-Ge. Therefore the latent heat is entirely released to the droplet, which leads to a temperature increase. Assuming the heat capacity C_P of the liquid and solid semiconductors is similar, which is true for silicon and germanium, we can approximate the temperature increase by equation the latent heat release to the change in enthalpy due to heating:

$$f\Delta H_M = C_P \Delta T \Longrightarrow \Delta T = \frac{f\Delta H_M}{C_P} \tag{5.1}$$

If we now consider the possibility of complete dendritic solidification ($f = 1$) from an initial large supercooling, we can compute the actual temperature increase of the droplet. We took the enthalpy of fusion and heat capacity of pure silicon at 1,400°C

[Nagashio et al., 2005], leading to:

$$\Delta T = \frac{1800\text{kJ/kg}}{1.0\text{kJ/(kg.°C)}} = 1800°\text{C} \tag{5.2}$$

This value is higher than the melting point of pure silicon (and any composition of Si-Ge alloy), meaning that no degree of undercooling is sufficient to lead to complete dendritic solidification.

Consequently, there must be another source of instability causing cellular morphologies to develop across the entire sphere volume. This mechanism is known as constitutional supercooling [Tiller et al., 1953; Balluffi et al., 2005]. The Si-Ge system is not characterized by a single melting temperature but by a solidus-liquidus curve (Figure 5-4.e) setting the temperature at which solid starts forming at a given germanium composition. When Si-Ge is solidified, germanium is extruded into the melt because of the solubility difference between the solid and liquid phase, causing a concentration transient spike at the interface [Balluffi et al., 2005]. On one hand, the germanium diffusion rate in the liquid defines a concentration profile which in turn defines a local liquidus temperature profile. On the other hand, the rate of heat transfer sets the actual temperature profile in the system. Two scenarios are possible:

a If the rate of germanium diffusion in the liquid is slow compared to the solidification front propagation, the actual temperature gradient at the interface will be lower than the liquidus temperature gradient defined by the germanium concentration profile. This defines a finite region of space where the actual temperature in the melt is lower than the liquidus temperature, i.e. a region where the liquid is constitutionally supercooled [Tiller et al., 1953; Balluffi et al., 2005]. Solidification then becomes unstable and may result in the formation of a cellular or dendritic structure [Tiller et al., 1953; Balluffi et al., 2005].

b Inversely, if the rate of germanium diffusion in the liquid is faster than the rate of solidification, the liquid temperature will be higher than the local liquidus temperature everywhere and the solidification proceeds in a stable planar manner [Tiller et al., 1953; Balluffi et al., 2005].

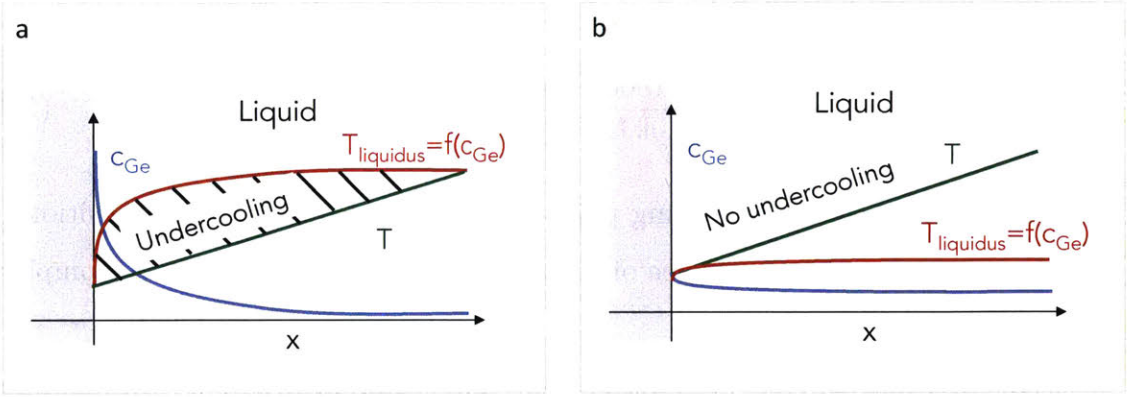

Figure 5-7: Illustration of constitutional supercooling. (**a**) Case of slow germanium diffusion in the melt compared to solidification front propagation - the melt is constitutionally supercooled and the interface is unstable. (**b**) Case of fast germanium diffusion in the melt compared to solidification front propagation - the melt not supercooled and the interface is stable.

5.4 Pressure buildup in silicon and germanium particles

5.4.1 Principle of pressure generation

The in-fibre solidification of particles not only has interesting consequences for Si-Ge alloys but also for pure silicon or germanium particles. Owing to their diamond cubic crystal structure in ambient conditions, silicon and germanium are known to expand upon solidification. When the post-breakup droplets reach the solidification temperature, they are restricted to their liquid volume by the relatively stiff surrounding silica cladding. The anomalous expansion upon solidification will thus cause the droplets to strain the surrounding silica as well as to develop internal compressive stress, much like a water bottle in the freezer.

To convince ourselves, we can consider the limiting cases described schematically in Figure 5-8. If silicon, for instance, were solidifying in an infinitely compliant matrix (*e.g.*, air), its volume would expand by a factor $\alpha = 1-\rho_{\mathrm{sol}}/\rho_{\mathrm{liq}}$ without developing any internal stress. By constrast, if a silicon particle were to expand in an infinitely rigid matrix, then its volume would remain constant but consequently it would develop an

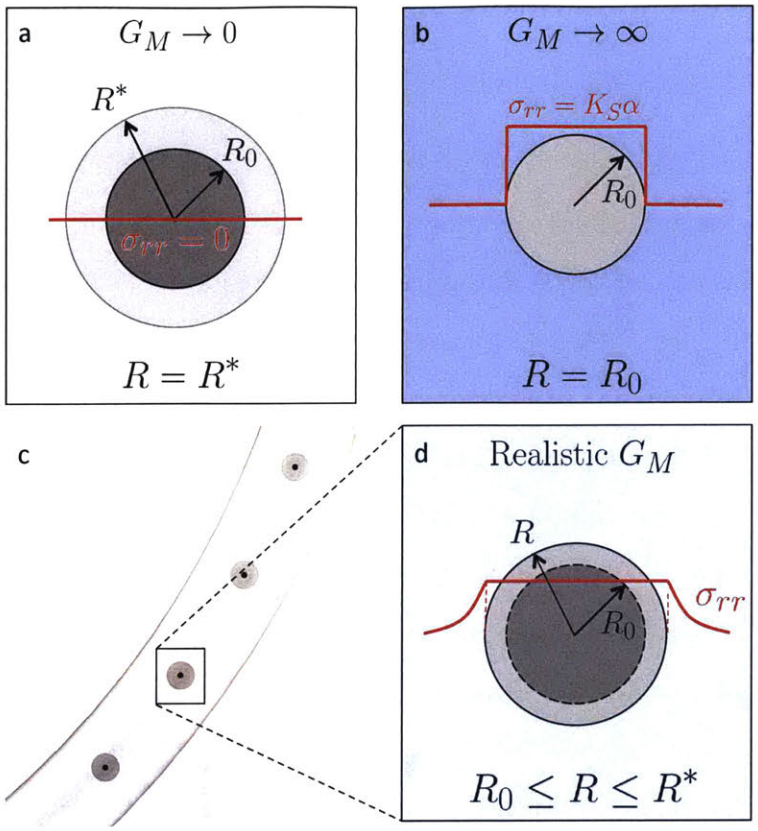

Figure 5-8: Schematic depiction of a silicon sphere solidifying in matrices of different compliances.

internal hydrostatic pressure $P = K_S\alpha$, where K_S is the bulk modulus of solid silicon. For the intermediate scenario closer to reality where the particle would solidify in a finite compliance matrix, it would expand to strain the surrounding matrix as well as develop internal stresses. The detailed calculation in an infinitely large matrix is developed in Appendix C and leads to a hydrostatic pressure in the sphere of:

$$P = \frac{4K_S G_M}{3K_S + 4G_M} \cdot \alpha \tag{5.3}$$

where K_S is the bulk modulus of the sphere material, G_M is the shear modulus of the matrix, and α is the expansion coefficient of the sphere material upon solidificaiton. For silicon in silica for example this leads to $P = 2.9$ GPa in the sphere.

5.4.2 Pressure generation in silicon-in-silica particles

Photoelastic measurements

In order to observe this effect and try to estimate the pressure, we relyed on a photoelastic measurement. If present, the strain field in silica alters its refractive index and causes the material to become birefringent, which we can observe using cross-polarizers (cf. Figure 5-9.b). Contrary to the region around the spheres, the intact section of the core remains unstressed. The birefringence pattern around the spheres shown in Figure 5-9.c displays a 4th-order rotational symmetry as well as multiple Michel-Levi rings [Einhardt et al., 2012]. By taking into account the photoelastic coefficients of silica, it is possible to compute the expected birefringence patterns for arbitrary stresses at the silica/semiconductor interface and give upper and lower bounds to the surface stress by matching the number of rings with the experimental patterns. The exact calculations were performed by Dr. Alexander Gumennik and will not be detailed in this thesis. This method enables us to define the range of surface stresses coherent with a given number of rings. For a 35 μm diameter silicon droplet, the surface stresses were between 0 and 0.9 GPa, while for a 450 μm diameter silicon droplet the surface stresses lied between 0.15 and 0.22 GPa. Although consistent with a state of a high internal stress, these values differ quite significantly from the theoretically derived stress and the measurement lacks precision.

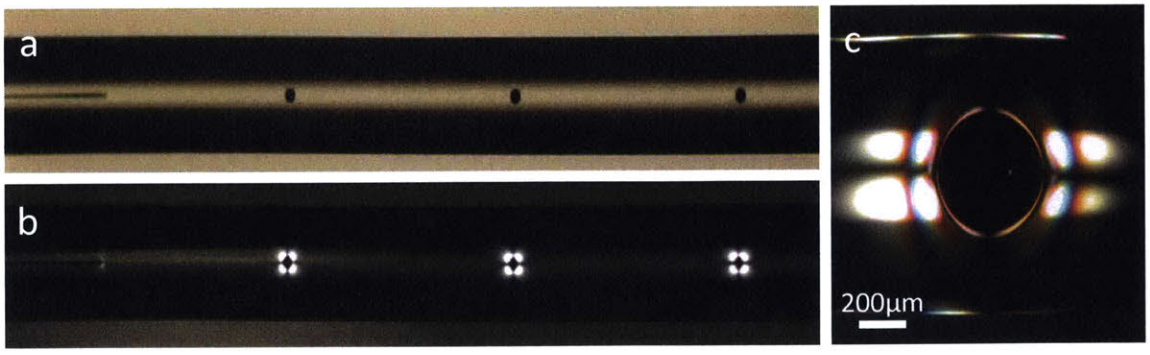

Figure 5-9: (**a**) Optical micrograph of a fiber with partially broken-up core. (**b**) Sample sample viewed under cross-polarizers. Birefringence patterns are visible around spheres but not around core regions. (**c**) Close-up on birefringence pattern around a particle embedded in the fiber.

Raman spectroscopy

We decided to evaluate stress through an alternative method, by performing Raman spectroscopy on silicon spheres and comparing to continuous core sections. According to Sui et al., for hydrostatically stressed silicon the shift of the first order Raman peak frequency ω depends on the pressure P according to:

$$\frac{\mathrm{d}\omega}{\mathrm{d}P} = 5.2 \pm 0.3 \frac{\mathrm{cm}^{-1}}{\mathrm{GPa}} \tag{5.4}$$

Raman measurements on 35 μm and 450 μm diameter silicon droplets shown in Figure 5-10 indicate a shift in the silicon peak location of 10.5±0.2 cm^{-1} and 4.7±0.1 cm^{-1} respectively. These shifts translate into hydrostatic stresses of 2.02±0.07 GPa and 0.90±0.06 GPa, respectively. Such GPa-level compressive stresses on silicon would generally require complex diamond-anvil presses, whereas here the stress state is applied by the silica cladding alone.

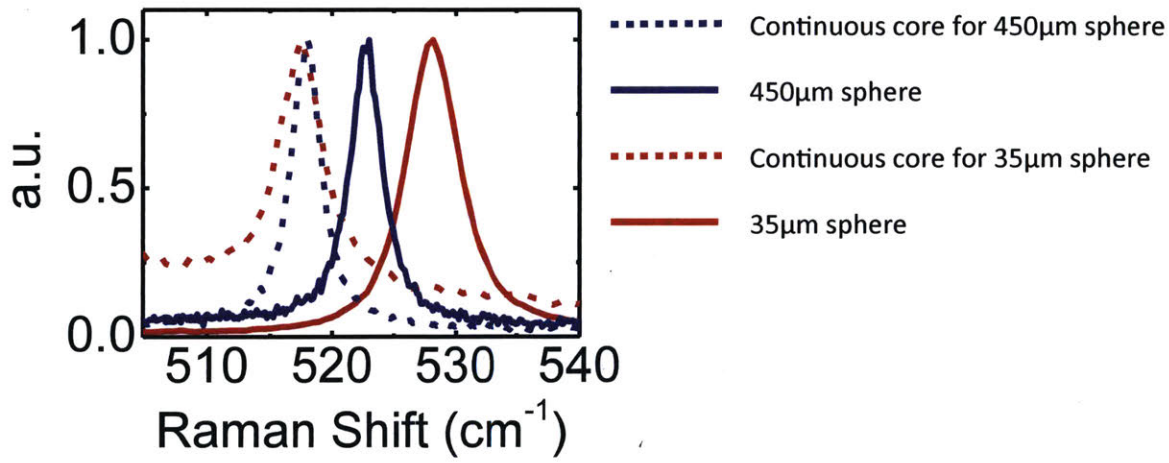

Figure 5-10: First order Raman peaks in silicon continuous core and spheres of different sizes.

5.4.3 Discussion and possible pressure focusing effect

Although birefringence observations and Raman spectroscopy are consistent with a state of high stress in the spheres, the measurements differ quite significantly from the theoretical prediction made from Equation 5.3. Not only are the values of pressure different from the numerical prediction, but more importantly their seems to be a strong effect of sphere size which is completely absent from the predicted pressure.

Our assumption is that finite-cladding effects are important as well proper account of the solidification kinetics. Silicon spheres are likely to solidify gradually, much like the Si-Ge particles in previous sections, from the coldest point to the hottest. This is likely to cause a "pressure focusing" effect, where the parts of the sphere solidifying last will likely be under higher compressive stress. The Raman measurements penetrate within 10μm of the sphere surface owing to the Raman laser wavelength of 784nm being rapidly absorbed [Green and Keevers, 1995] - therefore not probing the whole volume.

Appendix D details the calculation of the stresses within a sphere solidying progressively from its exterior surface inward in a spherically symmetric fashion. In this scenario, when a thin spherical shell solidifies its volume expands, and the remaining liquid in the core of the droplet is further compressed. Radial stress continuity at the liquid/solid interface causes the stress in the growing solid shell to rise upon advancement of the solidification front. The calculations leads to Figure 5-11 which shows the pressure in a sphere solidifying in such a way as a function of radial position, illustrating a possible "pressure focusing" mechanism. In fact the pressure and stress fields diverge close to sphere center; this is obviously not physical, but our model does not take into account probable yielding or fracturing of the material which in practice would occur. However pressure focusing could in principle still lead to pressures close to 10-11 GPa close to the sphere center, a value which could induce the appearance of β-phase silicon for example [Hu and Spain, 1984]. No direct observation of high internal pressures could be made, but future work should focus on attempting to probe stresses or lattice spacings in the sphere volume as opposed to its periphery.

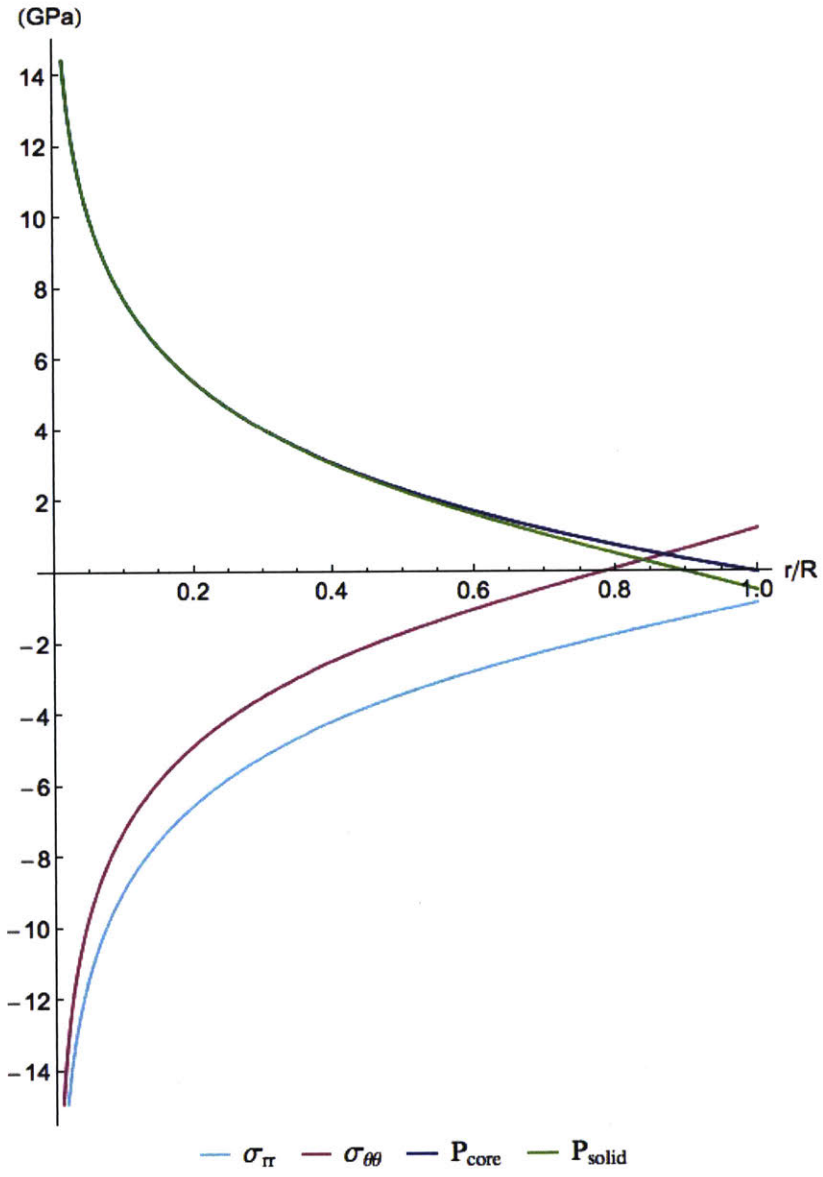

Figure 5-11: Stress fields and pressure as a function of radial position in a sphere solidifying progressively from the external surface inward, based on calculations developed in Appendix D. P_{solid} is the pressure in the solidified sphere, while P_{core} is the pressure in the liquid core when the solidification front is at a position $\xi = r/R$.

5.5 Discussion

To conclude, we have shown that the in-fibre breakup method is able to produce Si/Ge microparticles with a well-defined and controllable Janus morphology and silicon microparticles with a high level of internal stress. The stresses arising from anomalous expansion of silicon in silica are on the GPa level, which would potentially narrow down the bandgap by tens of meV thus broadening the wavelength range of the in-fibre particles for optical detection purposes [Healy et al., 2014]. In addition, the Janus particles produced by slow cooling Si-Ge droplets represent a main finding, with potential applications in components of traditional radio-frequency circuitry or in quantum computing, if successfully scaled down to nanometric regime which was shown to be potentially possible elsewhere [Kaufman et al., 2012; Gumennik et al., 2013]. Furthermore, combining our ability to reorient particles through laser recrystallization with the idea of selective breakup [Rein et al., 2016] one can envision building in-fibre arrays of Si-Ge Janus particles connected across the junction to metallic buses, thus paving the way towards fully integrated in-fibre microelectronics.

Chapter 6

Conclusions and future directions

This thesis presents the methodology and some applications of the concept of phase separation in thermally-drawn fibers. It does so first through a general framework for the incorporation of porous domains in thermally-drawn fibers. Later this methodology is applied towards fibers for neural scaffolding, and Li-ion fiber batteries. In this conclusion chapter we wish to expand upon these avenues, and point at potential future interesting research studies or applications.

6.1 Porosity generation in fibers

6.1.1 Studies around in-fiber thermally-induced phase separation

The method presented in the thesis for incorporation of porous domains in fibers revolves around the thermally-induced phase separation of a polymer solution contained in a cladding reservoir. One could push the results presented here into different directions:

New materials

We demonstrated the method with PCL and PVdF, guided by two applications (neural scaffold and battery respectively). An interesting and useful next step would be

to broaden the set of porous materials. The TIPS methodology can be employed over a broad range of polymers [Cui et al., 2013] with different solvents, used for a variety of applications. It would be interesting to screen for cladding materials, and polymer/solvent systems that would be compatible with the drawing process to expand the list of useable materials.

Quantitative study of pore size versus quenching temperature

In subsection 2.3.2, we presented data on pore size versus quenching temperature for a solution of PCL in PC/Triglycol exhibiting a liquid-liquid demixing behavior. We gave a qualitative explanation of the behavior. An in-depth analysis of the pore size versus quenching temperature based on standard coarsening theories would an interesting study, perhaps leading to predictive capabilities for other solutions exhibiting a similar behavior.

In-line quenching for pore size control

Besides a detailed analysis of the effect of quenching on pore size, the design and fabrication of a quenching apparatus in-line with the drawing process, used to rapidly cool fibers to a desired quenching temperature as they exit the furnace would be a useful feature for this fabrication method - as it would enable direct single-step control over the microstructure

6.1.2 Alternative methods for porosity generation

Besides thermally-induced phase separation, other methods could be considered to introduce in-fiber porosity.

Porogen leaching

The method of porogen leaching for the production of porous polymer generally involves the following steps. First a mixture of host polymer and porogen is generated. The porogen can be a crystalline material such as salt, or another polymer thus

forming a blend with the host polymer. Then the porogen is leached out with an appropriate solvent - eg. water for water-soluble salts, or an organic solvent for polymer porogens [Strathmann, 2011]. This concept could also perhaps be used with the drawing process - either in combination of the TIPS method for pore size tunability or as a standalone method. Contrary to the TIPS method, the porosity would not be generated in a single-step, but would require a post-processing step to leach out the porogen which could limit practicality.

Diffusion-induced phase separation

In non-solvent diffusion-induced phase separation, the phase separation of a polymer/solvent binary solution is not induced through cooling but through direct contact of the solution with a non-solvent for the polymer. Mass exchanges at the interface, specifically diffusion of solvent out of the solution and into the non-solvent bath, change the local concentration and trigger a phase separation mechanism that can lead to porosity with an appropriate choice of polymer/solvent/non solvent [Van de Witte et al., 1996]. This method could also be employed in the context of thermal-drawing. In this case, a polymer solution would be introduced in a cladding reservoir and drawn. At the end of the drawing process, the fiber would still contain the polymer solution in a homogeneous state. Immersion of the cladding in an organic solvent chosen to be a good solvent for the cladding polymer, but a non-solvent for the solution polymer, would slowly dissolve the cladding and trigger the phase separation of the solution as the latter is exposed once the cladding is removed. This slow phase separation process (slowed by the removal of cladding) could lead to interesting microstructures.

6.2 Fibers with external porosity

Chapter 3 presents results of the TIPS methodology applied for the fabrication of a neural fiber scaffold with porous windows. The type of fiber structures presented here are more general then this specific application - and fall into the category of fibers

with external porosity, ie. fibers that have a porous domain connecting the inside of the fiber to its environment. These fibers would have the ability to either intake material from the environment directly, or to release chemicals into the environment.

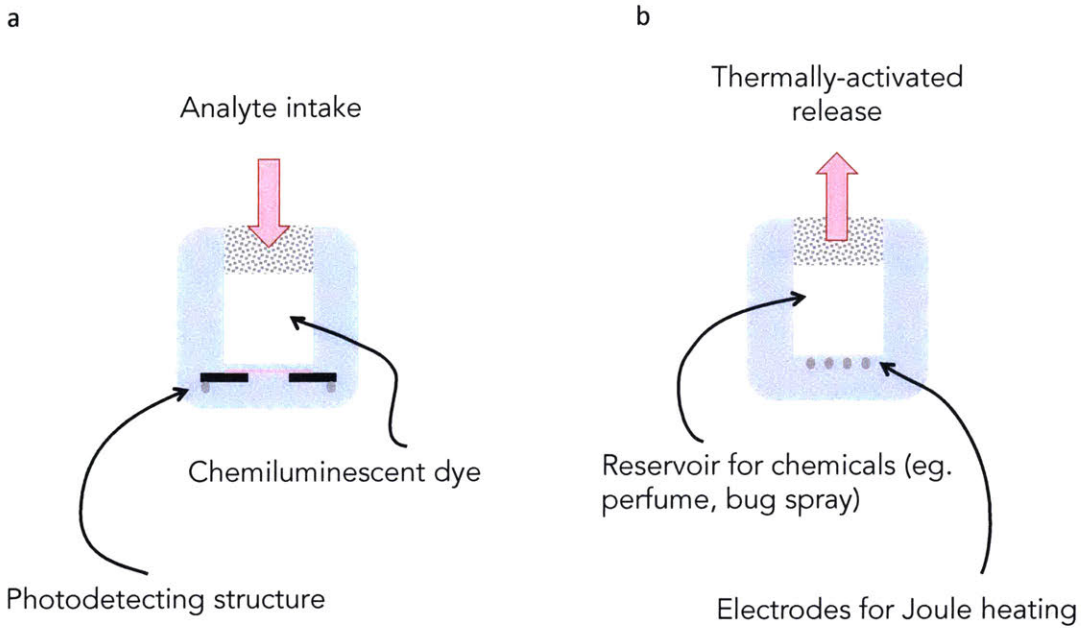

Figure 6-1: Schematics of fibers with external porosity. (**a**) Fiber for gas sensing, with porous window for analyte intake, hollow core with chemiluminescent dye, and photodetecting structure. (**b**) Fiber for volatile release, with porous window for chemical diffusion, hollow core for storage of chemical, and electrodes for Joule heating and activated release.

Fibers for sensing

In the first scenario, fibers with external porosity could be used to intake gases or liquids directly from the environment in the transverse direction - as opposed to from the ends of the fiber. This could be extremely useful for gas sensing fibers for instance. Gumennik et al. have introduced the concept of gas sensing fibers. In their fiber, hydrogen peroxide diffuses from the ends into a hollow-core containing a chemiluminescent dye emitting light at an intensity scaling with the concentration of analyte. The cladding contains a photodetecting structure then transducing the light intensity signal into an electrical signal. They note that the tip-limited diffusion is a

limitation of the sensor - while direct transport of H_2O_2 in the transverse direction would enable detection throughout the entire length of the fiber. A fiber structure similar to that shown in Figure 6-1.a would in theory solve the problem. A porous window could enable direct diffusion of analyte from the environment into the core in a fiber length-independent way, while a similar detection mechanism as Gumennik et al. could allow for detection.

Fibers for chemical release

In the section scenario, the porous windows could be used to transfer mass from a hollow-core acting as a reservoir into the environment. Figure 6-1.b shows an example of such a structure. We can envision Joule heating as a mechanism for release of volatiles. Through heating, the vapor pressure of the volatile in the core would increase according to the Clausius-Clapeyron equation - thus increase evaporation of volatiles out of the core and through the porous window. This could for example be used for the release of perfumes or insect repellants.

6.3 Fibers with internal porosity

Chapter 4 shows an application of fibers with internal porous domains, mediating the transport of ions in the context of a Li-ion fiber battery. Addtional applications can be pursued with similar structures exhibiliting internal porosity, or internal polymer solutions. We can cite here supercapacitor fibers, with similar structures as the battery, but storing charges through an electrical double layer at the interface of the electrodes and the gel electrolyte. Secondly, fibers with internal solutions exhibiting thermally-induced phase separation could find applications as phase-change materials for heat regulation. With an appropriate choice of solution, an increase in temperature would lead to homogenization of the solution and associated with a latent heat absorption thus limiting temperature increase of the wearer or substrate. Reversely, cooling of the environment would be associated with phase separation and latent heat release from the solution.

Appendix A

LDPE surface grafting step-by-step

Glassware and equipment

- 1× 1L three-neck flask, 24/40 joints (VWR: 80069-456)
- 3× Rubber stopper, 24/40 joints (VWR: 89097-544)
- 2× 500ml HDPE bottle (VWR: 414004-114)
- 2× 15mm stir bar (VWR: 58948-218)
- 1× 10"-long tweezers (McMaster-Carr: 7379A23)
- 1× Balance, maximum weight >400g if available
- 1× Vacuum oven
- 1× Plasma cleaner (at MIT CMSE: Barrick Plasma PDC-32G)
- 1× Schlenk line with stir plate and temperature controller
- 1× 1L-flask heating mantle (VWR: 33787-134)

Materials and chemicals

- LDPE preform part or film to be surface-grafted (McMaster-Carr)
- ϵ-caprolactone (ϵ-CL), 99% (Alfa-Aesar: A10299)
- Tin(II) 2-ethylhexanoate ($Sn(Oct)_2$), 96% (Alfa-Aesar: B23612)
- Nitrogen gas, industrial grade (Airgas: NI 300)
- Chloroform, 99.8% (Alfa-Aesar: 32614)
- Isopropyl alcohol (VWR: 89370-086)
- PTFE sheet, 1/8" × 2" × 6" (McMaster-Carr)

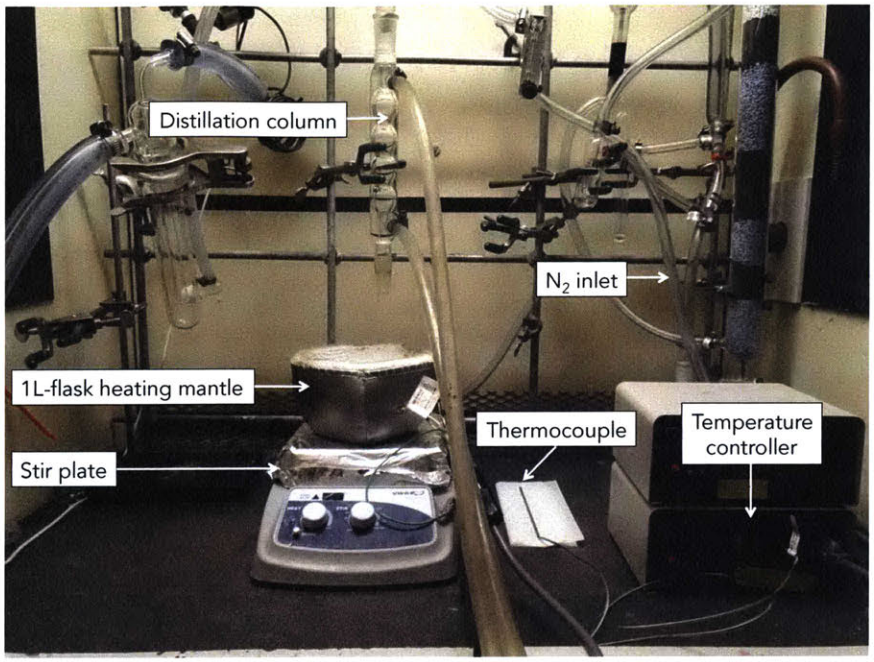

Figure A-1: Photograph of Schlenk line fume hood before at preparation step.

Step-by-step

Preparation step

1. Rinse a clean flask with ϵ-CL
2. Dry flask and stir bar overnight in a vacuum oven at 90°C under vacuum
3. Rinse HDPE bottle with ϵ-CL. Tare after rinsing.
4. Preweigh 400g of ϵ-CL in HDPE bottle.
5. Drill hole in rubber stopper at an angle with roughly 2-3mm drill bit. Mark rubber stopper with a "**T**". This will be used to insert thermocouple in flask.
6. Check Schlenk line - compare to Figure A-1. Namely make sure that:
   - Distillation column with 24/40 joint is connected
   - High purity nitrogen gas is connected
   - Temperature controller, 1L-flask heating mantle, and thermocouple are connected
   - Stir plate is connected

Plasma cleaning step

1. Preheat empty plasma cleaner: O_2 pressure: 800-1000 mTorr; RH power: "High"; Duration: 5min.
2. During preheat add 5508 μl of Sn(Oct)2 in flask. Close with rubber stoppers.
3. Insert LDPE sample in plasma cleaner on PTFE sheet. Make sure surface to be treated is facing up.
4. O_2-plasma treat sample: O_2 pressure: 800-1000 mTorr; RH power: "High"; Duration: 10min.
5. During plasma treatment, insert preweighed 400g of ϵ-CL in flask. Close with rubber stoppers and agitate vigorously by hand for 5min.
6. Ultrasonicate flask in ultrasonicator bath for 3min to remove as much bubbles on the surface as possible.
7. When plasma cleaning is done, rapidly insert LDPE sample in flask facing down in the bath with long tweezers.
8. Visually inspect surface LDPE surface looking from the bottom of the flask. Shake LDPE sample to remove trapped bubbles. Close with rubber stoppers - make sure that marked rubber stopper is on a side neck.

Polymerization step

1. Rapidly transfer flask to Schlenk line.
2. Insert flask center neck in distillation column and place bottom of flask in heating mantle. Place heating mantle on stir plate.
3. Insert thermocouple in marked and drilled rubber stopper. Probe should be inserted as deep as possible, and as close as possible to flask walls to limit overheating.
4. Turn heater on. Set temperature to 80°C. Mark $t = 0$.
5. Turn stir plate on. Set stir rate to $\approx$300 RPM.
6. Open nitrogen tank. Make sure nitrogen is flowing by checking bubbler.

7. Open Schlenk line valves to allow nitrogen to flow in flask. Control flow rate to ≈0.2-0.3 lpm (liters per minute).
8. Wrap flask with aluminum foil.
9. Check on flask regularly to make sure it is not overheating.
10. Prepare long tweezer, stir bar, and 500ml HDPE bottle for end of reaction.

Sample rinsing and drying step

1. At t = 24hrs, turn temperature controller and stir plate off. Close nitrogen tank. Remove flask from Schlenk line.
2. As rapidly as possible, extract LDPE sample from flask with long tweezers and insert in 500ml HDPE bottle.
3. Fill bottle to top with chloroform. Insert clean bar. Close bottle.
4. Place bottle on stir plate, set stir rate to ≈500 RPM. Wait 2hrs. Sample must be clean with no polycaprolactone homopolymer chunk on surface.
5. Remove sample. Rinse in isopropyl alcohol.
6. Place sample in desiccator and dry under vacuum until preform assembly.

Appendix B

Stability of a solid/liquid interface during solidification of a unary system

Here we demonstrate the premise of the constitutional supercooling argument, which is that the solidification front of a unary system solidifying in a supercooled melt is unstable, following the argument of Balluffi et al..

First, let us consider a planar interface between a liquid and solid at a position $x = \xi(t)$ propagating at a velocity v into the liquid. In an infinitesimal increment of time $\mathrm{d}t$, the solidification front progresses by an amount $\mathrm{d}x = v\mathrm{d}t$. The energy

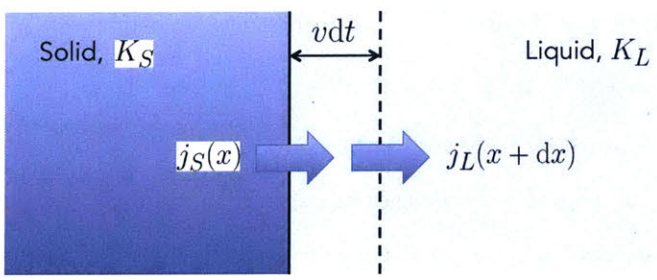

Figure B-1: Schematic of a solid-liquid interface propagating into the liquid at a velocity v

balance on the slab of material $\mathrm{d}x$ leads to:

$$\begin{aligned} v\mathrm{d}t \cdot \rho \cdot \Delta h_{L\to S} &= j_S(x) - j_L(x+\mathrm{d}x) \\ &= -K_S \left[\frac{\partial T_S}{\partial x}\right]_{x=\xi(t)} + K_L \left[\frac{\partial T_L}{\partial x}\right]_{x=\xi(t)} \end{aligned} \tag{B.1}$$

Where $\Delta h_{L\to S} = -\Delta h_M$ is the volumetric enthalpy of solidification, $K_{S,L}$ are the thermal conductivities in solid and liquid, ρ is the density of the solid. We assumed that heat transfer into the liquid is occuring through diffusion, a reasonable assumption considering convection is negligible in the boundary layer close to the interface. Furthermore we took $j_L(x+\mathrm{d}x) \approx j_L(x)$.

Thus the velocity of the propagating front is then governed by:

$$v = \frac{1}{\rho \Delta h_M} \cdot \left[K_S \frac{\partial T_S}{\partial x} - K_L \frac{\partial T_L}{\partial x}\right]_{x=\xi(t)} \tag{B.2}$$

Let us now consider the effect of a perturbation on the solidification front in two cases: when the liquid is superheated (*i.e.* above the melting temperature), and when the liquid is supercooled with respect to the melting temperature. For simplicity we will assume the temperature in the solid is constant, *i.e.* $\partial T_S/\partial x = 0$; in practice this does not change the argument.

Propagation in a superheated liquid

The temperature at the S/L interface is, by definition, equal to the melting temperature T_M. Therefore the heat flux in the liquid is positive towards the interface. Close to a protrusion, the magnitude of the temperature gradient is higher. This is the thermal equivalent of the "sharp-edge effect" in electrostatics. To convince ourselves, take for example a spherical solid solid particle of radius R and surface temperature set to T_M. In practice, this is a good model for a protrusion close enough to the interface. At equilibrium, the temperature in the surrounding liquid will be the solution of the heat equation:

$$\nabla^2 T_L = 0 \Leftrightarrow \frac{\partial}{\partial r}\left(r^2 \frac{\partial T_L}{\partial r}\right) = 0 \tag{B.3}$$

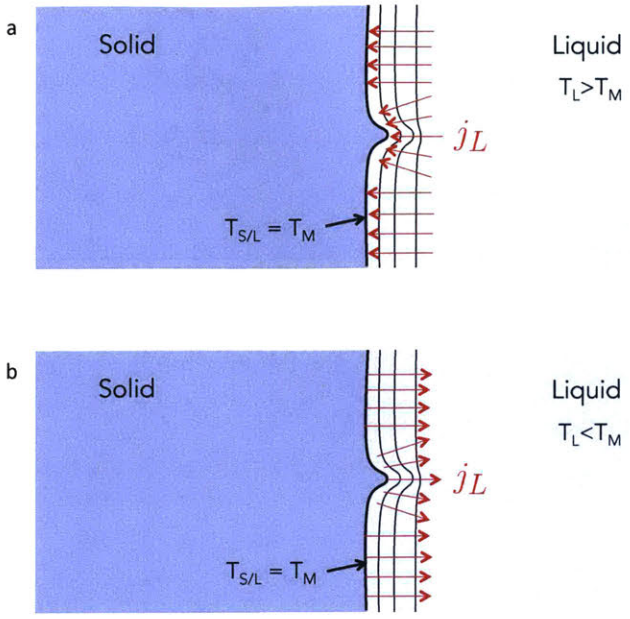

Figure B-2: Schematic of a solid-liquid interface propagating into the liquid at a velocity v

Solving the equation with boundary condition then leads to:

$$\begin{aligned} \left[\frac{\partial T_L}{\partial r}\right]_{r=R} &= (T_L^{\infty} - T_M) \cdot \frac{1}{R} \\ &= (T_L^{\infty} - T_M) \cdot \frac{\kappa}{2} \end{aligned} \tag{B.4}$$

Where κ is the curvature of the spherical particle. This proves that the magnitude of the temperature gradient in the liquid is always greater near a protrusion, characterized by a large value of curvature κ compared to a flat region of the interface.

Going back to Equation B.2, we see that close to a protrusion we therefore have a negative velocity meaning that the protrusion will actually melt back so that the solid/liquid front is stable. In practice the larger gradient causes a larger heat flux which melt back solid protrusions.

Propagation in a supercooled liquid

Similarly, for a solid propagating in a supercooled liquid the temperature at the S/L interface is set to T_M, and now the thermal gradient in the liquid is negative causing a positive heat flux from the interface outward. Using the same argument as above, we know that the magnitude of the temperature gradient will be higher close to a protrusion where the curvature κ is greater. With Equations B.2 and B.4 this now means that the velocity of the S/L front close to a protrusion is positive, and greater in magnitude than away from the protrusion:

$$0 < v_{\text{flat}} < v_{\text{protrusion}} \tag{B.5}$$

Hence, the S/L interface is unstable for a solid propagating into a supercooled liquid: any perturbation on the interface will tend to grow and evolve into dendrites.

Appendix C

Homogeneous solidification scenario

We consider a sphere of radius R made of a material S in the liquid state, and embedded in an infinite matrix of a material M in the solid state. We assume that prior to solidification, both the liquid and solid are stress-free. We consider now that the sphere homogeneously solidifies. In the process, the material acquires a purely dilatational stress-free strain of $\epsilon^*_{ij} = \frac{\alpha}{3}\delta_{ij}$, where $\alpha = 1 - \rho_{\text{sol}}/\rho_{\text{liq}}$ is the volume change upon solidification, and δ_{ij} is the Kronecker delta. We seek to determine the stress, strain and displacement fields generated by the solidification process both in the sphere of material S and the matrix M.

For obvious symmetry arguments, we choose to work in spherical coordinates with the origin at the center of the sphere. We furthermore take the displacement field in both M and S to bear the form:

$$\underline{u}^{S,M} = u^{S,M}(r)\underline{e_r} \tag{C.1}$$

Where $\underline{e_r}$ is the unit vector in the radial direction. Assuming small displacements, the strain tensors in M and S immediately derive from the above:

$$\epsilon^{S,M}_{rr} = \frac{\mathrm{d}u^{S,M}}{\mathrm{d}r} \tag{C.2}$$

$$\epsilon^{S,M}_{\theta\theta} = \epsilon^{S,M}_{\phi\phi} = \frac{u^{S,M}}{r} \tag{C.3}$$

The total strain in M is purely elastic, whereas in S the total strain is the sum of the elastic strain and the transformation stress-free strain ϵ^*_{ij}. By assuming that both materials S and M behave as linearly elastic, we thus have:

$$\epsilon^M_{ij} = S^M_{ijkl}\sigma^M_{kl} \tag{C.4}$$

$$\epsilon^S_{ij} = S^S_{ijkl}\sigma^S_{kl} + \epsilon^*_{ij} \tag{C.5}$$

where $\sigma^{S,M}_{ij}$ are the stress tensors in both S and M, and $S^{S,M}_{ijkl}$ are the stiffness tensors in both S and M. The above expressions contain implicit sums over k and l, according to the Einstein notation.

Further considering that both materials S and M are mechanically isotropic and homogeneous, we can write the components of the stress tensors in terms of the materials bulk moduli and shear moduli, $K_{S,M}$ and $G_{S,M}$. They take the form:

- In M:

$$\sigma^M_{rr} = (K_M - \frac{2}{3}G_M)\left(\frac{\mathrm{d}u^M}{\mathrm{d}r} + 2\frac{u^M}{r}\right) + 2G_M\frac{\mathrm{d}u^M}{\mathrm{d}r} \tag{C.6}$$

$$\sigma^M_{\theta\theta} = \sigma^M_{\phi\phi} = (K_M - \frac{2}{3}G_M)\left(\frac{\mathrm{d}u^M}{\mathrm{d}r} + 2\frac{u^M}{r}\right) + 2G_M\frac{u^M}{r} \tag{C.7}$$

- In S:

$$\sigma^S_{rr} = (K_S - \frac{2}{3}G_S)\left(\frac{\mathrm{d}u^S}{\mathrm{d}r} + 2\frac{u^S}{r}\right) + 2G_S\frac{\mathrm{d}u^S}{\mathrm{d}r} - K_S\alpha \tag{C.8}$$

$$\sigma^S_{\theta\theta} = \sigma^S_{\phi\phi} = (K_S - \frac{2}{3}G_S)\left(\frac{\mathrm{d}u^S}{\mathrm{d}r} + 2\frac{u^S}{r}\right) + 2G_S\frac{u^S}{r} - K_S\alpha \tag{C.9}$$

We now proceed to applying the equilibrium condition in both M and S. In a static situation such as the one studied here, the equilibrium condition simply states that $\nabla \cdot \sigma = 0$ at any given point of the system. This yields:

$$\frac{\mathrm{d}\sigma^{S,M}_{rr}}{\mathrm{d}r} + \frac{2\sigma^{S,M}_{rr} - \sigma^{S,M}_{\theta\theta} - \sigma^{S,M}_{\phi\phi}}{r} = 0 \tag{C.10}$$

Subbing in the previous expressions for stress components leads to a very simple differential equation on the displacement fields:

$$\frac{\mathrm{d}}{\mathrm{d}r}\left[\frac{\mathrm{d}u^{S,M}}{\mathrm{d}r} + 2\frac{u^{S,M}}{r}\right] = 0 \tag{C.11}$$

Solving the previous equation exactly, one gets:

$$u^{S,M}(r) = A_{S,M}r + \frac{B_{S,M}}{r^2} \tag{C.12}$$

Where $A_{S,M}$ and $B_{S,M}$ are integration constants. We note that B_S and A_M must equal zero to ensure a finite displacement field near the origin, and zero stress at infinity respectively.

The form of displacement field must also verify the continuity relations at the sphere/matrix interface.

$$\sigma_{rr}^{S}(r = R) = \sigma_{rr}^{M}(r = R) \tag{C.13}$$

$$u^{S}(r = R) = u^{M}(r = R) \tag{C.14}$$

Subbing in the form of the displacement fields in Equations D.14 and C.14 one gets a simple linear system with solutions:

$$A_S = \frac{K_S}{3K_S + 4G_M}\alpha \tag{C.15}$$

$$B_M = \frac{K_S}{3K_S + 4G_M}\alpha R^3 \tag{C.16}$$

We thus get the exact stress, strain, and displacements fields in both the matrix M and the sphere S.

- In M, $r > R$:

$$\epsilon^M_{rr} = -\frac{2K_S}{3K_S + 4G_M}\alpha\frac{R^3}{r^3} \tag{C.17}$$

$$\epsilon^M_{\theta\theta} = \epsilon^M_{\phi\phi} = \frac{K_S}{3K_S + 4G_M}\alpha\frac{R^3}{r^3} \tag{C.18}$$

$$\sigma^M_{rr} = -\frac{4K_S G_M}{3K_S + 4G_M}\alpha\frac{R^3}{r^3} \tag{C.19}$$

$$\sigma^M_{\theta\theta} = \sigma^M_{\phi\phi} = \frac{2K_S G_M}{3K_S + 4G_M}\alpha\frac{R^3}{r^3} \tag{C.20}$$

- In S, $r \leq R$:

$$\epsilon^S_{rr} = \epsilon^S_{\theta\theta} = \epsilon^S_{\phi\phi} = \frac{K_S}{3K_S + 4G_M}\alpha \tag{C.21}$$

$$\sigma^S_{rr} = \sigma^S_{\theta\theta} = \sigma^S_{\phi\phi} = -\frac{4K_S G_M}{3K_S + 4G_M}\alpha \tag{C.22}$$

We can thus express the hydrostatic pressure inside the sphere through the definition $P = -\frac{1}{3}\ \mathrm{tr}\ \sigma^S$, we get:

$$P = \frac{4K_S G_M}{3K_S + 4G_M}\alpha \tag{C.23}$$

Appendix D

Progressive solidification scenario

We consider again the case of a sphere of radius R made of a material S originally in the liquid state, and embedded in an infinite matrix of a material M in the solid state. Prior to solidification, the system is stress-free. We now consider that the sphere S progressively solidifies from its periphery to the center, by way of an advancing solidification front. We consider the process of solidification to be quasi-static so that any dynamical effect is neglected. Because of the volume mismatch between liquid S and solid S, the hydrostatic pressure in the liquid core rises as the solidification front advances inward. Radial stress continuity at the liquid/solid interface thus causes the stress in the solid shell to also rise upon solidification. This leads to a stress "focusing" at the center of the sphere.

We wish to compute the stress field in both S when the solidification process is complete, to relate to bandgap shifts measurements.

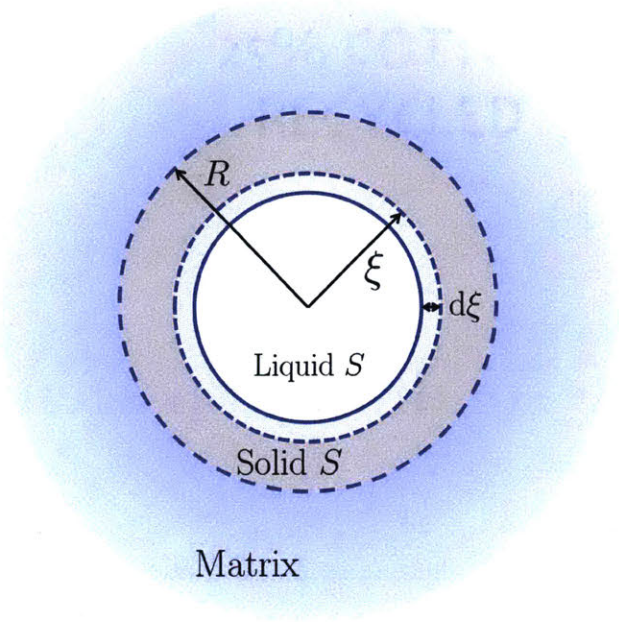

Figure D-1: Illustration of the gradulat solidification process.

Method If we neglect the stress history, the elastic field in both regions may be computed easily for a given position ξ of the solid/liquid interface, provided the liquid core pressure is known. Indeed, the system may then be considered as a simple spherical pressure vessel with internal pressure given by that in the liquid core, and constrained on the outside by the matrix. However, because of the volume mismatch between liquid and solid S, the pressure in the core rises as the solidification front progresses by an amount $\mathrm{d}\xi$. At any given point in the solid S region, this will consequently lead to a stress increment, due to the solidification of a shell of thickness $\mathrm{d}\xi$.

The problem has been treated by King & Fletcher King and Fletcher [1973] for the case of an infinitely compliant matrix. We borrow some of their notations and methodology to treat the present case of a finite rigidity matrix

1. In the absence of stress build-up, and for a given position ξ of solid/liquid interface, the system is a spherical pressure vessel with internal pressure $P(\xi)$ and constrained by the matrix M. Solutions can be derived following the same method

as that followed in the homogeneous solidification case, and we get:

- In M, $r > R$:

$$\tilde{u}^M = \frac{r}{3K_M} f_M(\xi) + \frac{g_M(\xi)}{4G_M r^2} \tag{D.1}$$

$$\tilde{\sigma}^M_{rr} = f_M(\xi) - \frac{g_M(\xi)}{r^3} \tag{D.2}$$

$$\tilde{\sigma}^M_{\theta\theta} = \tilde{\sigma}^M_{\phi\phi} = f_M(\xi) + \frac{g_M(\xi)}{2r^3} \tag{D.3}$$

- In S, $r \in [\xi, R]$:

$$\tilde{u}^S = \frac{r}{3K_S} f_S(\xi) + \frac{g_S(\xi)}{4G_S r^2} \tag{D.4}$$

$$\tilde{\sigma}^S_{rr} = f_S(\xi) - \frac{g_S(\xi)}{r^3} - K_S\alpha \tag{D.5}$$

$$\tilde{\sigma}^S_{\theta\theta} = \tilde{\sigma}^S_{\phi\phi} = f_S(\xi) + \frac{g_S(\xi)}{2r^3} - K_S\alpha \tag{D.6}$$

Where the functions $f_{M,S}$ and $g_{M,S}$ are unknown functions of ξ, which we shall solve for by applying the proper continuity relations of the total elastic fields. We note however that because the external stress is zero, the function f_M must be uniformly zero.

2. Stress increments From the previous expression, we deduce the displacement and stress increments as the solid/liquid front progresses by an amount $\mathrm{d}\xi$

- In M, $r > R$:

$$\frac{\partial \tilde{u}^M}{\partial \xi}(r,\xi) = \frac{1}{4G_M r^2} \frac{\partial g_M}{\partial \xi} \tag{D.7}$$

$$\frac{\partial \tilde{\sigma}^M_{rr}}{\partial \xi}(r,\xi) = -\frac{1}{r^3} \frac{\partial g_M}{\partial \xi} \tag{D.8}$$

- In S, $r \in [\xi, R]$

$$\frac{\partial \tilde{u}^S}{\partial \xi}(r,\xi) = \frac{r}{3K_S}\frac{\partial f_S}{\partial \xi} + \frac{1}{4G_S r^2}\frac{\partial g_S}{\partial \xi} \tag{D.9}$$

$$\frac{\partial \tilde{\sigma}^S_{rr}}{\partial \xi}(r,\xi) = \frac{\partial f_S}{\partial \xi} - \frac{1}{r^3}\frac{\partial g_S}{\partial \xi} \tag{D.10}$$

Similar relations can be written for hoop stresses as well.

4. Expression of the total stress and displacement due to stress history The stress in the solid shell builds up as the the solidification front advances. Following King & Fletcher King and Fletcher [1973], we write the total stress at a given point as the superposition of the incremental stresses generated by the advancement of the solidification front:

$$\sigma^S_{rr}(r,\xi) = -P(r) + \int_r^\xi \frac{\partial \tilde{\sigma}^S_{rr}}{\partial \xi} \mathrm{d}\xi' \tag{D.11}$$

Where ξ is the position of the solidification front, and $r \in [\xi, R]$ the point in solid S that we consider. $P(r)$ is the pressure that was in the liquid core when the solid/liquid interface was at the position r. Similar relations may be written for the hoop stresses and displacement.

5. Continuity relations We need to solve for the three unknown functions $f_S(\xi)$ and $g_{I,M}(\xi)$. In order to do so, we apply the continuity relations of radial stress and displacement at both M/S and Solid S/Liquid S.

- At the M/S interface, $r = R$:

$$\sigma^S_{rr}(r = R) = \sigma^M_{rr}(r = R) \tag{D.12}$$

$$u^S(r = R) = u^M(r = R) \tag{D.13}$$

- At the Solid S/Liquid S, $r = \xi$:

$$\sigma_{rr}^{S}(r = \xi) = -P(\xi) \tag{D.14}$$

Differentiating the previous equations with respect to ξ at fixed r, we and plugging in the forms of total stress and displacement expressed in equations D.11 and **??**, we get the following relations on the stress increments:

- At the M/S interface, $r = R$:

$$-\frac{1}{R^3}\frac{\partial g_M}{\partial \xi} = \frac{\partial f_S}{\partial \xi} - \frac{1}{R^3}\frac{\partial g_S}{\partial \xi} \tag{D.15}$$

$$-\frac{1}{4G_M R^2}\frac{\partial g_M}{\partial \xi} = \frac{R}{3K_I}\frac{\partial f_S}{\partial \xi} + \frac{1}{4G_I R^2}\frac{\partial g_S}{\partial \xi} \tag{D.16}$$

- At the Solid S/Liquid S, $r = \xi$:

$$\frac{\partial f_S}{\partial \xi} - \frac{1}{\xi^3}\frac{\partial g_S}{\partial \xi} = -\frac{\partial P}{\partial \xi} \tag{D.17}$$

So far we have 3 equations and 4 unknown functions of ξ (f_S, g_S, g_M and P). We need an additional equation governing the pressure rise in the core upon advancing of the solidification front.

As in King and Fletcher [1973], we consider that the advancement of the solid/liquid interface by an amount $\mathrm{d}\xi$ is a combination of the solidification of a thin shell of thickness $\delta\zeta$, and a solid displacement δu due to the pressure in the liquid core.

$$\mathrm{d}\xi = \delta\zeta + \delta u \tag{D.18}$$

We can compute the associated volume change of the liquid core, by noting that some liquid S has been used up during the solidification of the thin shell of thickness $\delta\zeta$. Again, taking $\alpha = 1 - V_{\mathrm{liq}}/V_{\mathrm{sol}}$ to be the volume mismatch between liqid and solid S, we get that the corresponding liquid volume necessary to form a solid shell of thickess $\delta\zeta$ is simply $\delta V_{\mathrm{used}} = 4\pi\xi^2(1-\alpha)\delta\zeta$. We thus get the total volume change

of the core to be:

$$\begin{aligned} \delta V_{\text{core}} &= \delta V_{\text{front}} - \delta V_{\text{used}} \\ &= 4\pi\xi^2(\alpha\delta\zeta + \delta u) \end{aligned} \tag{D.19}$$

We thus get the pressure increase in the core through the relation:

$$\delta P = -\frac{\delta V}{V} K_L \tag{D.20}$$

Where K_L is the bulk modulus or compressibility of liquid S. One gets the following differential equation on P:

$$\frac{\mathrm{d}P}{\mathrm{d}\xi} = -\frac{3K_L}{\xi}\left[\alpha + (1-\alpha)\frac{\mathrm{d}u^S}{\mathrm{d}\xi}\bigg|_{r=\xi}\right] \tag{D.21}$$

Summing up Eq. D.15, D.16 and D.21 yield the following system, with unknowns $\partial f_S/\partial\xi$, $\partial g_S/\partial\xi$ and $\partial g_M/\partial\xi$:

$$\frac{\partial f_S}{\partial\xi} - \frac{1}{R^3}\frac{\partial g_S}{\partial\xi} = -\frac{1}{R^3}\frac{\partial g_M}{\partial\xi} \tag{D.22}$$

$$\frac{R}{3K_I}\frac{\partial f_S}{\partial\xi} + \frac{1}{4G_I R^2}\frac{\partial g_S}{\partial\xi} = -\frac{1}{4G_M R^2}\frac{\partial g_M}{\partial\xi} \tag{D.23}$$

$$\left[1 - \frac{K_L}{K_S}(1-\alpha)\right]\frac{\partial f_S}{\partial\xi} + \frac{1}{\xi^3}\left[1 + \frac{3K_L}{4G_S}(1-\alpha)\right]\frac{\partial g_S}{\partial\xi} = \frac{3K_L}{\xi}\alpha \tag{D.24}$$

Solving this linear system yields:

$$\frac{\partial g_S}{\partial\xi} = \frac{3K_L\alpha}{\xi}\left[\frac{AB}{R^3} + \frac{C}{\xi^3}\right]^{-1} \tag{D.25}$$

$$\frac{\partial f_S}{\partial\xi} = \frac{A}{R^3}\frac{3K_L\alpha}{\xi}\left[\frac{AB}{R^3} + \frac{C}{\xi^3}\right]^{-1} \tag{D.26}$$

$$\frac{\partial g_M}{\partial\xi} = (1-A)\frac{3K_L\alpha}{\xi}\left[\frac{AB}{R^3} + \frac{C}{\xi^3}\right]^{-1} \tag{D.27}$$

where we have defined the following constants:

$$A = \frac{1 - \frac{G_M}{G_S}}{1 + \frac{4G_M}{3K_I}} \tag{D.28}$$

$$B = 1 - \frac{K_L}{K_S}(1 - \alpha) \tag{D.29}$$

$$C = \frac{3K_L}{4G_S}(1 - \alpha) - 1 \tag{D.30}$$

6. Having determined the functions $\partial f_S/\partial\xi$, $\partial g_S/\partial\xi$ and $\partial g_M/\partial\xi$, we can go back to Eq. D.17 and compute the pressure in the liquid core for a given position of solidification front ξ:

$$\begin{aligned} P(\xi) &= -\int_R^\xi \left(\frac{\partial f_S}{\partial\xi} - \frac{1}{\xi^3}\frac{\partial g_S}{\partial\xi}\right) \mathrm{d}\xi' \\ &= \frac{K_L\alpha}{BC}\left[3B\ln\left(\frac{\xi}{R}\right) + (B+C)\ln\left(\frac{R^3(C+AB)}{R^3C + \xi^3 AB}\right)\right] \end{aligned} \tag{D.31}$$

And subsequently we get the radial stress and hoop stresses in the solid shell S as a function of position of solidification front through the equations:

$$\sigma_{rr}^S(r,\xi) = -P(r) + \int_R^\xi \left(\frac{\partial f_S}{\partial\xi} - \frac{1}{r^3}\frac{\partial g_S}{\partial\xi}\right) \mathrm{d}\xi' \tag{D.32}$$

$$\sigma_{\theta\theta}^S(r,\xi) = -P(r) + \int_R^\xi \left(\frac{\partial f_S}{\partial\xi} + \frac{1}{2r^3}\frac{\partial g_S}{\partial\xi}\right) \mathrm{d}\xi' \tag{D.33}$$

Because we are interested in the stresses in the fully solidified sphere, we can take the limit where $\xi = 0$ in the previous expressions. We get:

$$\sigma_{rr}^S(r) = \frac{K_L\alpha}{BC}\left[-3B\ln\frac{r}{R} - (B+C)\ln\frac{R^3(AB+C)}{ABr^3+CR^3} - C\left(1 - \frac{R^3}{Ar^3}\right)\ln\left(1 + \frac{AB}{C}r^3\right)\right] \tag{D.34}$$

$$\sigma_{\theta\theta}^S(r) = \frac{K_L\alpha}{BC}\left[-3B\ln\frac{r}{R} - (B+C)\ln\frac{R^3(AB+C)}{ABr^3+CR^3} - B\left(1 - \frac{R^3}{2Ar^3}\right)\ln\left(1 + \frac{AB}{C}r^3\right)\right] \tag{D.35}$$

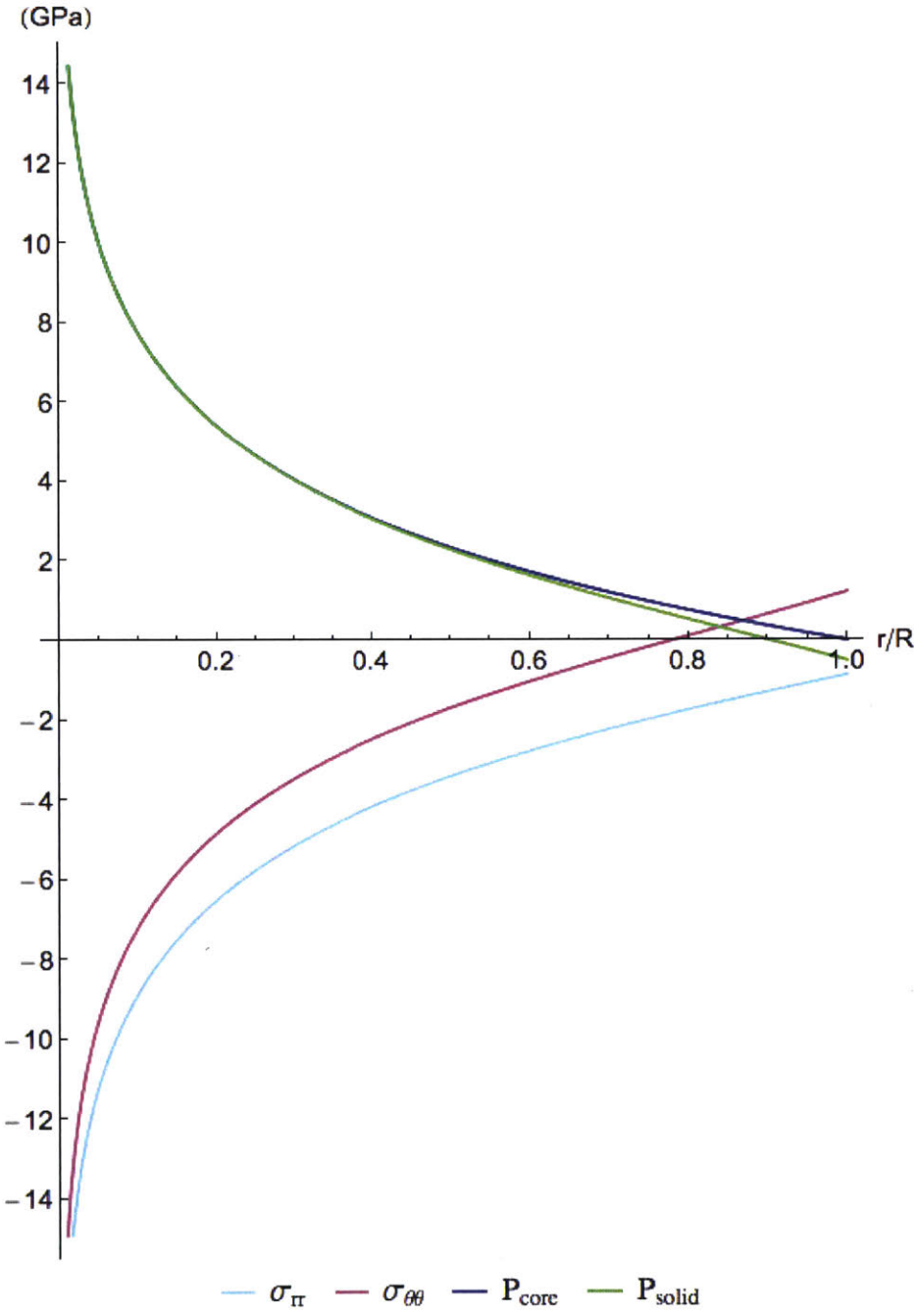

Figure D-2: Computed stresses and pressure in the progressively solidifies sphere.

Appendix E

Ideas that have failed (and possible reasons why)

This appendix is a list - certainly non-exhaustive - of ideas I tried and which have failed, with possible reasons why.

1. Around introducing porosity in thermally-drawn fibers

- **Direct preform-to-fiber drawing of porous PVdF polymer**

  Description of idea Incorporating a porous PVdF layer in a polycarbonate preform (either commercial film or lab-made), and drawing into a fiber.

  What failed Loss of porosity of the porous layer observed under SEM.

  Possible reasons why Densification of structure caused by low-viscosity state of PVdF during draw, causing rapid coarsening of porous structure. Elongational flow during fiber drawing may also accelerate pore collapse.

- **Draw powder and pellets in preform to generate porosity**

  Description of idea Build a polycarbonate preform with a large channel, filled prior to draw with pure PVdF powder or pellets. Concept was to rely on draw

conditions (high temperature and stress) to partially sinter the granular PVdF region while still leaving pores between individual particles.

What failed Powder or pellet region never flowed, consequently fiber would rapidly fracture.

Possible reasons why The high melting point of PVdF coupled with the low thermal-conductivity region defined by the powder/pellet region (highly insulative compared to dense material) probably resulted in PVdF not melting.

2. Around drawing a functional lithium-ion fiber battery

- **Using COC and LDPE as battery electrode binder**

Description of idea Using various methods I prepared composite battery electrodes with different compositions using COC and LDPE as a binder material. For COC I used slurry casting with different solvents (toluene, cyclohexane). For LDPE I used slurry casting with different solvents (mineral oil, toluene), as well as powder ball-milling and pressing, particle sprinking on CPE film and pressing, and extrusion. Idea was to replace the PVdF, because of the high risk of electrode dissolution during the drawing process for a PVdF-based electrode in contact with solvent.

What failed Film preparation was successful with both materials over a range of active material/carbon black compositions. However electochemical performances of coin-cells were in general poor (typically rapid capacity fade), and there was not composition overlap between electrochemically "functional" electrodes and drawable electrodes.

Possible reasons why Poor electrochenical performances were attributed to a variety of reasons. First overall particle loading was in general lower than for PVdF

electrodes; too high particle loading resulted in films with no mechanical integrity - this may be a consequence of molecule weight differences or intrinsic affinity differences between binder material and particles. Second, structure of electrode was in general dense compared to PVdF slurry-cast electrodes (especially when prepared with pressing or extrusion) - this resulted in low-accessiblity of active material particle by lithium ions. Third, wetting of electrolyte solution was lower on both LDPE and COC which may have resulted in poorer electrochemical performances. In any event, electrodes displaying lithium ion intercalation/deintercalation in coin-cell had extremely high particle loading thus prohibiting their draw.

- **Plasticizing PVdF-based electrode during draw**

  Description of idea Preparing a PVdF electrode with high particle loading from traditional slurry casting method (typically not drawable on its own), and relying on solvent plasticization/dissolution of the electrode during the draw to decrease viscosity and permit electrode drawability.

  What failed Idea worked for low particle loading, but failed at higher particle loading required for electrochemical functionality.

  Possible reasons why High particle loading may cause electrode to behave as nearly physically "cross-linked" by particles - therefore not flowing even in presence of solvent/

3. Around preventing delamination in scaffold fibers

- **Using geometry to prevent delamination**

  Description of idea Using geometrical features (*e.g.* dovetails, T-slots) to mechanically prevent delamination between two non-adhering parts in a fiber - like in woodworking.

  What failed Delamination occured anyway.

Possible reasons why Intrinsic flexibility of polymeric materials likely caused slipping and delamination to occur even with dovetails or T-slots.

- **Synthesizing diblock copolymers as interfacial compatibilizer**

Description of idea Instead of surface grafting, directly synthesize a diblock copolymer of LDPE and PCL to promote adhesion between two materials.

What failed Adhesion improvement was small at the preform level, and completely absent at fiber level: fibers consistently delaminated.

Possible reasons why Method of synthesis did not enable high molecular weight of both LDPE region and PCL region. For diffusive adhesion, molecular weight is key to adhesion. Therefore adhesion improvement was likely low because of this; in addition the solvent during the draw likely dissolved away the interface completely, again owing to the low molecular weight of the diblock chains at the interface.

5. Around general fabrication

- **Consolidating preform by solvent-bonding**

Description of idea Instead of thermally consolidating preforms using a hot-press or oven, I tried using solvent-bonding. For example I would apply a thin layer of solvent on a preform part using a brush, clamp the parts, and dry under vacuum for several days.

What failed At the preform drawing step, solvent-bonded region would form bubbles.

Possible reasons why Solvent trapped at the interface not completely removed during drying, thus causing outgassing and bubbling at high temperatures.

- **Drawing tapped/threaded preforms**

  Description of idea For some designs, fastening of two preform parts is necessary but consolidation may not be possible. I tried fastenin two preform parts by tapping one and threading the other, and screwing both together.

  What failed Region did not flow even at a tempearture where pure material would flow; fiber broke.

  Possible reasons why Stresses originating from the tapping/threading procedure may have caused strain hardening of the materials. In addition, possible air gaps between parts may have increased thermal insulation and eventually caused parts not to flow.

Bibliography

Abouraddy A. F., Shapira O., Bayindir M., Arnold J., Sorin F., Hinczewski D. S., Joannopoulos J. D., and Fink Y. Large-scale optical-field measurements with geometric fibre constructs. *Nature Materials*, 5(7): 532–6, 2006. 19, 24

Abouraddy A. F., Bayindir M., and Benoit G. Towards multimaterial multifunctional fibres that see, hear, sense and communicate. *Nature Materials*, 6(May), 2007. 16

Al-Majed A. A., Neumann C. M., Brushart T. M., and Gordon T. Brief electrical stimulation promotes the speed and accuracy of motor axonal regeneration. *The Journal of Neuroscience*, 20(7): 2602–2608, 2000. 46

Alluin O., Wittmann C., Marqueste T., Chabas J. F., Garcia S., Lavaut M. N., Guinard D., Feron F., and Decherchi P. Functional recovery after peripheral nerve injury and implantation of a collagen guide. *Biomaterials*, 30(3): 363–373, 2009. 46

Armand M. and Tarascon J.-M. Building better batteries. *Nature*, 451(7179): 652–657, 2008. 73

Arslantunali D., Dursun T., Yucel D., Hasirci N., and Hasirci V. Peripheral nerve conduits: Technology update. *Medical Devices: Evidence and Research*, 7: 405–424, 2014. 48

Aubert J. H. Structural coarsening of demixed polymer solutions. *Macromolecules*, 23(5): 1446–1452, 1990. 32

Autumn K., Sitti M., Liang Y. A., Peattie A. M., Hansen W. R., Sponberg S., Kenny T. W., Fearing R., Israelachvili J. N., and Full R. J. Evidence for van der Waals adhesion in gecko setae. *Proceedings of the National Academy of Sciences of the United States of America*, 99(19): 12252–12256, 2002. 54

Ballato J., Hawkins T., Foy P., Stolen R., Kokuoz B., Ellison M., McMillen C., Reppert J., Rao A. M., Daw M., Sharma S. R., Shori R., Stafsudd O., Rice R. R., and Powers D. R. Silicon optical fiber. *Optics Express*, 16(23): 18675–18683, 2008. 19, 101

Ballato J., Hawkins T., Foy P., Yazgan-Kokuoz B., Stolen R., McMillen C., Hon N. K., Jalali B., and Rice R. Glass-clad single-crystal germanium optical fiber. *Optics Express*, 17(10): 8029–8035, 2009. 101

Ballato J. and Dragic P. Glass: The Carrier of Light - A Brief History of Optical Fiber. *International Journal of Applied Glass Science*, 10: 1–10, 2016. 16

Balluffi R. W., Allen S. M., and Carter W. C. *Kinetics of Materials.* John Wiley & Sons, Inc., Hoboken, 2005. 32, 104, 108, 109, 127

Bard A. J. and Faulkner L. R. *Electrochemical Methods: Fundamentals and Applications.* Wiley, 2000. 89

Bayindir M., Sorin F., Abouraddy A. F., Viens J., Hart S. D., Joannopoulos J. D., and Fink Y. Metal-insulator-semiconductor optoelectronic fibres. *Nature*, 431: 826–829, 2004. 19, 24

Boyd J. G. and Gordon T. Neurotrophic factors and their receptors in axonal regeneration and functional recovery after peripheral nerve injury. *Molecular Neurobiology*, 27(3): 277–324, 2003. 46

Canales A., Jia X., Froriep U. P., Koppes R. A., Tringides C. M., Selvidge J., Lu C., Hou C., Wei L., Fink Y., and Anikeeva P. Multifunctional fibers for simultaneous optical , electrical and chemical interrogation of neural circuits in vivo. *Nature Biotechnology*, 33(3), 2015. 24

Cha B. J. and Yang J. M. Preparation of poly(vinylidene fluoride) hollow fiber membranes for microfiltration using modified TIPS process. *Journal of Membrane Science*, 291(1-2): 191–198, 2007. 23

Chocat N., Lestoquoy G., Wang Z., Rodgers D. M., Joannopoulos J. D., and Fink Y. Piezoelectric fibers for conformal acoustics. *Advanced Materials*, 24(39): 5327–5332, 2012. 19, 24, 84

Choi M.-C., Kim Y., and Ha C.-S. Polymers for flexible displays: From material selection to device applications. *Progress in Polymer Science*, 33(6): 581–630, 2008. 73

Cristobal A., Vega A. M., and López A. L. *Next generation of photovoltaics: new concepts*, volume 165. Springer, 2012. 99

Cross R. A., Tyson W. H., and Cleveland D. S. Asymmetric hollow fiber membranes for dialysis. *Transactions of the American Society of Artificial Internal Organs*, 17: 279–286, 1971. 23

Cui Z., Hassankiadeh N. T., Lee S. Y., Lee J. M., Woo K. T., Sanguineti A., Arcella V., Lee Y. M., and Drioli E. Poly(vinylidene fluoride) membrane preparation with an environmental diluent via thermally induced phase separation. *Journal of Membrane Science*, 444: 223–236, 2013. 118

da Silva L. F. M., Oschner A., and Adams R. D., editors. *Handbook of adhesion technology*, volume 2. Springer, 2011. 54, 55, 58

Dadaci M., Karagulle N., Sonmez E., Dadaci Z., Isci E. T., Ince B., Vargel I., Piskin E., and Erk A. Y. Evaluation of the effectiveness of biodegradable electrospun caprolactone and poly(Lactic acid-ϵ-caprolactone) nerve conduits for peripheral nerve regenerations in a rat sciatic nerve defect model. *Turkish Journal of Medical Sciences*, 46(2): 539–548, 2016. 47

Daniel C. and Besenhard J. O. *Handbook of Battery Materials.* Wiley, 2 edition, 2011. 75, 77, 79, 80, 81, 83

Egusa S., Wang Z., Chocat N., Ruff Z. M., Stolyarov A. M., Shemuly D., Sorin F., Rakich P. T., Joannopoulos J. D., and Fink Y. Multimaterial piezoelectric fibres. *Nature Materials*, 9(8): 643–648, 2010. 19, 24, 84

Einhardt J. Ü. R., Raith M. M., Raase P., and Reinhard J. *Guide to thin section microscopy.* Second edition, 2012. 112

Evans G. R. D., Brandt K., Widmer M. S., Lu L., Meszlenyi R. K., Gupta P. K., Mikos A. G., Hodges J., Williams J., Gürlek A., Nabawi A., Lohman R., and Patrick C. W. In vivo evaluation of poly(L-lactic acid) porous conduits for peripheral nerve regeneration. *Biomaterials*, 20(12): 1109–1115, 1999. 47

Fan Z., Razavi H., Do J., Moriwaki A., Ergen O., Chueh Y.-L., Leu P. W., Ho J. C., Takahashi T., Reichertz L. A., Neale S., Yu K., Wu M., Ager J. W., and Javey A. Three-dimensional nanopillar-array photovoltaics on low-cost and flexible substrates. *Nature Materials*, 8(8): 648–653, 2009. 73

Fergus J. W. Ceramic and polymeric solid electrolytes for lithium-ion batteries. *Journal of Power Sources*, 195(15): 4554–4569, 2010. 81

Gámez E., Goto Y., Nagata K., Iwaki T., Sasaki T., and Matsuda T. Photofabricated gelatin-based nerve conduits: Nerve tissue regeneration potentials. *Cell Transplantation*, 13(5): 549–564, 2004. 46

Gao W., Emaminejad S., Nyein H. Y. Y., Challa S., Chen K., Peck A., Fahad H. M., Ota H., Shiraki H., Kiriya D., Lien D.-H., Brooks G. A., Davis R. W., and Javey A. Fully integrated wearable sensor arrays for multiplexed in situ perspiration analysis. *Nature*, 529(7587): 509–514, 2016. 73

Gokmen M. T. and Du Prez F. E. Porous polymer particles - A comprehensive guide to synthesis, characterization, functionalization and applications. *Progress in Polymer Science*, 37(3): 365–405, 2012. 40

Green M. A. and Keevers M. J. Optical properties of intrinsic silicon at 300 K. *Progress in Photovoltaics: Research and Applications*, 3(3): 189–192, 1995. 114

Gumennik A., Stolyarov A. M., Schell B. R., Hou C., Lestoquoy G., Sorin F., McDaniel W., Rose A., Joannopoulos J. D., and Fink Y. All-in-fiber chemical sensing. *Advanced Materials*, 24(45): 6005–6009, 2012. 24, 120, 121

Gumennik A., Wei L., Lestoquoy G., Stolyarov A. M., Jia X., Rekemeyer P. H., Smith M. J., Liang X., Grena B. J.-B., Johnson S. G., Gradečak S., Abouraddy A. F., Joannopoulos J. D., and Fink Y. Silicon-in-silica spheres via axial thermal gradient in-fibre capillary instabilities. *Nat Commun*, 4, 2013. 19, 39, 99, 101, 116

Gustafsson G., Cao Y., Treacy G., Klavetter F., Colaneri N., and Heeger A. Flexible light-emitting diodes made from soluble conducting polymers. *Nature*, 357: 477–479, 1992. 73

Hart S. D., Maskaly G. R., Temelkuran B., Prideaux P. H., Joannopoulos J. D., and Fink Y. External reflection from omnidirectional dielectric mirror fibers. *Science*, 296(5567): 510–3, 2002. 19, 24

Hart S. D. *Multilayer composite photonic bandgap fibers.* PhD thesis, Massachusetts Institute of Technology, 2004. 21

Healy N., Mailis S., Bulgakova N. M., Sazio P. J. A., Day T. D., Sparks J. R., Cheng H. Y., Badding J. V., and Peacock A. C. Extreme electronic bandgap modification in laser-crystallized silicon optical fibres. *Nat Materials*, 13(12): 1122–1127, 2014. 116

Hecht J. *City of Light: The Story of Fiber Optics.* Sloan Technology Series. Oxford University Press, 2004. 16

Hoffman-Kim D., Mitchel J. A., and Bellamkonda R. V. Topography, cell response, and nerve regeneration. *Annual Review of Biomedical Engineering*, 12: 203–231, 2010. 46

Hosseini S. S., Peng N., and Chung T. S. Gas separation membranes developed through integration of polymer blending and dual-layer hollow fiber spinning process for hydrogen and natural gas enrichments. *Journal of Membrane Science*, 349 (1-2): 156–166, 2010. 23, 30

Hou C., Jia X., Wei L., Tan S.-C., Zhao X., Joannopoulos J. D., and Fink Y. Crystalline silicon core fibres from aluminium core preforms. *Nature Communications*, 6: 6248, 2015. 21, 22

Hu J. Z. and Spain I. L. Phases of silicon at high pressure. *Solid State Communications*, 51(5): 263–266, 1984. 114

Hu L., Wu H., La Mantia F., Yang Y., and Cui Y. Thin, flexible secondary Li-ion paper batteries. *ACS Nano*, 4(10): 5843–5848, 2010. 73

Hudson T. W., Evans G. R., and Schmidt C. E. Engineering strategies for peripheral nerve repair. *Orthopedic Clinics of North America*, 31(3): 485–498, 2000. 46, 47, 49

Hughes C. S., Postovit L. M., and Lajoie G. A. Matrigel: a complex protein mixture required for optimal growth of cell culture. *Proteomics*, 10(9): 1886–1890, 2010. 68

Israelachvili J. N. *Intermolecular and Surface Forces*. Academic Press, San Diego, third edit edition, 2011. 53, 54

Johnson B. N., Lancaster K. Z., Zhen G., Gupta M. K., Kong Y. L., Engel E. A., Krick K. D., Ju A., Meng F., Enquist L. W., Jia X., and Mcalpine M. C. 3D Printed Anatomical Nerve Regeneration Pathways. *Advanced Functional Materials*, 25: 6205–6217, 2015. 48

Julien C., Mauger A., Vijh A., and Zaghib K. *Lithium Batteries: Science and Technology*. Springer, 2015. 80

Kandel E. and Schwartz J. *Principles of Neural Science*. Principles of Neural Science. McGraw-Hill Education, fifth edit edition, 2013. 43, 44, 66

Kapantaidakis G. and Koops G. High flux polyethersulfone-polyimide blend hollow fiber membranes for gas separation. *Journal of Membrane Science*, 204(1-2): 153–171, 2002. 23

Karkhanechi H., Rajabzadeh S., Di Nicolò E., Usuda H., Shaikh A. R., and Matsuyama H. Preparation and characterization of ECTFE hollow fiber membranes via thermally induced phase separation (TIPS). *Polymer*, 97: 515–524, 2016. 23

Kaufman J. J., Tao G., Shabahang S., Banaei E.-H., Deng D. S., Liang X., Johnson S. G., Fink Y., and Abouraddy A. F. Structured spheres generated by an in-fibre fluid instability. *Nature*, 487(7408): 463–7, 2012. 21, 39, 99, 100, 102, 116

Kaufman J. J., Ottman R., Tao G., Shabahang S., Banaei E.-H., Liang X., Johnson S. G., Fink Y., Chakrabarti R., and Abouraddy A. F. In-fiber production of polymeric particles for biosensing and encapsulation. *Proceedings of the National Academy of Sciences*, 110(39): 15549–54, 2013. 39

Kehoe S., Zhang X. F., and Boyd D. FDA approved guidance conduits and wraps for peripheral nerve injury: A review of materials and efficacy. *Injury*, 43(5): 553–572, 2012. 45

Kim J. J., Hwang J. R., Kim U. Y., and Kim S. S. Operation parameters of melt spinning of polypropylene hollow fiber membranes. *Journal of Membrane Science*, 108(1-2): 25–36, 1995. 23

Kim Y., Haftel V. K., Kumar S., and Bellamkonda R. V. The role of aligned polymer fiber-based constructs in the bridging of long peripheral nerve gaps. *Biomaterials*, 29(21): 3117–3127, 2008. 46

King W. D. and Fletcher N. H. Pressures and stresses in freezing water drops. *Journal of Physics D: Applied Physics*, 6: 2157–2173, 1973. 136, 138, 139

Koppes R. A., Park S., Hood T., Jia X., Abdolrahim Poorheravi N., Achyuta A. H., Fink Y., and Anikeeva P. Thermally drawn fibers as nerve guidance scaffolds. *Biomaterials*, 81: 27–35, 2016. 49, 50, 66, 70

Kurc B. and Jakóbczyk P. Polymer electrolyte and liquid electrolyte based on sulfolane in full cell $LiFePO_4/Li_4Ti_5O_{12}$. *Electrochimica Acta*, 205: 248–255, 2016. 89

Kvavadze E., Bar-Yosef O., Belfer-Cohen A., Boaretto E., Jakeli N., Matskevich Z., and Meshveliani T. 30,000-Year-Old Wild Flax Fibers. *Science*, 325(5946): 1359–1359, 2009. 15

Labet M. and Thielemans W. Synthesis of polycaprolactone: a review. *Chemical Society Reviews*, 38(12): 3484, 2009. 56

Lee J.-H., Jang J.-T., Choi J.-S., Moon S. H., Noh S.-H., Kim J.-G. J.-W. J.-G. J.-W., Kim J.-G. J.-W. J.-G. J.-W., Kim I.-S., Park K. I., and Cheon J. Exchange-coupled magnetic nanoparticles for efficient heat induction. *Nature nanotechnology*, 6(7): 418–422, 2011. 99

Lee J. Y., Bashur C. A., Goldstein A. S., and Schmidt C. E. Polypyrrole-coated electrospun PLGA nanofibers for neural tissue applications. *Biomaterials*, 30(26): 4325–4335, 2009. 47

Lee S. K. and Wolfe S. W. Peripheral nerve injury and repair. *Journal of the American Academy of Orthopaedic Surgeons*, 8(4): 243–252, 2000. 44

Lestoquoy G., Chocat N., Wang Z., Joannopoulos J. D., and Fink Y. Fabrication and characterization of thermally drawn fiber capacitors. *Applied Physics Letters*, 102 (15): 152908, 2013. 19

Li D., Chung T. S., and Wang R. Morphological aspects and structure control of dual-layer asymmetric hollow fiber membranes formed by a simultaneous co-extrusion approach. *Journal of Membrane Science*, 243(1-2): 155–175, 2004. 23, 30

Liu W., Song M.-S., Kong B., and Cui Y. Flexible and Stretchable Energy Storage: Recent Advances and Future Perspectives. *Advanced Materials*, 2016. 74

Lloyd D. R., Kinzer K. E., and Tseng H. S. Microporous membrane formation via thermally-induced phase separation. I. Solid-liquid phase separation. *Journal of Membrane Science*, 52(3): 239–261, 1990. 23, 25, 27

Lloyd D. R., Kim S. S., and Kinzer K. E. Microporous membrane formation via thermally induced phase separation. II. Liquid-liquid phase separation. *Journal of Membrane Science*, 64(1-2): 1–11, 1991. 23, 25, 26, 28

Lu C., Froriep U. P., Koppes R. A., Canales A., Caggiano V., Selvidge J., Bizzi E., and Anikeeva P. Polymer Fiber Probes Enable Optical Control of Spinal Cord and Muscle Function In Vivo. *Advanced Functional Materials*, 24: 6594–6600, 2014. 24

Lundborg G. A 25-year perspective of peripheral nerve surgery: Evolving neuroscientific concepts and clinical significance. *Journal of Hand Surgery*, 25(3): 391–414, 2000. 45

MacCallum J. R. and Vincent C. A. *Polymer Electrolyte Reviews*. Number v. 1 in Developments in polymer electrolyte reviews. Springer Netherlands, 1987. 36

Madduri S., Papaloïzos M., and Gander B. Trophically and topographically functionalized silk fibroin nerve conduits for guided peripheral nerve regeneration. *Biomaterials*, 31(8): 2323–2334, 2010. 46

Manuel Stephan A. Review on gel polymer electrolytes for lithium batteries. *European Polymer Journal*, 42(1): 21–42, 2006. 80, 81

Martha S. K., Haik O., Zinigrad E., Exnar I., Drezen T., Miners J. H., and Aurbach D. On the Thermal Stability of Olivine Cathode Materials for Lithium-Ion Batteries. *Journal of The Electrochemical Society*, 158(10): A1115, 2011. 83

Matsuyama H., Okafuji H., Maki T., Teramoto M., and Kubota N. Preparation of polyethylene hollow fiber membrane via thermally induced phase separation. *Journal of Membrane Science*, 223: 119–126, 2003. 23

McConnell M. D., Kraeutler M. J., Yang S., and Composto R. J. Patchy and multiregion Janus particles with tunable optical properties. *Nano Letters*, 10(2): 603–609, 2010. 99

McGuire K. S., Laxminarayan A., and Lloyd D. R. Kinetics of droplet growth in liquid-liquid phase separation of polymer-diluent systems: experimental results. *Polymer*, 36(26): 4951–4960, 1995. 33

Mehringer C., Wagner R., Jakuttis T., Butz B., Spiecker E., and Peukert W. Gas phase synthesis of anisotropic silicon germanium hybrid nanoparticles. *Journal of Aerosol Science*, 67: 119–130, 2014. 99

Meng C., Liu C., Chen L., Hu C., and Fan S. Highly flexible and all-solid-state paperlike polymer supercapacitors. *Nano Letters*, 10(10): 4025–4031, 2010. 73

Mercado-Pagán Á. E., Kang Y., Findlay M. W., and Yang Y. Development and evaluation of elastomeric hollow fiber membranes as small diameter vascular graft substitutes. *Materials Science and Engineering C*, 49: 541–548, 2015. 23

Mizushima K., Jones P. C., Wiseman P. J., and Goodenough J. B. Li_xCoO_2 ($0<x\leq1$): A new cathode material for batteries of high energy density. *Solid State Ionics*, 3-4 (C): 171–174, 1981. 76

Nagashio K., Okamoto H., Kuribayashi K., and Jimbo I. Fragmentation of faceted dendrite in solidification of undercooled B-doped Si melts. *Metallurgical and Materials Transactions A*, 36A(December): 3407–3413, 2005. 108, 109

Nagashio K., Jian Z., and Kuribayashi K. Direct observation of the crystal-growth transition in undercooled silicon. *Metallurgical and Materials Transactions A*, 33 (9): 2947–2953, 2002. 104

Nakayama K., Takakuda K., Koyama Y., Itoh S., Wang W., Mukai T., and Shirahama N. Enhancement of peripheral nerve regeneration using bioabsorbable polymer tubes packed with fibrin gel. *Artificial Organs*, 31(7): 500–508, 2007. 47

Newton C. D. and Nunamaker D. M. *Textbook of Small Animal Orthopaedics*. Lippincott, 1985. 45

Nishide H. and Oyaizu K. Materials science. Toward flexible batteries. *Science*, 319 (5864): 737–738, 2008. 73

Nitta N., Wu F., Lee J. T., and Yushin G. Li-ion battery materials: Present and future. *Materials Today*, 18(5): 252–264, 2015. 76, 77, 78, 79

Noble J., Munro C. A., Prasad V. S. S. V., and Midha R. Analysis of upper and lower extremity peripheral nerve injuries in a population of patients with multiple injuries. *Journal of Trauma-Injury Infection & Critical Care*, 45(1): 116–122, 1998. 44

Ohzuku T., Ueda A., and Yamamoto N. Zero-Strain Insertion Material of Li Li1/3Ti5/3 O-4 for Rechargeable Lithium Cells. *Journal of The Electrochemical Society*, 142(5): 1431–1435, 1995. 77

Oldenburg S., Averitt R., Westcott S., and Halas N. Nanoengineering of optical resonances. *Chemical Physics Letters*, 288(2-4): 243–247, 1998. 99

Olivier C. and Jamur M. C., editors. *Immunocytochemical Methods and Protocols*. Humana Press, 3 edition, 2010. 69

Orf N. D., Shapira O., Sorin F., Danto S., Baldo M. A., Joannopoulos J. D., and Fink Y. Fiber draw synthesis. *Proceedings of the National Academy of Sciences*, 108(12): 4743–4747, 2011. 21, 22

Ow H., Larson D. R., Srivastava M., Baird B. A., Webb W. W., and Wiesner U. Bright and Stable Core âĹŠ Shell Fluorescent Silica Nanoparticles. *Nano Letters*, 5(1): 113–117, 2005. 99

Park S., Koppes R. A., Froriep U. P., Jia X., Achyuta A. K. H., McLaughlin B. L., and Anikeeva P. Optogenetic control of nerve growth. *Scientific Reports*, 5: 9669, 2015. 46

Patra N., Hladik J., Pavlatová M., Militký J., and Martinová L. Investigation of plasma-induced thermal, structural and wettability changes on low density polyethylene powder. *Polymer Degradation and Stability*, 98(8): 1489–1494, 2013. 56

Qiu Y. R., Matsuyama H., Gao G. Y., Ou Y. W., and Miao C. Effects of diluent molecular weight on the performance of hydrophilic poly(vinyl butyral)/Pluronic F127 blend hollow fiber membrane via thermally induced phase separation. *Journal of Membrane Science*, 338(1-2): 128–134, 2009. 23

Rayleigh L. On the instability of cylindrical fluid surfaces. *Philosophical Magazine Series 5*, 34(207): 177–180, 1892. 100

Rein M., Levy E., Gumennik A., Abouraddy A., Joannopolous J., and Fink Y. Self-assembled fibre optoelectronics with discrete translational symmetry. *Nature Communications*, 2016. 116

Robinson L. R. Traumatic injury to peripheral nerves. *Muscle & Nerve*, 23(6): 863–873, 2000. 45

Rutkowski G. E. and Heath C. A. Development of a bioartificial nerve graft. II. Nerve regeneration in vitro. *Biotechnology Progress*, 18(2): 373–379, 2002. 47

Sanchis M. R., Blanes V., Blanes M., Garcia D., and Balart R. Surface modification of low density polyethylene (LDPE) film by low pressure O2 plasma treatment. *European Polymer Journal*, 42(7): 1558–1568, 2006. 56

Schilz J. and Romanenko V. N. Bulk growth of silicon-germanium solid solutions, 1995. 102, 103, 104

Schmidt C. E., Shastri V. R., Vacanti J. P., and Langer R. Stimulation of neurite outgrowth using an electrically conducting polymer. *Proceedings of the National Academy of Sciences of the United States of America*, 94(17): 8948–8953, 1997. 46

Schmidt C. E. and Leach J. B. Neural Tissue Engineering: Strategies for Repair and Regeneration. *Annual Review of Biomedical Engineering*, 5(1): 293–347, 2003. 44, 45

Song S.-w. and Torkelson J. M. Coarsening Effects on Microstructure Formation in Isopycnic Polymer Solutions and Membranes Produced via Thermally Induced Phase Separation. *Macromolecules*, 27: 6389–6397, 1994. 32, 33

Sorin F., Abouraddy A. F., Orf N., Shapira O., Viens J., Arnold J., Joannopoulos J. D., and Fink Y. Multimaterial Photodetecting Fibers: a Geometric and Structural Study. *Advanced Materials*, 19(22): 3872–3877, 2007. 19, 24

Sorin F., Shapira O., Abouraddy A. F., Spencer M., Orf N. D., Joannopoulos J. D., and Fink Y. Exploiting collective effects of multiple optoelectronic devices integrated in a single fiber. *Nano Letters*, 9(7): 2630–2635, 2009. 19

Splitstoser J. C., Dillehay T. D., Wouters J., and Claro A. Early pre-Hispanic use of indigo blue in Peru. *Science Advances*, 2(9): 1–5, 2016. 15

Stolyarov A. M., Wei L., Shapira O., Sorin F., Chua S. L., Joannopoulos J. D., and Fink Y. Microfluidic directional emission control of an azimuthally polarized radial fibre laser. *Nature Photonics*, 6(4): 229–233, 2012. 24

Strathmann H. *Introduction to Membrane Science and Technology.* Wiley, 2011. 23, 119

Su Y., Chen C., Li Y., and Li J. PVDF membrane formation via thermally induced phase separation. *Journal of Macromolecular Science, Part A: Pure and Applied Chemistry*, 44(1): 99–104, 2007. 27

Sui Z., Burke H. H., and Herman I. P. Raman scattering in germanium-silicon alloys under hydrostatic pressure. *Physical Review B*, 48(4): 2162, 1993. 113

Suzuki Y., Tanihara M., Ohnishi K., Suzuki K., Endo K., and Nishimura Y. Cat peripheral nerve regeneration across 50 mm gap repaired with a novel nerve guide composed of freeze-dried alginate gel. *Neuroscience Letters*, 259(2): 75–78, 1999. 46

Tan X., Tan S. P., Teo W. K., and Li K. Polyvinylidene fluoride (PVDF) hollow fibre membranes for ammonia removal from water. *Journal of Membrane Science*, 271 (1-2): 59–68, 2006. 23

Tanaka T., Tsuchiya T., Takahashi H., Taniguchi M., and Lloyd D. R. Microfiltration membrane of polymer blend of poly(l-lactic acid) and poly(ϵ-caprolactone). *Desalination*, 193(1-3): 367–374, 2006. 28

Tao G., Stolyarov A. M., and Abouraddy A. F. Multimaterial fibers. *International Journal of Applied Glass Science*, 3(4): 349–368, 2012. 25

Tiller W., Jackson K., Rutter J., and Chalmers B. The redistribution of solute atoms during the solidification of metals. *Acta Metallurgica*, 1(4): 428–437, 1953. 109

Tomotika S. On the instability of a cylindrical thread of a viscous liquid surrounded by another viscous fluid. *Proceedings of the Royal Society A: Mathematical, Physical and Engineering Sciences*, 150(870): 322–337, 1935. 100

Unger R. E., Huang Q., Peters K., Protzer D., Paul D., and Kirkpatrick C. J. Growth of human cells on polyethersulfone (PES) hollow fiber membranes. *Biomaterials*, 26(14): 1877–1884, 2005. 23

Van de Witte P., Dijkstra P. J., Van den Berg J. W. A., and Feijen J. Phase separation processes in polymer solutions in relation to membrane formation. *Journal of Membrane Science*, 117(1-2): 1–31, 1996. 26, 27, 28, 32, 119

Vleggeert-Lankamp C. L. A. M., de Ruiter G. C. W., Wolfs J. F. C., Pêgo A. P., van den Berg R. J., Feirabend H. K. P., Malessy M. J. A., and Lakke E. A. J. F. Pores in synthetic nerve conduits are beneficial to regeneration. *Journal of Biomedical Materials Research: Part A*, 80A(4): 965–982, 2007. 47

Wang A., Ao Q., Cao W., Yu M., He Q., Kong L., Zhang L., Gong Y., and Zhang X. Porous chitosan tubular scaffolds with knitted outer wall and controllable inner structure for nerve tissue engineering. *Journal of Biomedical Materials Research: Part A*, 79A(1): 36–45, 2006. 46

Wang C., Yin H., Dai S., and Sun S. A general approach to noble metal-metal oxide dumbbell nanoparticles and their catalytic application for CO oxidation. *Chemistry of Materials*, 22(10): 3277–3282, 2010. 23

Wang K. Y., Chung T. S., and Gryta M. Hydrophobic PVDF hollow fiber membranes with narrow pore size distribution and ultra-thin skin for the fresh water production through membrane distillation. *Chemical Engineering Science*, 63(9): 2587–2594, 2008. 23

Wang K. Y., Foo S. W., and Chung T. S. Mixed matrix PVDF hollow fiber membranes with nanoscale pores for desalination through direct contact membrane distillation. *Industrial and Engineering Chemistry Research*, 48(9): 4474–4483, 2009. 24

Wang S. and Cai L. Polymers for fabricating nerve conduits. *International Journal of Polymer Science*, 2010, 2010. 48

Wang W., Choi D., and Yang Z. Li-ion battery with $LiFePO_4$ cathode and $Li_4Ti_5O_{12}$ anode for stationary energy storage. *Metallurgical and Materials Transactions A: Physical Metallurgy and Materials Science*, 44: 21–25, 2013. 89, 91

Wen X. and Tresco P. A. Fabrication and characterization of permeable degradable poly(dl-lactide-co-glycolide) (PLGA) hollow fiber phase inversion membranes for use as nerve tract guidance channels. *Biomaterials*, 27(20): 3800–3809, 2006. 23

Widmer M. S., Gupta P. K., Lu L., Meszlenyi R. K., Evans G. R. D., Brandt K., Savel T., Gurlek A., Patrick C., Mikos A. G., and Charles W. P. J. Manufacture of porous biodegradable polymer conduits by an extrusion process for guided tissue regeneration. *Biomaterials*, 19(21): 1945–1955, 1998. 47

Wu Q., Xu Y., Yao Z., Liu A., and Shi G. Supercapacitors based on flexible graphene/polyaniline nanofiber composite films. *ACS Nano*, 4(4): 1963–1970, 2010. 73

Xiang J., Lu W., Hu Y., Wu Y., Yan H., and Lieber C. M. Ge/Si nanowire heterostructures as high-performance field-effect transistors. *Nature*, 441(7092): 489–493, 2006. 99

Xu K., Zhang S., Poese B. A., and Jow T. R. Lithium bis(oxalato)borate stabilizes graphite anode in propylene carbonate. *Electrochemical and Solid-State Letters*, 5 (11): A259, 2002. 83

Xu K. Nonaqueous liquid electrolytes for lithium-based rechargeable batteries. *Chemical Reviews*, 104(10): 4303–417, 2004. 80

Xu S., Zhang Y., Cho J., Lee J., Huang X., Jia L., Fan J. A., Su Y., Su J., Zhang H., Cheng H., Lu B., Yu C., Chuang C., Kim T., Song T., Shigeta K., Kang S., Dagdeviren C., Petrov I., Braun P. V., Huang Y., Paik U., and Rogers J. A. Stretchable batteries with self-similar serpentine interconnects and integrated wireless recharging systems. *Nature Communications*, 4: 1543–1550, 2013. 73

Yang Q., Chung T. S., and Santoso Y. E. Tailoring pore size and pore size distribution of kidney dialysis hollow fiber membranes via dual-bath coagulation approach. *Journal of Membrane Science*, 290(1-2): 153–163, 2007. 23, 66

Ye S. and Carroll R. L. Design and fabrication of bimetallic colloidal "janus" particles. *ACS Applied Materials and Interfaces*, 2(3): 616–620, 2010. 99

Yoon J., Baca A. J., Park S.-I., Elvikis P., Geddes J. B., Li L., Kim R. H., Xiao J., Wang S., Kim T.-H., Motala M. J., Ahn B. Y., Duoss E. B., Lewis J. A., Nuzzo R. G., Ferreira P. M., Huang Y., Rockett A., and Rogers J. A. Ultrathin silicon solar microcells for semitransparent, mechanically flexible and microconcentrator module designs. *Nature Materials*, 7(11): 907–915, 2008. 73

Yu H., Chen M., Rice P. M., Wang S. X., White R. L., and Sun S. Dumbbell-like Bifunctional Au-Fe_3O_4 Nanoparticles. *Nano Letters*, 5(2): 379–382, 2005. 99

Yu T. T. and Shoichet M. S. Guided cell adhesion and outgrowth in peptide-modified channels for neural tissue engineering. *Biomaterials*, 26(13): 1507–1514, 2005. 66

Zhang Q., Lu X., and Zhao L. Preparation of polyvinylidene fluoride (PVDF) hollow hiber hemodialysis membranes. *Membranes*, 4(1): 81–95, 2014. 23, 47

Zhang S. S., Xu K., Foster D. L., Ervin M. H., and Jow T. R. Microporous gel electrolyte Li-ion battery. *Journal of Power Sources*, 125(1): 114–118, 2004. 80

Zhou J., Li J., Yu W., Li X., and Zhou C. Studies on the melt spinning process of noncircular fiber by numerical and experimental models. *Polymer Engineering & Science*, 50(10): 1935–1944, 2010. 28